

**UNDERSTANDING THE LAST GLACIAL AND DEGLACIAL OCEAN
CIRCULATION USING AN ISOTOPE-ENABLED OCEAN MODEL**

by

Sifan Gu

A dissertation submitted in partial fulfillment of
the requirements for the degree of

Doctor of Philosophy

(Atmospheric and Oceanic Sciences)

at the

UNIVERSITY OF WISCONSIN-MADISON

2018

Date of final oral examination: 04/23/18

The dissertation is approved by the following members of the Final Oral Committee:

Zhengyu Liu, Professor, Atmospheric and Oceanic Sciences

Matthew Hitchman, Professor, Atmospheric and Oceanic Sciences

Ankur Desai, Professor, Atmospheric and Oceanic Sciences

Jack Williams, Professor, Atmospheric and Oceanic Sciences

Stephen Meyers, Associate Professor, Geoscience

Shaun Marcott, Assistant Professor, Geoscience

ACKNOWLEDGMENT

First, I would like to express my sincere gratitude to my advisor Prof. Zhengyu Liu, not only for his guidance, patience, and support throughout my PhD study, but also for bringing me into the fascinating field of paleoclimate study. Numerous discussions with him clear my confusions and shape my way of thinking on scientific questions.

I am also grateful to the members of my committee, Profs. Matt Hitchman, Ankur Desai, Jack Williams, Shaun Marcott and Stephen Meyers for their time, expertise and valuable feedback on the preliminary results.

My gratitude also goes to Keith Lindsay from the National Center for Atmospheric Research (NCAR) and Alexandra Jahn from University of Colorado Boulder for their help on the model development.

I am grateful to the professors and members in the Center for Climate Research and the Department of Atmospheric and Oceanic Sciences. Especially I would like to thank Kevin Braun, Julie Niesen and Dee VanRuyven for the good working environment.

I would like to thank my friends and fellow graduate students Yan Yu, Jiaxu Zhang, Jiang Zhu, Ke Xu, Feiyu Lu, Chengfei He, Lingwei Li for the helpful discussions and all the great times we shared.

Last but not least, I would like to express deepest thanks to my husband, my parents and grandmother for their endless love and support over the years.

Contents

Contents.....	ii
List of Tables.....	iv
List of Figures.....	v
Abstract	1
1 Introduction.....	3
1.1 ϵ_{Nd} as a Water Mass Tracer.....	4
1.2 $^{231}Pa/^{230}Th$ as a Proxy for AMOC Strength.....	6
1.3 Controversial AAIW Northward Penetration in the Atlantic during the Last Deglaciation.....	7
1.4 Can $\delta^{18}O_c$ Gradient be Used to Reconstruct AMOC Strength?.....	9
1.5 Objectives of my PhD Study.....	12
2 Isotope-enabled Ocean Model Development.....	13
2.1 Neodymium Isotope Development.....	13
2.1.1 Physical Ocean Model and the Biogeochemical Component in POP2.....	13
2.1.2 Neodymium implementation	15
2.1.3 Parameter Tuning and Model Validation.....	17
2.1.4 ϵ_{Nd} in Idealized Hosing Experiment.....	23
2.1.5 Conclusion and Discussion.....	29
2.2 ^{231}Pa and ^{230}Th Development.....	30
2.2.1 ^{231}Pa and ^{230}Th Implementation.....	30
2.2.2 Model Validation.....	32
2.2.3 ^{231}Pa and ^{230}Th in Idealized Hosing Experiment.....	39
2.2.4 Conclusion and Discussion.....	47
2.2.3 ^{231}Pa and ^{230}Th in idealized hosing experiment	
2.2.4 Conclusion and Discussion	

3 Deglacial Northward Penetration of AAIW in the Atlantic.....	48
3.1 Transient Deglacial Simulation and Nd Module Setup.....	48
3.2 Coherent AAIW response and AMOC strength.....	50
3.2.1 Reduced AAIW Northward Penetration but Increased Depth and Thickness of AAIW Water Mass during Weaker AMOC.....	50
3.2.2 Mechanism.....	56
3.2.3 AAIW Depth, Pycnocline Depth and Shallow Reverse Cell.....	59
3.3 Reconciling ϵ_{Nd} Reconstructions Controversy with Core Depth.....	66
3.4 Conclusion and Discussion.....	75
4 Using Horizontal $\delta^{18}O_c$ Gradient to Reconstruct Past Overturning Strength.....	77
4.1 Transient Deglacial Simulation Set Up.....	77
4.2 Deglacial Evolution of $\delta^{18}O_c$ Gradient Over Florida Straits and AMOC.....	79
4.3 Glacial and Deglacial Evolution of $\delta^{18}O_c$ Gradient across the Atlantic at 30°S....	85
4.4 How Well in General Can $\delta^{18}O_c$ Gradient Across the Basin and the West Boundary in the Atlantic Represent AMOC Strength?.....	93
4.5 Conclusion.....	95
5 Conclusions and Future Perspectives.....	96
5.1 Conclusions.....	96
5.2 Future Perspectives.....	97
Appendix: Vertical differentiation scheme in calculating the reversible scavenging term.....	100
BIBLIOGRAPHY.....	102

LIST OF TABLES

2.1.1 The linear regression coefficient (rc) between model ϵ_{Nd} and observational ϵ_{Nd} in different ocean basins at different depth range: 0-200m, 200-1000m, 1000-3000m and depth deeper than 3000m. N is the number of points.....	22
2.2.1. Partition coefficients for different particle types for ^{231}Pa and ^{230}Th	32
2.2.2. References for observations of water column ^{231}Pa and ^{230}Th activity (left column) and Holocene core-top $^{231}Pa/^{230}Th$ (right column).....	39
3.2.1 AMOC strength, AAIW depth and Pycnocline depth in CTRL and WD_SO.....	62

LIST OF FIGURES

- 1.1 (a) Location of each ϵ_{Nd} reconstruction site in the tropical Atlantic. KNR166-2-26JPC: (24°19.62'N, 83°15.14'W, 546m), yellow; MD99-2198: (12.09°N, 61.23°W, 1330m), green; KNR197-3-46CDH: (7.836°N, 53.663°W, 947m), blue. (b) Reconstructed ϵ_{Nd} evolutions at each site. HS1 is indicated by grey shading.....9
- 2.1.1 Annual mean particle fields produced by the ecosystem module in the CESM under present day forcing. (a) $CaCO_3$ flux at 105m ($mol\ m^{-2}\ yr^{-1}$). (b) Opal flux at 105m ($mol\ m^{-2}\ yr^{-1}$). (c) POC flux at 105m ($mol\ m^{-2}\ yr^{-1}$). (d) \log_{10} values of annual atmospheric dust deposition ($g\ m^{-2}\ yr^{-1}$).....14
- 2.1.2 Contours of cost function of $[Nd]_d$ ($J_{[Nd]_d}$: solid lines, unit: $pmol\ kg^{-1}$) and ϵ_{Nd} ($J_{\epsilon_{Nd}}$: color, unit: ϵ_{Nd} units) and total Nd inventory (dashed lines, unit: $10^{12}g$) for different combinations of $f_{boundary}$ and $\frac{[Nd]_p}{[Nd]_d}$ at the end of each experiment. $J_{[Nd]_d}$ reaches minimum at the pink square; $J_{\epsilon_{Nd}}$ reaches minimum at the red triangle; CTRL is indicated by the yellow star.....18
- 2.1.3 Nd concentration (a and b) and ϵ_{Nd} (c and d) in the vertical section in the Atlantic (20°W-30°W) and the Pacific (150°W-160°W) in CTRL. Observations are superimposed as filled circles using the same color scale.....19
- 2.1.4 Seafloor Nd concentration in CTRL. Observations are superimposed as filled circles using the same color scale. Selected Nd concentration profiles are also shown: black line for CTRL and red dot for observation.....20
- 2.1.5 Seafloor ϵ_{Nd} in CTRL. Observations are superimposed as filled circles using the same color scale. Selected ϵ_{Nd} profiles are also shown: black line for CTRL and red dot for observation.....21
- 2.1.6 Scatter plot of Nd concentration (a, b and c) and ϵ_{Nd} (d, e and f) between observations and CTRL in different ocean basins. Southern Ocean is included in each Atlantic, Pacific and Indian Ocean section. Observations in different depth ranges are indicated by different colors: 0-200m (red), 200-1000m (yellow), 1000-3000m (green) and depth deeper than 3000m (navy).....21
- 2.1.7 (a) Atlantic zonal mean p-fixed ϵ_{Nd} (color) and salinity (contour). (b) South Atlantic (0°S-30°S) mean p-fixed ϵ_{Nd} vertical profile in different experiments with varying $\frac{[Nd]_p}{[Nd]_d}$ ($f_{boundary} = 4 \times 10^9\ g\ yr^{-1}$).....23
- 2.1.8 Time evolutions (decadal mean) in HOSING. (a) Fresh water forcing (black) and AMOC strength (navy). (b) ϵ_{Nd} value for AABW end-member, which is calculated as the

average of 60°S-70°S below 4000m. (c) ϵ_{Nd} value for NADW end-member, which is calculated as the average of 50°N-60°N between 2500m to 3000m. (d) ϵ_{Nd} value for NADW in the east Atlantic, which is calculated as the average of 50°N-60°N between 2500m to 3000m east of 20°W. (e) ϵ_{Nd} value for NADW in the west Atlantic, which is calculated as the average of 50°N- 60°N between 2500m to 3000m west of 50°W. (f) ϵ_{Nd} value at 2890m at (40°N, 40°W), where productivity experiences great changes in HOSING. In the ϵ_{Nd} time series (b-f), green is p-fixed ϵ_{Nd} and red is p-coupled ϵ_{Nd}25

2.1.9 Atlantic zonal mean p-fixed ϵ_{Nd} (color) and Atlantic meridional overturning streamfunction (contour) in AMOC_on (a) and AMOC_off (b). The difference of Atlantic zonal mean p-fixed ϵ_{Nd} between AMOC_off and AMOC_on (c). (d), (e) and (f) are the same as (a), (b) and (c) for p-coupled ϵ_{Nd} . The difference between p-coupled and p-fixed ϵ_{Nd} during AMOC_off.....26

2.1.10 South Atlantic (a) and North Atlantic (b) mean ϵ_{Nd} profile during AMOC_on (solid line) and AMOC_off (dash line) for p-fixed (green) and p-coupled (red) ϵ_{Nd}27

2.1.11 ϵ_{Nd} (p-fixed) at 2500m in CTRL (a) and the difference between different times in HOSING and CTRL (b-f). Velocity (cm/s) at different times is overlaid in each plot.....28

2.2.1 Dissolved ^{231}Pa , dissolved ^{230}Th and particulate $^{231}Pa/^{230}Th$ in CTRL along GEOTRACES transect GA02S for both p-fixed (top row) and p-coupled (bottom row) ^{231}Pa and ^{230}Th (colored contour). Observations of dissolved ^{231}Pa and ^{230}Th activity are superimposed as colored circles using the same color scale.....33

2.2.2 Dissolved ^{231}Pa , dissolved ^{230}Th and particulate $^{231}Pa/^{230}Th$ in CTRL along GEOTRACES transect GA03 for both p-fixed (top row) and p-coupled (bottom row) ^{231}Pa and ^{230}Th (colored contour). Observations of dissolved ^{231}Pa and ^{230}Th activity are superimposed as colored circles using the same color scale.....34

2.2.3 Sediment $^{231}Pa/^{230}Th$ activity ratio in CTRL for both p-fixed (a) and p-coupled version (b). Observations are attached as filled cycles using the same color map. The $^{231}Pa/^{230}Th$ activity ratio is plotted relative to the production ratio of 0.093 on a \log_{10} scale.....35

2.2.4 Scatter plot of global dissolved and particulate ^{231}Pa and ^{230}Th between observation and CTRL (p-fixed) (unit: dpm/m³). (a) dissolved ^{231}Pa ; (b) particulate ^{231}Pa ; (c) dissolved ^{230}Th ; (d) particulate ^{230}Th . Observations in different depth range are indicated by different colors: green for 0-100m; red for 100m-1,000m; blue for 1,000m-3,000m and yellow for deeper than 3,000m. Purple line is the least squared linear regression line for all depth range, the slope of which is indicated at the top right of each plot. Green line is the least squared linear regression line for depth from 0-100m. Red line is the least squared linear regression line for depth from 100m -1,000m. Blue line is the least squared

linear regression line for depth from 1,000m-3,000m. Yellow line is the least squared linear regression line for depth deeper than 3,000m.....36

2.2.5 Comparison of particle fluxes between AMOC_on and AMOC_off. CaCO₃ flux at 105m (mol m⁻² yr⁻¹) during AMOC_on (a), AMOC_off (b) and difference between AMOC_off and AMOC_on. (b) Opal flux at 105m (mol m⁻² yr⁻¹) during AMOC_on (d), AMOC_off (e) and difference between AMOC_off and AMOC_on (f). POC flux at 105m (mol m⁻² yr⁻¹) during AMOC_on (g), AMOC_off (h) and difference between AMOC_off and AMOC_on (i).....40

2.2.6 Time evolutions in HOSING. (a) Freshwater forcing (black) and AMOC strength (navy), which is defined as the maximum of the overturning streamfunction below 500m in the North Atlantic. (b) North Atlantic average sediment ²³¹Pa/²³⁰Th activity ratio from 20°N to 60°N: p-fixed (green) and p-coupled (red). Production ratio of 0.093 is indicated by a solid black line (similar in c, d, e and f). (c) Sediment ²³¹Pa/²³⁰Th activity ratio at (55°N, 30°W). (d) Sediment ²³¹Pa/²³⁰Th activity ratio at (40°N, 40°W). (e) Sediment ²³¹Pa/²³⁰Th activity ratio at (35°N, 58°W). (f) Sediment ²³¹Pa/²³⁰Th activity ratio at (34°N, 60°W). (e) and (f) are near Bermuda Rise. Locations of each site are shown as dots in Figure 2.2.5b.....42

2.2.7 Sediment ²³¹Pa/²³⁰Th activity ratio during AMOC off state and the difference between AMOC off and CTRL. (a) P-fixed log₁₀[(²³¹Pa/²³⁰Th)/0.093] in AMOC_off. (b) Difference of p-fixed sediment ²³¹Pa/²³⁰Th activity ratio between AMOC_off and AMOC_on. (c) and (d) are similar to (a) and (b) for p-coupled sediment ²³¹Pa/²³⁰Th activity ratio.....43

2.2.8 (a) Correlation of p-fixed and p-coupled evolution of sediment ²³¹Pa/²³⁰Th activity ratio in HOSING. (b) Scatter plot of p-fixed and p-coupled sediment ²³¹Pa/²³⁰Th activity ratio change from AMOC_on to AMOC_off in the Atlantic and the Southern Ocean (70°W-20°E). Purple line is the least squared linear regression line and slope is the linear regression coefficient.....44

2.2.9 Difference of Atlantic zonal mean particulate ²³¹Pa/²³⁰Th between AMOC_off and AMOC_on: (a) p-fixed and (b) p-coupled. (c) North Atlantic (20°N-60°N) average profile during AMOC_on (solid) and AMOC_off (dash) for p-fixed (green) and p-coupled (red) particulate ²³¹Pa/²³⁰Th.....46

3.1.1 Comparison of present day ε_{Nd} fields between model and observation. (A) Global map of ε_{Nd} at the sea floor. Observations are superimposed as filled circles, using the same color scale. Selected vertical profiles, focusing on tropical Atlantic, show observed (red) and simulated (black) ε_{Nd} values.....49

3.2.1 Model Atlantic zonal mean ε_{Nd} (color shading) and salinity (black contour) under present day forcing. The green line is the isopycnal line of σ_{AAIW}.....51

3.2.2 Evolution during the last deglaciation in reconstructions and iPOP2-TRACE. (a) Winter surface density in NADW (black) and AAIW (red) production region. (b) Model maximum AMOC transport (under 500m) in iPOP2-TRACE (black), Sedimentary $^{231}\text{Pa}/^{230}\text{Th}$ record of OCE326-5GGC (dashed green) and AAIW transport which is defined as the meridional transport at equatorial Atlantic of layers between ($\sigma_{\text{AAIW}} - 0.5$) and ($\sigma_{\text{AAIW}} + 0.5$) (red). (c) Estimation of AAIW northward penetration latitude (navy dots). AAIW depth at equatorial Atlantic (red). Black triangle on the right of Y axis indicates the late Holocene AAIW depth. (d) Zonal mean AAIW ϵ_{Nd} value at equatorial Atlantic (solid black), the difference between AAIW ϵ_{Nd} value at equatorial Atlantic and AAIW end-member ϵ_{Nd} value (red) and ϵ_{Nd} value at 1,000 m at western boundary equatorial Atlantic (dashed black). (e) ϵ_{Nd} reconstruction in Demerara Rise (dashed navy) and ϵ_{Nd} evolution at this location in iPOP2-TRACE (solid navy). (f) ϵ_{Nd} records from Tobago Basin (dashed green) and ϵ_{Nd} evolution at this location in iPOP2-TRACE (solid green). HS1 is indicated by grey shading.....	53
3.2.3 Comparison between LGM (20 kyr B.P.) and HS1 (16 kyr B.P.) in iPOP2-TRACE experiment. Atlantic overturning streamfunction (black contour) and Atlantic zonal mean potential density (color shading) during (a) LGM and (b) HS1. Atlantic zonal mean ϵ_{Nd} (color shading), salinity (black contour) and isopycnal line for σ_{AAIW} (green line) at (c) LGM and (d) HS1. Circulation (vectors) and ϵ_{Nd} (color) at σ_{AAIW} surface: (e) LGM and (f) HS1.....	54
3.2.4 Northward transport at equatorial Atlantic of layers between ($\sigma_{\text{AAIW}} - d$) and ($\sigma_{\text{AAIW}} + d$): $d = 0.5$ (red), 0.4 (magenta), 0.3 (purple), 0.2 (navy) and 0.1 (green).....	55
3.2.5 Velocity and meridional transport at annual mean σ_{AAIW} surface during LGM and HS1. (a) Vectors indicate direction and magnitude of (u,v) (cm/s) and color indicate magnitude (cm/s) during LGM. (b) meridional transport (Sv) at different latitudes during LGM, green for western boundary transport, red for interior and black for total transport. Same for (c) and (d) during HS1.....	58
3.2.6 AMOC in CTRL (a) and WD_SO (b). Atlantic zonal mean ϵ_{Nd} (color contour) and salinity (line contour) in CTRL (c) and WD_SO (d). Green line indicates the AAIW depth and the purple line indicates the pycnocline depth.....	62
3.2.7 AMOC in CTRL (a), HOSING_01 (b), HOSING_03 (c), HOSING_05 (d), HOSING_07 (e) and HOSING_10 (f).....	64
3.2.8 AMOC strength, reverse cell strength, reverse cell depth and pycnocline depth in CTRL, HOSING_01, HOSING_03, HOSING_05, HOSING_07 and HOSING_10.....	65
3.2.9 AMOC in WD_0040S (a) and WD_0040S_HOSING (b).....	65

3.2.10 The AAIW ϵ_{Nd} decay and the AMOC strength in the sensitivity experiments. The black dots are experiments with no change of wind stress. The red dots are the experiments with the change of wind stress over $0^{\circ}S$ to $40^{\circ}S$ in the Atlantic.....65

3.3.1 Comparison between model ϵ_{Nd} (solid) with reconstructions (dash). (a) KNR197-3-9GGC in Demerara Rise ($7^{\circ}55.8'N$, $53^{\circ}34.51'W$, 1100m). (b) KNR197-3-25GGC in Demerara Rise ($7^{\circ}42.27'N$, $53^{\circ}47.12'W$, 671m). (d) KNR166-2-26JPC in the Florida Straits ($24^{\circ}19.62'N$, $83^{\circ}15.14'W$, 546m). (d) GeoB2107-3 in southern Brazil margin ($27.2^{\circ}S$, $46.5^{\circ}W$, 1050m).....67

3.3.2: ϵ_{Nd} evolution for the upper 2,000m at four different locations in the tropical North Atlantic sites. (a) Area average from Gulf of Mexico and Caribbean Sea ($15^{\circ}N$ - $30^{\circ}N$, $85^{\circ}W$ - $100^{\circ}W$). Black contours are vertical velocity in 10^{-4} cm/s. (b) ($24.33^{\circ}N$, $83.25^{\circ}W$), which is the horizontal location for site KNR166-2-26JPC in Florida Strait (c) ($7.84^{\circ}N$, $53.66^{\circ}W$), which is the horizontal location for site KNR197-3-46CDH in Demerara Rise and (d) ($12.09^{\circ}N$, $61.23^{\circ}W$), which is the horizontal location for site MD99-2198 in Tobago Basin. The depth of each core is indicated by a thin black dash line with filled symbol: KNR166-2-26JPC(triangle), KNR197-3-46CDH (square) and MD99-2198 (star). The depth of σ_{AAIW} is indicated by thick black lines in C and D: σ_{AAIW} by salinity (solid, defined in text) and σ_{AAIW} by ϵ_{Nd} (dash, defined as average of potential density where ϵ_{Nd} reaches maximum vertically Atlantic average from $40^{\circ}S$ to equator). The maximum ϵ_{Nd} tongue is shifted slightly deeper in the minimum salinity tongue, because of the reversible scavenging by settling particles.....69

3.3.3 ϵ_{Nd} tracer budget analysis for ($12^{\circ}N$, $75^{\circ}W$, 1330m), which is near MD99-2198. (a), time series of ϵ_{Nd} tendency terms: zonal advection (magenta), meridional advection (red), horizontal advection (zonal advection + meridional advection) (yellow), vertical advection (navy) and mixing (green). (b), evolution of velocity: zonal velocity (u) (red), meridional velocity (v) (navy) and vertical velocity multiplied by 10^4 (w) (green). (c), ϵ_{Nd} gradient: zonal gradient (red), meridional gradient (navy) and vertical gradient (green).....70

3.3.4 Ocean current (vector) and ϵ_{Nd} (color) at the depth of KNR197-3-46CDH (947m) (a and c) and MD99-2198 (1330m) (b and d) during LGM and HS1. The location of each site is indicated by a black box.....72

3.3.5 ϵ_{Nd} tracer budget analysis for site KNR197-3-46CDH (a, c and e) and MD99-2198 (c, d and f). (a) and (b), time series of ϵ_{Nd} tendency terms: zonal advection (magenta), meridional advection (red), horizontal advection (zonal advection + meridional advection) (yellow), vertical advection (navy) and mixing (green). (c) and (d), evolution of velocity: zonal velocity (u) (red), meridional velocity (v) (navy) and vertical velocity multiplied by 10^4 (w) (green). (e) and (f), ϵ_{Nd} gradient: zonal gradient (red), meridional gradient (navy) and vertical gradient (green).....73

3.3.6 ϵ_{Nd} tracer budget analysis for (12°N, 75°W, 1330m), which is near MD99-2198. (a), time series of ϵ_{Nd} tendency terms: zonal advection (magenta), meridional advection (red), horizontal advection (zonal advection + meridional advection) (yellow), vertical advection (navy) and mixing (green). (b), evolution of velocity: zonal velocity (u) (red), meridional velocity (v) (navy) and vertical velocity multiplied by 10^4 (w) (green). (c), ϵ_{Nd} gradient: zonal gradient (red), meridional gradient (navy) and vertical gradient (green)..74

3.4.1. Schematic figure of circulation and ϵ_{Nd} during LGM and HS1 at different depth: AAIW core depth (A and B), 947 m (C and D) and 1330 m (E and F). Red filled circle represents upwelling in the Gulf of Mexico and Caribbean Sea, with larger size for stronger upwelling. Curves with arrows represents flow, with thickness for flow magnitude and color from blue to green to yellow to red for the increasing of ϵ_{Nd} . Locations of each observational site are indicated by filled symbols: KNR166-2-26JPC: (24°19.62'N, 83°15.14'W, 546m), triangle; MD99-2198: (12.09°N, 61.23°W, 1330m), star; KNR197-3-46CDH: (7.836°N, 53.663°W, 947m), square.....76

4.1.1 AMOC during LGM (a contour) and HS1(b contour) in CTRACE. Atlantic zonal mean salinity during LGM (a color) and HS1 (b color). Atlantic zonal mean temperature during LGM (c) and HS1 (d).....78

4.2.1 Time evolutions in the Florida Straits in CTRACE. (a) AMOC strength (black) and observational (red dot) and model (red curve) $^{231}\text{Pa}/^{230}\text{Th}$ from site OCE326-GGC5 (33°42'N, 57°35'W, 4.55km). (b) $\delta^{18}\text{O}_c$ evolution from two cores located on either side of the Florida Current (blue for KNR166-2-26JPC; red for KNR166-2-73GC). Dots are observations and curves are model results. (c) $\delta^{18}\text{O}_w$ evolution from the two cores in (b). (d) $\delta^{18}\text{O}_T$ evolution from the two cores in (b). (e) The gradient (west - east) of $\delta^{18}\text{O}$ between the two cores: black for the $\delta^{18}\text{O}_c$, green for $\delta^{18}\text{O}_T$ and purple for $\delta^{18}\text{O}_w$. (f) The density gradient (west - east) between the two cores (black), the density gradient caused by the salinity gradient (purple) and the density gradient caused by the temperature gradient (green). (g) Meridional velocity at 530m in the Florida Straits. (h) The average barotropic streamfunction (BSF) at these two cores.....80

4.2.2 Regression coefficient of vertically averaged meridional velocity evolution on AMOC: (a) 0-500 m; (b) 500-1,000 m; (c) 1,000-2,400 m and (d) deeper than 2,400m.....82

4.2.3 The barotropic streamfunction during LGM (a) and HS1 (c). The Sverdrup transport calculated from surface wind stress (b) and (d).....83

4.2.4 (a) Correlation between the barotropic streamfunction (BSF) and AMOC. (b) Correlation between the barotropic streamfunction and Sverdrup transport. Topography is overlaid as black contours.....84

4.2.5 Evolutions of BSF (red) and Sverdrup transport (navy) from the locations indicated by the dots on Figure 4.2.3b.....	85
4.3.1 Density, $\delta^{18}\text{O}_c$, $\delta^{18}\text{O}_w$ and $\delta^{18}\text{O}_T$ profiles at the eastern (red) and western (navy) margin at 30°S in the Atlantic during modern climate, LGM and HS1 in the model. $\delta^{18}\text{O}_c$ observations are attached as colored dots. $\delta^{18}\text{O}_c$ values at observation sites are attached as colored cross.....	86
4.3.2 Atlantic zonal mean $\delta^{18}\text{O}_c$, $\delta^{18}\text{O}_w$ and $\delta^{18}\text{O}_T$ during modern climate, LGM and HS1.....	87
4.3.3 Zonal section at 30°S of $\delta^{18}\text{O}_w$, ϵ_{Nd} , $\delta^{13}\text{C}$ and radiocarbon age during present day, LGM and HS1. Black contours are the meridional velocity.....	88
4.3.4 Atlantic zonal mean ϵ_{Nd} during present day and LGM and the difference between LGM and present day in the model. Observations are overlaid as circles. Black contours are the Atlantic meridional overturning streamfunction.....	89
4.3.5 (a) $^{231}\text{Pa}/^{230}\text{Th}$ during present day (red) and LGM (navy): the average from 20°N - 60°N in the North Atlantic (curve) from model simulation; observations in the North Atlantic (dots); model $^{231}\text{Pa}/^{230}\text{Th}$ at observational sites (cross). (b) The difference of $^{231}\text{Pa}/^{230}\text{Th}$ between LGM and present day: the average from 20°N - 60°N in the North Atlantic (curve) from model simulation; observations (dots) and model values at observational sites (cross) (red for positive values and navy for negative values).....	90
4.3.6 $\delta^{13}\text{C}$ in the western Atlantic during present day (a) and LGM (b). Observations (Hesse et al., 2011) are overlaid as circles. (c) $\delta^{13}\text{C}$ in the North Atlantic during LGM (red) and present day (navy): average vertical profile of $\delta^{13}\text{C}$ in the western Atlantic (curve); observations (dot); model values at observational sites (cross).....	90
4.3.7 Time evolutions at 530 m at 30°S in CTRACE. (a) AMOC strength. (b) $\delta^{18}\text{O}_c$ evolution from the western (red) and eastern (navy) margin. (c) potential density evolution from the western (red) and eastern (navy) margin. (d) The gradient (west - east) of $\delta^{18}\text{O}$ between the two cores: black for the $\delta^{18}\text{O}_c$, green for $\delta^{18}\text{O}_T$ and purple for $\delta^{18}\text{O}_w$. (e) The potential density gradient (west - east) (black), the density gradient caused by the salinity gradient (purple) and the density gradient caused by the temperature gradient (green).....	92
4.3.8 Distribution of $\delta^{18}\text{O}_c$, $\delta^{18}\text{O}_w$ and $\delta^{18}\text{O}_T$, potential density, temperature and salinity at 530m during LGM, HS1 and the difference between HS1 and LGM.....	93
4.4.1 (a) Meridional velocity at 530m in the western boundary in the Atlantic during LGM (solid) and HS1 (dash). (b) The correlation between AMOC and the density gradient across the western boundary (red) and the Atlantic basin (navy) at 530m. (c) The	

correlation between AMOC and the $\delta^{18}\text{O}_c$ gradient across the western boundary (red) and the Atlantic basin (navy) at 530m. (d) The correlation between density gradient and $\delta^{18}\text{O}_c$ gradient across the western boundary (red) and the Atlantic basin (navy) at 530m. All the gradients are eastern value minus western value.....94

ABSTRACT

Ocean circulation during the last deglaciation can help us to improve the understanding of the mechanisms underlying the ocean circulation as well as test climate models to evaluate model credibility. However, previous model-data comparisons suffer from indirect comparison since reconstructions measures proxy records and climate model simulate physical variables. Since both reconstruction and climate model have uncertainties, it is difficult to address the model data discrepancies. To meet this challenge, my PhD work contributes to the isotope enabled Community Earth System Model (iCESM) project by developing a Neodymium (Nd) model and a Protactinium (^{231}Pa) and Thorium (^{230}Th) in the ocean model of CESM. Nd isotopic composition (ϵ_{Nd}) is being used increasingly as a tracer for water mass mixing and to reconstruct past ocean circulation changes. Sediment $^{231}\text{Pa}/^{230}\text{Th}$ activity ratio is an important proxy for deep ocean circulation rate. Under present day climate forcing, model Nd is able to capture the overall distribution of both ϵ_{Nd} and Nd concentration seen in the observations. Model ^{231}Pa and ^{230}Th activity and sediment $^{231}\text{Pa}/^{230}\text{Th}$ activity ratio are also in good agreement with available observations.

With the isotope enabled ocean model (iPOP2), I investigated two scientific questions: (1) How does the northward penetration of Antarctic Intermediate Water (AAIW) in the North Atlantic during the last deglaciation? (2) Can $\delta^{18}\text{O}_{\text{c}}$ be used to reconstruct past Atlantic Meridional Overturning Circulation (AMOC)?

(1) *Deglacial AAIW in the Atlantic*. AAIW plays important roles in the global climate system and the global ocean nutrient and carbon cycles. However, it is unclear how AAIW responds to global climate changes. In particular, neodymium isotopic composition (ϵ_{Nd}) reconstructions from different locations from the tropical Atlantic, have led to a debate on the relationship between northward penetration of AAIW into the tropical Atlantic and AMOC variability during the last deglaciation. We resolve this controversy by studying the transient oceanic evolution during the last deglaciation using a neodymium-enabled ocean model. Our results suggest a coherent response of AAIW and AMOC: when AMOC weakens, the northward penetration and transport of AAIW

decreases while its depth and thickness increase. Our study highlights that as part of the return flow of the North Atlantic Deep Water (NADW), the northward penetration of AAIW in the Atlantic is determined predominately by AMOC intensity. Moreover, the inconsistency among different tropical Atlantic ϵ_{Nd} reconstructions is reconciled by considering their corresponding core locations and depths, which were influenced by different water masses in the past. The very radiogenic water from the bottom of the Gulf of Mexico and the Caribbean Sea, which was previously overlooked in the interpretations of deglacial ϵ_{Nd} variability, can be transported to shallow layers during active AMOC, and modulates ϵ_{Nd} in the tropical Atlantic. Changes in the AAIW core depth must also be considered. Thus, interpretation of ϵ_{Nd} reconstructions from the tropical Atlantic is more complicated than suggested in previous studies.

(2) *Using $\delta^{18}Oc$ to reconstruct AMOC.* The vertical shear in the meridional flow is reflected by the zonal density contrast. Therefore, past circulation strength can be reconstructed by reconstructing ocean density gradients. $\delta^{18}Oc$ in foraminifera depends on the $\delta^{18}O$ in the water and the temperature and can be used to reconstruct density. $\delta^{18}Oc$ from the Florida Straits has been used to reconstruct AMOC evolution during the last deglaciation but the strength of Florida current can also be influenced by surface wind stress. Our model simulation suggests that in the western boundary, the Florida current strength is dominated by AMOC through the last deglaciation, which rules out the possibility of wind stress effect. Therefore, $\delta^{18}Oc$ contrast from the Florida Straits can be used to reconstruct past AMOC. However, in the South Atlantic, the basin-wide $\delta^{18}Oc$ contrast is decoupled from density contrast through the deglaciation in the upper ocean because of the deglacial density contrast change is dominated by salinity, which is caused by AAIW sinking to greater depth during HS1 and influencing the density in the western Atlantic. Although the model cannot simulate the different east-west contrast of $\delta^{18}Oc$ between LGM and present day in the observation, the example of deglacial decoupling of basin-wide $\delta^{18}Oc$ contrast from density contrast suggests that better constraints on the past water mass property are required to use $\delta^{18}Oc$ to reconstruct density.

1 Introduction

Ocean circulation plays a key role in controlling global climate mainly through modulating heat transport (e.g. Ganachaud and Wunsch, 2000) and carbon storage (e.g. Sabine et al., 2004). Understanding the responses of ocean circulation to different climate forcing perturbations is important for future climate predictions. However, instrumental observation (less than 200 years) covers only 0.1 millionth of the Earth's history and deep ocean response is in the order of millennia time scale. Therefore, studying ocean circulation changes in the past, which has much longer temporal coverage and also much greater variations, provides us with a good opportunity to improve our understanding of ocean's behavior. Furthermore, past ocean circulation also provides a good opportunity to test climate models. Whether climate models can simulate large and abrupt climate changes in the past helps to evaluate the credibility of models used for future predictions.

Climate during the Last Glacial Maximum (LGM) (26.5 ka – 19.0 ka) (Clark et al., 2009), when global ice sheets reached their maximum during the last glacial-interglacial cycle, was quite different from present day. For example, the global temperature is estimated to be 3°C ~ 5°C cooler than present day. The last transition from glacial to interglacial (the last deglaciation: ~19 ka - 10 ka) was punctuated by several large cooling and warming events: Heinrich Stadial 1 cooling (HS1, 17.5 ka – 14.7 ka), Bølling-Allerød warming (BA, 14.7 ka -12.7 ka) and Younger Dryas cooling (YD, ~12.7 ka) which is accompanied by abrupt changes in the Atlantic Meridional Overturning Circulation (AMOC) (Boyle and Keigwin, 1987; McManus et al., 2004). The large magnitude of changes and the abundance of different proxy records make the last deglaciation an ideal period to study the ocean circulation and test climate model.

Our knowledge of past ocean circulation changes relies on different proxy records. However, proxy records are not direct measurements of different climate variables and interpretation of different proxy records can be complicated by many other processes. Sometimes, interpretation of different proxy records can lead to opposite conclusions. In addition, the spatial resolution of ocean proxy records is limited. Therefore, combining paleo proxy records and climate models can improve our

knowledge about how ocean responded to different forcings in the past. Modeling efforts have been made to simulate past climate changes and contribute to our understanding of underlying mechanisms (e.g. He et al., (2013); Liu et al., (2009)). However, sometimes modeling results and proxy records can be contradictory. For example, global annual temperature reconstruction suggests a cooling trend through the middle to the late Holocene (Marcott et al., 2013) while model simulations suggest a warming trend in response to the ice sheet retreats and rising CO₂ (Liu et al., 2014). Since climate variables simulated by climate models cannot be compared with proxy reconstructions directly, considering both proxy records and model results have uncertainties, the direct model-data comparison is needed to better resolve the model data discrepancy and also help to explain some discrepancies in the reconstruction itself. Therefore, different isotopes have been implemented in climate models in the past decade to meet this challenge. This study develops two geotracers in the ocean components of the state-of-the-art Community Earth System Model (CESM) and uses this isotope-enabled ocean model to study the ocean circulation during the LGM and the last deglaciation.

1.1 ϵ_{Nd} as a Water Mass Tracer

Radiogenic ^{143}Nd is produced by the radioactive decay of ^{147}Sm with decay half-life of 106 billion years (Lugmair, 1974). During magma formation, Nd is more likely to enter magma than Sm, therefore, continents have lower Sm/Nd or $^{143}Nd/^{144}Nd$ compared with mantle (melt residue) and the bulk of earth. The difference of $^{143}Nd/^{144}Nd$ between continents and the bulk of earth increases with the age of the continent as $^{143}Nd/^{144}Nd$ in younger continents is more similar to the mantle. Therefore, younger (older) continents have higher (lower) $^{143}Nd/^{144}Nd$, which is more radiogenic (unradiogenic) (Goldstein and Hemming, 2003). Neodymium (Nd) isotopic composition (ϵ_{Nd}) is reported as Nd isotopic ratio ($^{143}Nd/^{144}Nd$) relative to the value of the bulk earth ($(^{143}Nd/^{144}Nd)_{CHUR} = 0.512638$)

(Jacobsen and Wasserburg, 1980), $\epsilon_{Nd} = \left[\frac{\left(\frac{^{143}Nd}{^{144}Nd} \right)_{sample}}{\left(\frac{^{143}Nd}{^{144}Nd} \right)_{CHUR}} - 1 \right] \times 10^4$. Due to the different

ages of continental crust, ϵ_{Nd} in continental crust varies geographically (Albarède and

Goldstein, 1992). The general feature consists of the two extremes, with the most unradiogenic values (minimum) in the North Atlantic (-10 to -14), the most radiogenic values (maximum) in the Pacific (-3 to -4), and intermediate values in the Indian and Southern Ocean (-7 to -10). Seawater derives its ϵ_{Nd} value mainly through weathering and erosion of continental crust (Piepgras et al., 1979). Therefore, different water masses from different locations have different ϵ_{Nd} values. In the modern ocean, ϵ_{Nd} value for the North Atlantic Deep Water (NADW) is ~ -13.5 , ϵ_{Nd} value for the Antarctic Intermediate Water (AAIW) and the Antarctic Bottom Water (AABW) is ~ -8.5 and ϵ_{Nd} value for water from the deep Pacific is ~ -3.5 (Amakawa et al., 2009; Piepgras and Wasserburg, 1987; Stichel et al., 2012). In the Atlantic, ϵ_{Nd} covaries with salinity (von Blanckenburg, 1999) and behaves as quasi-conservative water mass mixing tracer (Goldstein and Hemming, 2003; Piepgras and Wasserburg, 1982). Unlike proxies such as $\delta^{13}C$ and $^{231}Pa/^{230}Th$, which are also used to reconstruct past ocean circulation but subject to biological processes, ϵ_{Nd} is suggested to be minimally influenced by biological processes (Goldstein and Hemming, 2003). Therefore, ϵ_{Nd} has been increasingly used to trace different water masses in paleoceanographic studies (e.g. Piotrowski et al. 2004; Gutjahr et al. 2008; Roberts et al. 2010; Piotrowski et al. 2012).

However, the knowledge of processes controlling ϵ_{Nd} is still limiting a reliable application of ϵ_{Nd} as a paleo ocean circulation tracer. For example, groundwater (Johannesson and Burdige, 2007) and hydrothermalism (Zheng et al., 2016) can modify local seawater ϵ_{Nd} . In addition, the interpretation of the reconstructed ϵ_{Nd} changes in the Atlantic as water mass changes is based on the assumption that ϵ_{Nd} end-member changes can be neglected. However, NADW is formed by very unradiogenic Labrador Sea Water (< -20) and relative radiogenic water from Norwegian and Greenland Sea ($-7 \sim -10$) (Goldstein and Hemming, 2003). Uncertainty in the dominant deep water formation region in the past (Crockett et al., 2011; Dokken and Jansen, 1999; Labeyrie et al., 1992) leads to uncertainties in the end-member value of NADW (van de Flierdt et al., 2016), complicating the interpretation of ϵ_{Nd} changes seen in proxies. In addition, the magnitude and isotopic composition of Nd in sources, which have been suggested to be changing in the past (e.g. : Grousset et al. 1998; Harris and Mix 1999; Amakawa et al. 2000; Lézine

et al. 2005; Wolff et al. 2006; Rickli et al. 2010), may also influence ϵ_{Nd} in seawater (Tachikawa et al., 2003). Therefore, it is important to implement Nd isotopes into climate models to help improve our understanding of ϵ_{Nd} changes in the ocean, which can improve the interpretation of ϵ_{Nd} reconstructions.

1.2 $^{231}\text{Pa}/^{230}\text{Th}$ as a Proxy for AMOC Strength

^{231}Pa (32.5 ka half-life) and ^{230}Th (75.2 ka half-life) are produced at a constant rate approximately uniformly in the ocean by the α decay of ^{235}U and ^{234}U , respectively, with a production activity ratio of 0.093 (Henderson and Anderson, 2003). Water column ^{231}Pa and ^{230}Th are subject to particle scavenging and transport to sediments (Bacon and Anderson, 1982; Nozaki et al., 1987). Different scavenging efficiency results in different ocean residence time: ^{231}Pa has a residence time of approximately 111 years and ^{230}Th has a residence time of approximately 26 years (Yu et al., 1996). Longer residence time of ^{231}Pa than ^{230}Th makes ^{231}Pa more subject to ocean transport and therefore in the modern ocean about 45% of ^{231}Pa produced in the Atlantic is transported to the Southern Ocean (Yu et al., 1996), resulting a lower than 0.093 sediment $^{231}\text{Pa}/^{230}\text{Th}$ activity ratio in the North Atlantic and higher than 0.093 sediment $^{231}\text{Pa}/^{230}\text{Th}$ activity ratio in the Southern Ocean.

The application of the principle above to interpret sediment $^{231}\text{Pa}/^{230}\text{Th}$ as the strength of Atlantic meridional overturning circulation (AMOC), however, can be complicated by other factors, leading to uncertainties in using $^{231}\text{Pa}/^{230}\text{Th}$ as a proxy for past circulation (Keigwin and Boyle, 2008; Lippold et al., 2009; Scholten et al., 2008). In addition to the physical ocean transport, sediment $^{231}\text{Pa}/^{230}\text{Th}$ is also influenced by particle flux and composition (Chase et al., 2002; Geibert and Usbeck, 2004; Scholten et al., 2008; Siddall et al., 2007; Walter et al., 1997). The region of a higher particle flux tends to have a higher $^{231}\text{Pa}/^{230}\text{Th}$ (Kumar et al., 1993; Yong Lao et al., 1992), which is referred to as the “particle flux effect” (Siddall et al., 2005). Regional high particle flux in the water column will favor the removal of isotopes into the sediment, which leads to more isotopes transported into this region due to the down-gradient diffusive flux and subsequently more removal of isotopes into the sediment. With longer residence time for

^{231}Pa than ^{230}Th , ^{231}Pa is more subjective to this “particle flux effect”. Therefore, sediment $^{231}\text{Pa}/^{230}\text{Th}$ will be higher in high productivity regions. Also, the ability of opal to scavenge ^{231}Pa is stronger than that of ^{230}Th , resulting in the higher $^{231}\text{Pa}/^{230}\text{Th}$ in the high opal flux regions such as the Southern Ocean (Chase et al., 2002).

Furthermore, sediment $^{231}\text{Pa}/^{230}\text{Th}$ is suggested to record circulation change only within 1,000 m above the sediment, instead of the whole water column, complicating the interpretation of sediment $^{231}\text{Pa}/^{230}\text{Th}$ reconstructions (Thomas et al., 2006). For example, sediment $^{231}\text{Pa}/^{230}\text{Th}$ approaching 0.093 during HS1 from the subtropical North Atlantic is interpreted as the collapse of AMOC (McManus et al., 2004). If sediment $^{231}\text{Pa}/^{230}\text{Th}$ only records deepest water mass, it is possible that during HS1, AMOC gets shallower, as opposed to a fully collapse, and an increase of deep water imported from the Southern Ocean featuring high $^{231}\text{Pa}/^{230}\text{Th}$ can increase the sediment $^{231}\text{Pa}/^{230}\text{Th}$ approaching the production ratio (0.093) (Thomas et al., 2006). Therefore, it is important to incorporate ^{231}Pa and ^{230}Th into climate models for a direct model-data comparison and to promote a thorough understanding of sediment $^{231}\text{Pa}/^{230}\text{Th}$ as well as past ocean circulation.

1.3 Controversial AAIW Northward Penetration in the Atlantic during the Last Deglaciation

Antarctic Intermediate Water (AAIW) is a key component of the global ocean circulation. Large volume northward flowing AAIW plays an important role in northward nutrient transport to sustain primary production in North Atlantic (Palter and Lozier, 2008; Sarmiento et al., 2004). It also contributes to anthropogenic carbon sink (Gruber et al., 2009; Sabine, 2004) and ocean acidification (Ito et al., 2010; Resplandy et al., 2013). However, how the AAIW responds to global climate changes during the last deglaciation has remained poorly understood. In particular, how the AAIW interacts with the AMOC is highly controversial. There are only a few studies conducted on sediment cores bathed by modern AAIW and available data leads to opposite interpretations of variations of AAIW northward extend in the Atlantic during the last deglaciation.

The tropical Atlantic region is a key region of interaction between AAIW and the AMOC, where AAIW, as a part of the North Brazil Current (NBC), contributes significantly to the upper return branch of the AMOC (Lumpkin and Speer, 2003; Rintoul, 1991; Schmitz and McCartney, 1993; Zhang et al., 2011). Given AAIW as a part of the return flow of AMOC, the northward penetration of AAIW in the tropical Atlantic should be positively correlated with the AMOC strength, as suggested in some previous studies of deglacial AAIW (Came et al., 2008; Huang et al., 2014; Xie et al., 2012). However, other studies infer an enhanced AAIW penetration into the tropical Atlantic with a collapsed AMOC during the last deglaciation, or a negative correlation between the AAIW penetration and AMOC intensity (Pahnke et al., 2008; Rickaby and Elderfield, 2005; Zahn and Stüber, 2002). These contradictory studies are based on paleo reconstructions of ϵ_{Nd} and nutrient proxies such as $\delta^{13}\text{C}$ and Cd/Ca. One can argue that nutrient proxies can be complicated by processes such as organic matter remineralization (Kroopnick, 1980). However, ϵ_{Nd} reconstructions, which is minimally influenced by biological fractionation and is a quasi-conservative water mass tracer within Atlantic basin (Goldstein and Hemming, 2003), from three nearby tropical Atlantic sites show opposite evolution behaviors from the LGM to the HS1: ϵ_{Nd} decreases in some cores (Huang et al., 2014; Xie et al., 2012), but increases in some other cores (Pahnke et al., 2008) from LGM to HS1 (Figure 1.1). These opposite ϵ_{Nd} evolutions are interpreted as different AAIW northward penetration changes during North Atlantic cold events. Therefore, understanding why ϵ_{Nd} reconstructions at intermediate-depth vary is critical for understanding the deglacial response of AAIW.

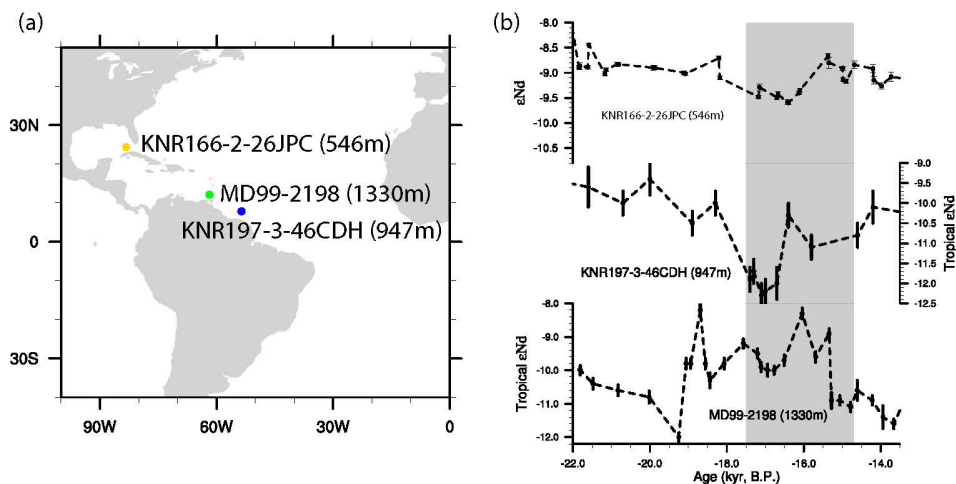


Figure 1.1 (a) Location of each ϵ_{Nd} reconstruction site in the tropical Atlantic. KNR166-2-26JPC: (24°19.62'N, 83°15.14'W, 546m) (Xie et al., 2012), yellow; MD99-2198: (12.09°N, 61.23°W, 1330m) (Pahnke et al., 2008), green; KNR197-3-46CDH: (7.836°N, 53.663°W, 947m) (Huang et al., 2014), blue. (b) Reconstructed ϵ_{Nd} evolutions at each site. HS1 is indicated by grey shading.

In addition to paleo reconstructions, some model studies simulate an increased AAIW transport into the North Atlantic in a counterclockwise shallow AAIW cell after the initial collapse of AMOC, further reinforcing the AMOC collapse (Saenko et al., 2003; Stouffer et al., 2007).

The different relationship between AAIW and the AMOC strength suggests different role of AAIW in AMOC: a positive correlation implies the AAIW penetration as a subsequent response to AMOC reorganization while a negative correlation indicates that the AAIW penetration may provide a positive feedback or a trigger for AMOC reorganization as more fresh water is transported to the North Atlantic by AAIW when AMOC is weak (Pahnke et al., 2008). In addition to paleo reconstructions, some model studies simulate an increased AAIW transport into the North Atlantic in a counterclockwise shallow AAIW cell after the initial collapse of AMOC, further reinforcing the AMOC collapse (Saenko et al., 2003; Stouffer et al., 2007), supporting the argument that AAIW can be a trigger for AMOC reorganization.

1.4 Can $\delta^{18}O_c$ Gradient be Used to Reconstruct AMOC Strength?

AMOC is considered to be one of the most important parts of the climate system because of its role in redistributing heat, carbon, and nutrients. In today's Atlantic, AMOC has two cells: an upper cell where northward flowing warm surface and intermediate water (upper 1,000 m) lose buoyancy in the North Atlantic and become southward flowing cold North Atlantic Deep Water (NADW) (1,500 – 4,500 m); a lower cell where Antarctic Bottom Water (AABW) formed in the Southern Ocean flows northward and gradually upwells into the NADW. How climate will change under anthropogenic forcing motivates us to study how AMOC has changed in the past, since climate changes on glacial-interglacial and millennial timescales are suggested to be coupled with changes in AMOC (e.g. Clark et al., 2002; Rahmstorf, 2002).

Efforts have been made to reconstruct past AMOC strength and geometry using different proxy records. Changes in the past circulation have been inferred from nutrient proxies such as $\delta^{13}\text{C}$ and Cd/Ca (e.g. Boyle and Keigwin, 1987; Keigwin and Lehman, 1994). But these tracers only provide information about the geometry and don't have constraints on the strength of the AMOC (LeGrand and Wunsch, 1995). Sediment $^{231}\text{Pa}/^{230}\text{Th}$ has been proposed to be a kinematic tracer for AMOC (Marchal et al., 2000; Yu et al., 1996) and has been used to infer AMOC strength in the past (e.g. Böhm et al., 2014; Gherardi et al., 2005, 2009; Hall et al., 2006; McManus et al., 2004) based on the assumption that stronger AMOC will transport more ^{231}Pa out of the North Atlantic, leaving sediment $^{231}\text{Pa}/^{230}\text{Th}$ in the North Atlantic smaller than the production ratio of 0.093. However, this approach has been contested as discussed in Chapter 1.2.

Another method to reconstruct AMOC intensity is using the density gradient based on the thermal wind relationship. Assuming geostrophic and hydrostatic balance, the horizontal density difference at a specific depth reflects the average vertical shear at this depth:

$$-\frac{f\rho_0}{g}L_x\left(\frac{\partial V}{\partial z}\right) = \rho_E - \rho_W, \text{ where } f \text{ is the Coriolis parameter, } \rho \text{ is seawater}$$

density, L_x is the horizontal width. The large scale northward surface flow and southward deep flow of AMOC is reflected in the basin-wide density gradient: the eastern margin is lighter than the western margin in the North Atlantic while the eastern margin is denser

than the western margin in the South Atlantic. Therefore, AMOC strength can be determined by measuring the density differences across the basin (Cunningham et al., 2007; Marotzke et al., 1999). Oxygen isotopic composition of calcite ($\delta^{18}\text{O}_c$) can be used to reconstruct density in the past (Lynch-Stieglitz et al., 1999). $\delta^{18}\text{O}_c$ is determined by the temperature and $\delta^{18}\text{O}$ of seawater ($\delta^{18}\text{O}_w$) in which the foraminifera calcify:

$$\delta^{18}\text{O}_c = \delta^{18}\text{O}_w - 0.27 + 0.0011t^2 - 0.245t + 3.58 \quad (\text{Marchitto et al., 2014}),$$

where t is temperature in $^{\circ}\text{C}$. In the upper ocean, $\delta^{18}\text{O}_w$ generally covaries with salinity. Therefore, with the increase of salinity and decrease of temperature, both $\delta^{18}\text{O}_c$ and density will increase.

$\delta^{18}\text{O}_c$ gradient among the western boundary has been used to reconstruct the AMOC strength during the last deglaciation (Lynch-Stieglitz et al., 2014). During HS1, AMOC is suggested to be collapsed in response to the icebergs discharge by $^{231}\text{Pa}/^{230}\text{Th}$ reconstruction from Bermuda Rise (McManus et al., 2004). However, radiocarbon reconstruction from subtropical North Atlantic suggests suppressed deep ventilation but not as much as the LGM (Keigwin and Boyle, 2008). Benthic $\delta^{13}\text{C}$ and $\delta^{18}\text{O}$ from Northeast Atlantic imply a still active AMOC during the HS1 (Oppo et al., 2015). $\delta^{18}\text{O}_c$ gradient across Florida Straits is reduced during HS1 and YD, which indicates the weakening of the flow through the straits during this time period. However, the strength of the flow through the Florida Straits can be influenced by both wind-driven subtropical gyre and AMOC and it is hard to exclude the possibility that the flow through the Florida Straits reflects the wind-driven flow strength instead of the AMOC evolution.

$\delta^{18}\text{O}_c$ at eastern and western boundary of the South Atlantic at 27°S has also been used to reconstruct AMOC strength during the LGM (Lynch-Stieglitz et al., 2006). At present day, in the South Atlantic, the eastern margin $\delta^{18}\text{O}_c$ is higher than the western margin, which is consistent with the denser water in the eastern margin. During LGM, AMOC is suggested to be active but shallower than present day, with southward flow of NADW replaced by the Glacial North Atlantic Intermediate Water (GNAIW) (Boyle and Keigwin, 1987; Curry and Oppo, 2005; Marchitto and Broecker, 2006), which would suggest much larger $\delta^{18}\text{O}_c$ in the eastern margin than the western margin. However, $\delta^{18}\text{O}_c$

in the eastern margin is smaller than the western margin (Lynch-Stieglitz et al., 2006) for upper 1,000m at 27°S. If $\delta^{18}\text{O}_{\text{c}}$ gradient in the benthic foraminifera still represents the density gradient, it is incompatible with the shallower and active AMOC in the Atlantic.

1.5 Objectives of my PhD Study

The objectives of my PhD study are:

(1) Implementing the Nd isotopes, ^{231}Pa and ^{230}Th in the ocean component of CESM, which is the Parallel Ocean Program version 2 (POP2) (Danabasoglu et al., 2012). Other tracers, such as $\delta^{18}\text{O}$ (Zhang et al., 2017), $\delta^{13}\text{C}$ and radiocarbon (Jahn et al., 2015) have been implemented in POP2. With additional Nd, ^{231}Pa and ^{230}Th , POP2 is facilitated with the most widely used isotopes in paleoceanography. Therefore, the isotope-enabled POP2 (iPOP2) will provide a new tool which can help to improve the understanding of past ocean circulation.

(2) Study how the AAIW northward penetration in the Atlantic evolves during the last deglaciation using a transient ocean simulation. With the new Nd module in POP2, the contradictory ϵ_{Nd} evolutions from three nearby tropical Atlantic sites can be investigated.

(3) Study how well can $\delta^{18}\text{O}_{\text{c}}$ gradient represent density gradient to reconstruct AMOC strength. Specifically, can $\delta^{18}\text{O}_{\text{c}}$ gradient evolution across the Florida Straits represent the AMOC evolution during the last deglaciation? How to reconcile the reversed $\delta^{18}\text{O}_{\text{c}}$ gradient compared with present day at 27°S in the South Atlantic with shallower but active AMOC suggested by other tracers during LGM? Lastly, how well in general can $\delta^{18}\text{O}_{\text{c}}$ gradient across the basin and across the west boundary represent AMOC strength.

This dissertation is arranged in the following way. The model development and model validation of Nd isotopes and ^{231}Pa and ^{230}Th , as well as the transient simulation are presented in Chapter 2. Chapter 3 will explore the deglacial AAIW evolution. Chapter 4 will study using $\delta^{18}\text{O}_{\text{c}}$ to represent AMOC intensity. Finally, conclusions and future perspectives will be discussed in Chapter 5. Currently, Chapter 2 and Chapter 3 have

already been published in different journals. The Nd isotope development is published in the Geoscientific Model Development Discussion (Gu et al., 2017b). The ^{231}Pa and ^{230}Th development is published in the Geoscientific Model Development (Gu and Liu, 2017). The deglacial AAIW evolution is published in Paleoceanography (Gu et al., 2017a).

2. Isotope-enabled Ocean Model Development

2.1 Neodymium Isotope Development

Nd isotopes have been simulated in previous modeling studies (Arsouze et al., 2009; Jones et al., 2008; Rempfer et al., 2011; Siddall et al., 2008). Jones et al., 2008 simulates ϵ_{Nd} using an offline ocean circulation model and prescribed surface ϵ_{Nd} . Approaches in Siddall et al., 2008, Arsouze et al., 2009 and Rempfer et al., 2011 are similar except that Arsouze et al., 2009 uses a fully prognostic coupled dynamic and biogeochemical model and Rempfer et al., 2011 uses a cost-efficient model which enables a thorough investigation of the Nd cycle. The implementation of Nd isotopes in POP2 follows previous modeling schemes (Arsouze et al., 2009; Rempfer et al., 2011; Siddall et al., 2008).

2.1.1 Physical Ocean Model and the Biogeochemical Component in POP2

POP2 is the ocean component of the CESM, which is a state-of-the-art coupled climate model. Studies describing model components and analyzing results can be found in a special collection in Journal of Climate (<http://journals.ametsoc.org/topic/ccsm4-cesm1>). In the development of Nd isotopes, the ocean-alone simulation is applied, which is the ocean model coupled to data atmosphere, land, ice and river runoff under the normal year forcing of CORE-II data (Large and Yeager, 2008), using the low-resolution version of POP2 with a nominal 3° horizontal resolution and 60 vertical layers.

CESM has incorporated a marine ecosystem module that simulates biological variables (Moore et al., 2013). The marine ecosystem module has been validated against

present day observations extensively (e.g. Doney et al., 2009; Long et al., 2013; Moore et al., 2002, 2004; Moore and Braucher, 2008). The implementation of Nd isotopes requires particle fields: CaCO_3 , opal, particulate organic carbon (POC) and dust. These particle fields can be obtained through the ecosystem driver from the ecosystem module (Jahn et al., 2015). The ecosystem module simulates the particle fluxes in reasonable agreement with the present-day observations. The pattern and magnitude of the annual mean particle fluxes (CaCO_3 , opal, POC) leaving the euphotic zone at 105m are similar to the satellite observations (Fig. 7.2.5 and 9.2.2 in Sarmiento and Gruber 2006) (Figure 2.1.1 a~c): particle fluxes are higher in the high productivity regions such as high latitudes and equatorial Pacific; opal flux is high in the Southern Ocean. The remineralization scheme of the particle is based on the ballast model of Armstrong et al., (2002). Detailed parameterizations for particle remineralization are documented in Moore et al., (2004) with temperature dependent remineralization length scales for POC and opal. Surface dust deposition is taken from the ecosystem module, which is prescribed monthly surface dust flux from Luo et al., (2003) (Figure 2.1.1 d).

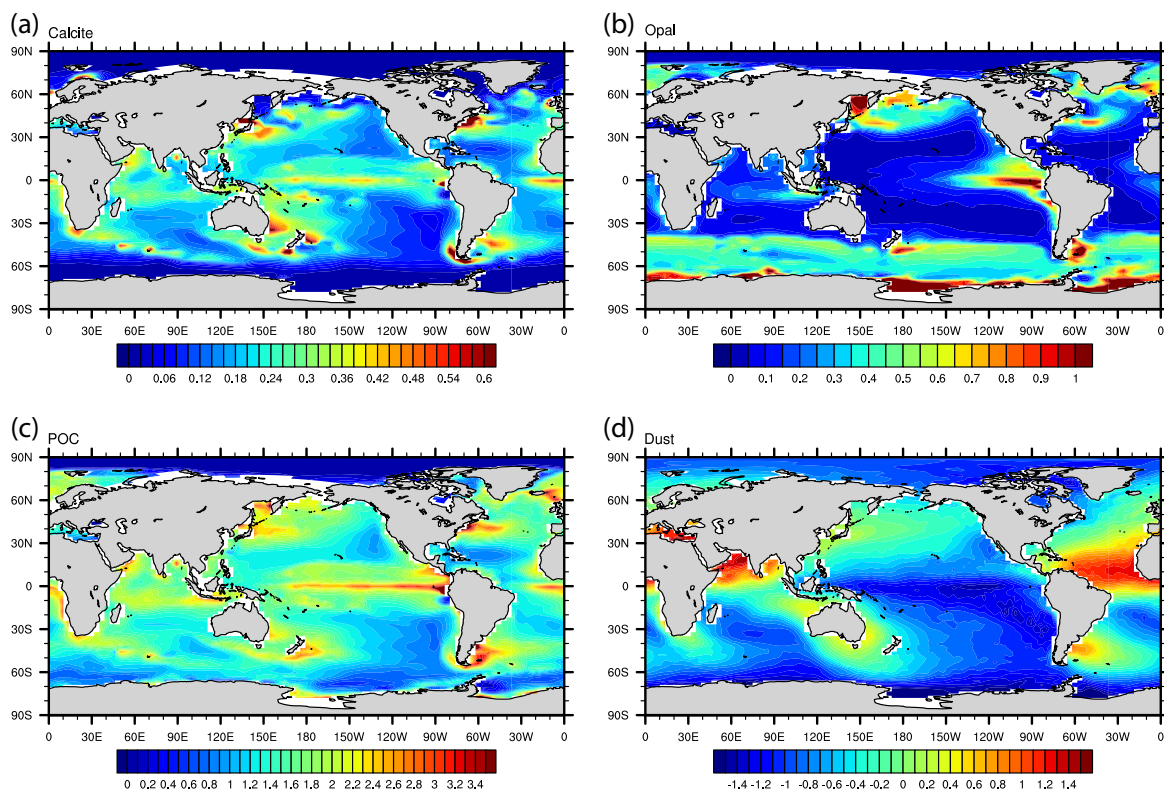


Figure 2.1.1 Annual mean particle fields produced by the ecosystem module in the CESM under present day forcing. (a) CaCO_3 flux at 105m ($\text{mol m}^{-2} \text{yr}^{-1}$). (b) Opal flux at 105m ($\text{mol m}^{-2} \text{yr}^{-1}$). (c) POC flux at 105m ($\text{mol m}^{-2} \text{yr}^{-1}$). (d) Log_{10} values of annual atmospheric dust deposition ($\text{g m}^{-2} \text{yr}^{-1}$).

2.1.2 Neodymium implementation

Two versions of Nd isotopes are implemented: one is the standard Nd isotope, which is coupled with the active marine biogeochemical module (p-coupled Nd); the other is the auxiliary Nd isotope with prescribed particle fluxes (p-fixed Nd). With these two versions of Nd, the potential effect of productivity change on ϵ_{Nd} distribution can be studied. The p-fixed version also provides a computationally efficient tool for sensitivity studies.

The sources of Nd in the ocean include surface dust, river and weathering of continental crust. Monthly surface dust deposition (F_{dust}) is prescribed using Luo et al.,

(2003). The Nd concentration (C_{dust}) in the dust is assumed to be 20 $\mu\text{g/g}$ (Goldstein et al., 1984; Grousset et al., 1988, 1998), of which 2% (β_{dust}) can be released into the ocean (Greaves et al., 1994). Therefore, the dust source (S_{dust}) can be calculated as

$$S_{dust} = \frac{F_{dust} \times C_{dust} \times \beta_{dust}}{dz1}, \quad (\text{Eq 2.1})$$

where $dz1$ is the thickness of the surface layer. The simulated river runoff (ROFF) from the coupler is used as river discharge. The Nd concentration (C_{river}) in river discharge is prescribed following Goldstein and Jacobsen, (1987). 30% (γ_{river}) of Nd in the river runoff can enter the ocean through estuaries (Rempfer et al., 2011). The river source (S_{river}) can therefore be calculated as

$$S_{river} = \frac{ROFF \times C_{river} \times \gamma_{river}}{dz1}. \quad (\text{Eq 2.2})$$

A boundary source is applied to the continental margin, in the upper 3,000 m in the ocean (Arsouze et al., 2007). The boundary source in Arsouze et al., (2009) is assumed to be depth dependent, which is not supported by observations (van de Flierdt et al., 2016). Therefore, following Rempfer et al., (2011), a globally uniform constant value for the boundary source per unit area is assumed. The total boundary source ($f_{boundary}$) is a tuning parameter in Rempfer et al., 2011. The boundary source ($S_{boundary}$) can be calculated as

$$S_{boundary} = \frac{f_{boundary}}{A_{tot}} \times \frac{1}{dz}, \quad (\text{Eq 2.3})$$

where A_{tot} is the total area of the continental margin and dz is the thickness of the grid.

^{143}Nd and ^{144}Nd are simulated as two tracers in the model (Eq 2.4). ^{143}Nd and ^{144}Nd account for 36% of total Nd. Individual fluxes for ^{143}Nd and ^{144}Nd can be calculated using the isotopic ratio (IR) (Eq 2.5). IR in the dust source is prescribed following Tachikawa, Athias, and Jeandel (2003). IR in the river source and the boundary source is prescribed from Jeandel et al., (2007).

$$\text{Nd} = ^{143}\text{Nd} + ^{144}\text{Nd} \quad (\text{Eq 2.4})$$

$$\text{IR} = ^{143}\text{Nd}/^{144}\text{Nd} \quad (\text{Eq 2.5})$$

The internal cycling of Nd is modeled using the reversible scavenging by sinking particles (Bacon and Anderson, 1982). Unlike the quasi-conservative behavior of ϵ_{Nd} , Nd concentration shows a nutrient-like distribution as it increases with depth and along

circulation pathway, which is suggested to be caused by reversible scavenging (Siddall et al., 2008). Reversible scavenging describes the adsorption of the isotopes onto sinking particles and the desorption when the particle is dissolved. The particles involved in the reversible scavenging of Nd are CaCO₃, opal, POC and dust. The particle fluxes can be computed by the biogeochemical module, which is the p-coupled Nd, or can be prescribed using the particle fluxes generated by the biogeochemical module under modern climate, which is the p-fixed Nd.

The reversible scavenging (S_{rs}) considers total Nd ($[Nd]_t^i$, where i denotes ¹⁴³Nd and ¹⁴⁴Nd) as dissolved Nd ($[Nd]_d^i$) and particulate Nd ($[Nd]_p^i$) associated with different particle types ($[Nd]_{p,j}^i$, where j denotes CaCO₃, opal and POC and dust (Eq 2.6)).

$$[Nd]_t^i = [Nd]_d^i + [Nd]_p^i = [Nd]_d^i + \sum_j [Nd]_{p,j}^i \quad (\text{Eq 2.6})$$

$[Nd]_d$ and $[Nd]_p$ are assumed to be in equilibrium and the ratio between $[Nd]_d$ and $[Nd]_p$ is controlled by the partition coefficient (K) and the ratio (R_j) between particle concentration (C_j) and the density of seawater (1024.5 kg m⁻³) (Eq 2.7). K_j value for different particles can be calculated by another tuning parameter ($\frac{[Nd]_p}{[Nd]_d}$) and the average R_j (Eq 2.8). Assuming there is no differentiation during the reversible scavenging due to the similar molecule mass of ¹⁴³Nd and ¹⁴⁴Nd, the same K_j is applied to ¹⁴³Nd and ¹⁴⁴Nd. Reversible scavenging transport $[Nd]_p$ downward by the settling velocity (w) of 1000 m yr⁻¹ (Arsouze et al., 2009; Dutay et al., 2009; Kriest, 2002; Rempfer et al., 2011) (Eq 2.9). Combining Eq 2.6 and 2.7, we can get $[Nd]_p$ (Eq. 10). In the bottom layer, $[Nd]_p$ is removed from the ocean, which acts as the sink for the Nd budget.

$$\frac{[Nd]_{j,p}^i}{[Nd]_d^i} = K_j^i \times R_j \quad (\text{Eq 2.7})$$

$$K_j = \left(\frac{[Nd]_p}{[Nd]_d}\right) \times \frac{1}{R_{j,avg}} \quad (\text{Eq 2.8})$$

$$S_{rs} = -\frac{\partial(w[Nd]_p)}{\partial z} \quad (\text{Eq 2.9})$$

$$[Nd]_p^i = [Nd]_t^i \times \left(1 - \frac{1}{1 + \sum_j K_j^i \times R_j}\right), \quad (\text{Eq 2.10})$$

The total conservation equation for Nd can be written as

$$\frac{\partial [Nd]_t^i}{\partial t} = S_{dust}^i + S_{river}^i + S_{boundary}^i + S_{rs}^i + \text{Transport} \quad (\text{Eq 2.11})$$

2.1.3 Parameter Tuning and Model Validation

Following Rempfer et al., (2011), the Nd model is tuned with two parameters: f_{boundary} and $\frac{[Nd]_p}{[Nd]_d}$. 99 sets of experiments are run with different combinations of f_{boundary} and $\frac{[Nd]_p}{[Nd]_d}$ to search for the optimal set of parameters that can simulate both Nd concentration and ϵ_{Nd} most consistent with available observations. f_{boundary} is varied among 1×10^9 , 2×10^9 , 3×10^9 , 4×10^9 , 5×10^9 , 5.5×10^9 , 6×10^9 , 7×10^9 , 8×10^9 and $\frac{[Nd]_p}{[Nd]_d}$ is varied among 2×10^{-4} , 4×10^{-4} , 6×10^{-4} , 8×10^{-4} , 9×10^{-4} , 10×10^{-4} , 11×10^{-4} , 12×10^{-4} , 14×10^{-4} , 16×10^{-4} , 18×10^{-4} . For computational efficiency purposes, there is only p-fixed Nd in these experiments. To evaluate the performance of each parameter combination, the cost function of $[Nd]_d$ and ϵ_{Nd} is used, as in Rempfer et al., (2011);

$$J = \frac{1}{N} \sum_{k=1}^N |obs_k - model_k| \quad (\text{Eq 2.12})$$

where k represents each observational point, N is the total number of observational points, obs_k is the observational $[Nd]_d$ or ϵ_{Nd} and $model_k$ is the model $[Nd]_d$ or ϵ_{Nd} at the observational location. The observations used for comparison are compiled from van de Fliedert et al., (2016).

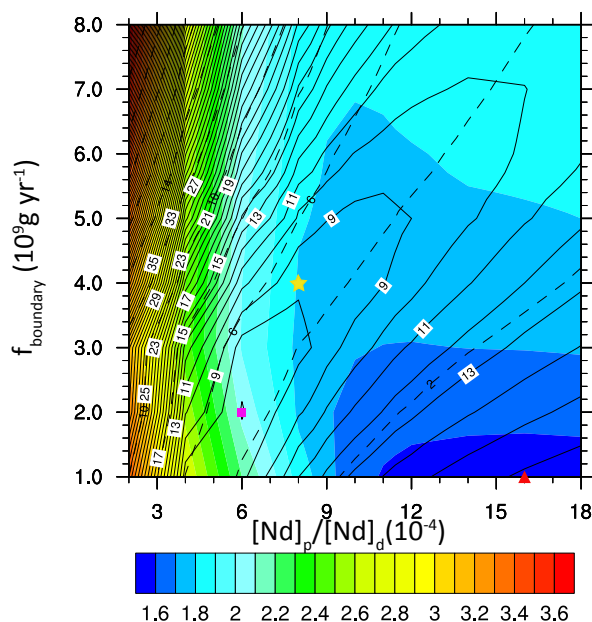


Figure 2.1.2 Contours of cost function of $[\text{Nd}]_d$ ($J_{[\text{Nd}]_d}$: solid lines, unit: pmol kg^{-1}) and ϵ_{Nd} ($J_{\epsilon_{\text{Nd}}}$: color, unit: ϵ_{Nd} units) and total Nd inventory (dashed lines, unit: 10^{12}g) for different combinations of f_{boundary} and $\frac{[\text{Nd}]_p}{[\text{Nd}]_d}$ at the end of each experiment. $J_{[\text{Nd}]_d}$ reaches minimum at the pink square; $J_{\epsilon_{\text{Nd}}}$ reaches minimum at the red triangle; CTRL is indicated by the yellow star.

The cost function J measures the average deviation of the simulated $[\text{Nd}]_d$ or ϵ_{Nd} from observation (Figure 2.1.2). As pointed out by Rempfer et al., (2011), it is not possible to have a setup of f_{boundary} and $\frac{[\text{Nd}]_p}{[\text{Nd}]_d}$ that can minimize both $J_{[\text{Nd}]_d}$ and $J_{\epsilon_{\text{Nd}}}$ simultaneously. In POP2, when $J_{[\text{Nd}]_d}$ reaches the minimum, the overall performance of ϵ_{Nd} is not good enough and when $J_{\epsilon_{\text{Nd}}}$ reaches the minimum, $[\text{Nd}]_d$ is too far away from the observations. Therefore, after further examination of the distributions of $[\text{Nd}]_d$ and ϵ_{Nd} as well as the cost functions in other parameter settings, the combination that relatively better simulating both reasonable $[\text{Nd}]_d$ and ϵ_{Nd} distributions is chosen as the control experiment (CTRL) (Figure 2.1.2 yellow star). The f_{boundary} used in CTRL is $4 \times 10^9 \text{ g yr}^{-1}$ and $\frac{[\text{Nd}]_p}{[\text{Nd}]_d}$ is 0.0009, which is similar to $5.5 \times 10^9 \text{ g yr}^{-1}$ and 0.001, respectively, in Rempfer et al., (2011).

The Nd inventory in CTRL is 4.3×10^{12} g, which is in agreement with the estimation in Arsouze et al., (2009) and Tachikawa et al., (2003). The residence time of Nd is 785 year, which also agrees with Siddall et al., (2008) and Tachikawa et al., (2003).

CTRL can simulate the general feature of Nd concentration, in good agreement with observations. Nd concentration in CTRL increases with depth and along the circulation pathway from the North Atlantic to the North Pacific (Figure 2.1.3 and 2.1.4), which is the same as observations.

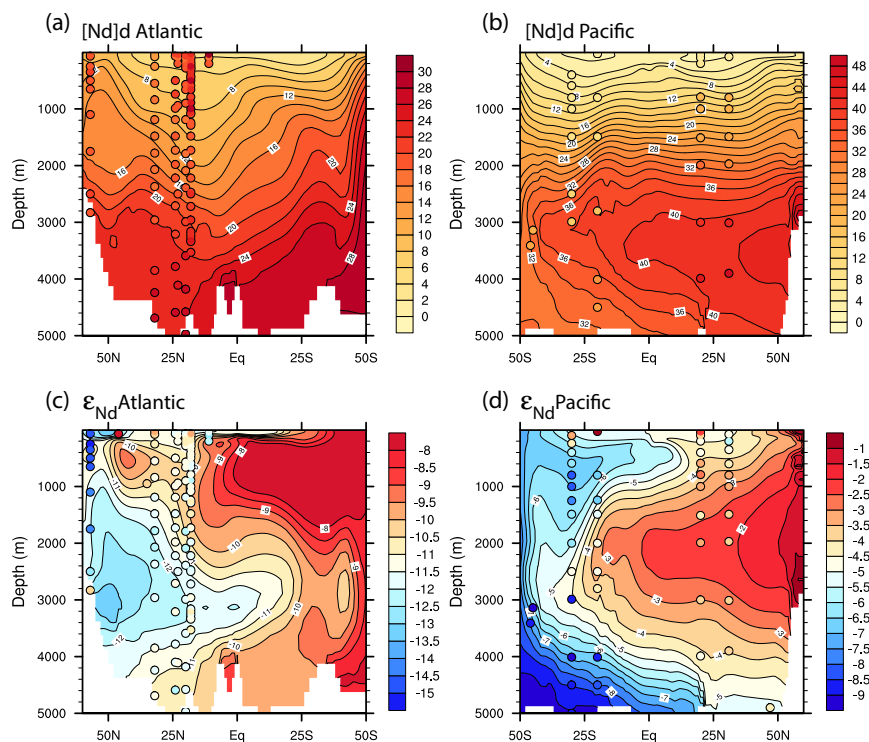


Figure 2.1.3 Nd concentration (a and b) and ϵ_{Nd} (c and d) in the vertical section in the Atlantic ($20^{\circ}W$ - $30^{\circ}W$) and the Pacific ($150^{\circ}W$ - $160^{\circ}W$) in CTRL. Observations are superimposed as filled circles using the same color scale.

The largest Nd concentration is in the abyssal North Pacific. Vertical profiles of Nd concentration overall have the right magnitude compared with observations (Figure 2.1.4). However, Nd concentration in CTRL is generally smaller than in observations in the surface layer of all ocean basins and larger than observation in the deep ocean, especially in the Pacific (Figure 2.1.6). This depleted Nd concentration in the surface ocean compared with observations was also found in previous Nd modeling studies (Arsouze et

al., 2009; Rempfer et al., 2011), probably because similar approaches are applied. The correlation between model Nd concentration and observational Nd concentration is 0.65 (N = 851) in the Atlantic, 0.67 (N = 668) in the Pacific and 0.57 (N = 180) in the Indian Ocean.

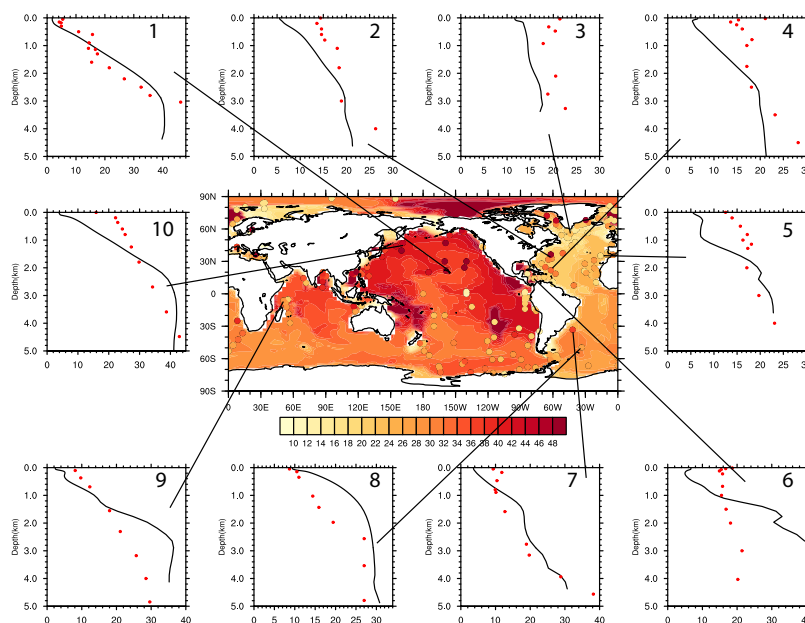


Figure 2.1.4 Seafloor Nd concentration in CTRL. Observations are superimposed as filled circles using the same color scale. Selected Nd concentration profiles are also shown: black line for CTRL and red dot for observation.

The ϵ_{Nd} distribution in CTRL, which agrees well with observations, shows different water mass property. Vertical section of ϵ_{Nd} in the Atlantic shows the southward propagation of unradiogenic NADW and northward movement of radiogenic AAIW and AABW (Figure 2.1.3c). In the Pacific, the distribution of ϵ_{Nd} shows the southward traveling radiogenic North Pacific Deep Water and northward moving AAIW and AABW (Figure 2.1.3d). Seafloor ϵ_{Nd} shows the most radiogenic water in the North Pacific and the most unradiogenic water in the North Atlantic, more specifically, the Labrador Sea. This inter-basin gradient in ϵ_{Nd} is well produced in CTRL (Figure 2.1.5). Most vertical profiles of ϵ_{Nd} reproduce the vertical changes of ϵ_{Nd} in the observations (Figure 2.1.5), especially the “zig-zag” pattern (Goldstein and Hemming, 2003) in the Atlantic (Figure

2.1.5 profile 2, 4, 5 and 7), showing the vertically alternating water mass from AAIW to NADW to AABW.

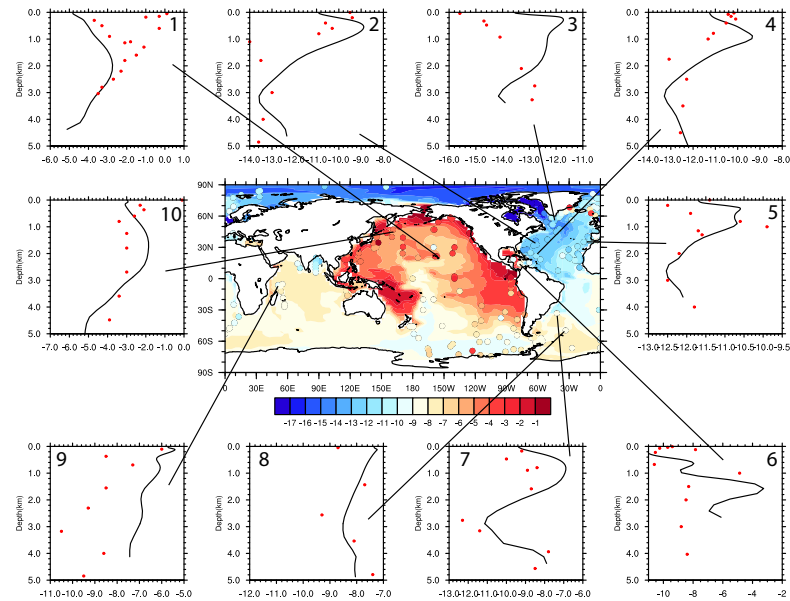


Figure 2.1.5 Seafloor ϵ_{Nd} in CTRL. Observations are superimposed as filled circles using the same color scale. Selected ϵ_{Nd} profiles are also shown: black line for CTRL and red dot for observation.

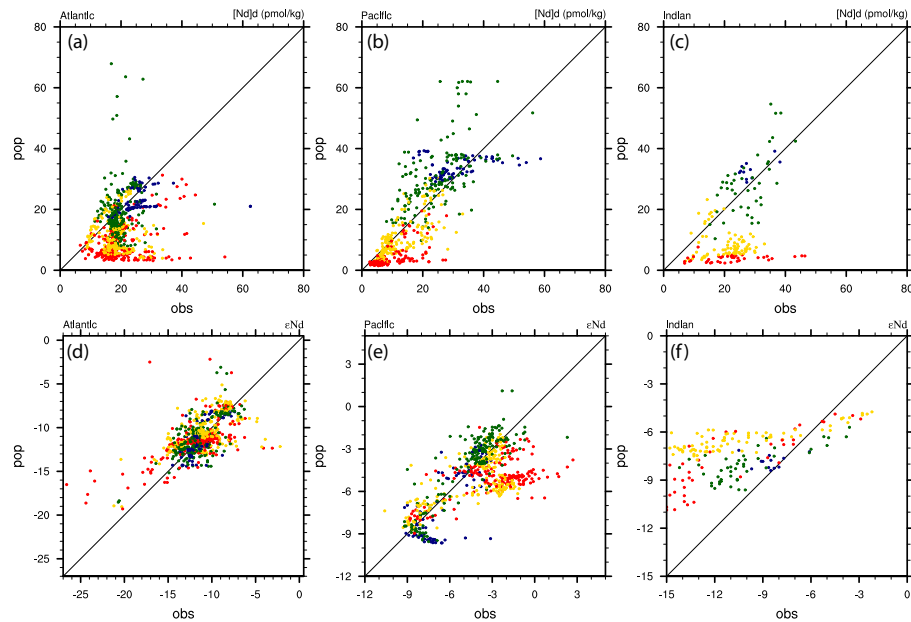


Figure 2.1.6 Scatter plot of Nd concentration (a, b and c) and ϵ_{Nd} (d, e and f) between observations and CTRL in different ocean basins. Southern Ocean is included in each Atlantic, Pacific and Indian Ocean section. Observations in different depth ranges are indicated by different

colors: 0-200m (red), 200-1000m (yellow), 1000-3000m (green) and depth deeper than 3000m (navy).

Quantitatively, the linear regression coefficient can be used to indicate the model ability to simulate ϵ_{Nd} . ϵ_{Nd} is in better agreement with observations in the Atlantic and the Pacific than in the Indian Ocean (Table 2.1.1). In the Atlantic and the Pacific, ϵ_{Nd} is better simulated below 1,000m than upper 1,000m (Table 2.1.1). The largest deviations from observation are mainly found in the upper 1000m (Figure 2.1.5 and Table 2.1.1). Since the surface ϵ_{Nd} in the observation is much more variable than in deeper water (Goldstein and Hemming, 2003) and the upper 1000m ϵ_{Nd} is influenced by surface sources (dust source and river source) (Rempfer et al., 2011), the large model data discrepancy in the upper 1000m is probably caused by the bias in the IR prescribed for the dust source and river source. However, the surface sources can only influence the upper 1000m, as below 1000 m ϵ_{Nd} is mainly controlled by the boundary source (Rempfer et al., 2011). ϵ_{Nd} in CTRL agrees well with observations below 1000m in the Atlantic and Pacific (Table 2.1.1 and Figure 2.1.5 and 2.1.6). Since most of the reconstructions are located at intermediate and deep depth, model ϵ_{Nd} bias in the surface layers is not as important as biases at intermediate and deep depths. However, due to this bias, using our model to help interpret data from surface layers should be cautious.

	Atlantic		Pacific		Indian	
	N	rc	N	rc	N	rc
Total	851	0.54	668	0.56	180	0.23
0-200m	250	0.43	177	0.32	41	0.38
200-1000m	264	0.47	196	0.47	82	0.16
1000-3000m	254	0.75	207	0.97	45	0.29
>3000m	83	0.98	88	1.05	12	0.04

Table 2.1.1 The linear regression coefficient (rc) between model ϵ_{Nd} and observational ϵ_{Nd} in different ocean basins at different depth range: 0-200m, 200-1000m, 1000-3000m and depth deeper than 3000m. N is the number of points.

Atlantic zonal mean ϵ_{Nd} covaries with salinity in CTRL (Figure 2.1.7a), which is consistent with observation and indicates the ability of ϵ_{Nd} to trace different water masses

(Goldstein and Hemming, 2003). However, compared with salinity, ϵ_{Nd} is shifted to a deeper depth, which is attributed to reversible scavenging transporting ϵ_{Nd} values downward in Rempfer et al., (2011). The “zig-zag” pattern in the South Atlantic mean ϵ_{Nd} profile shows different water masses at different depths. With the increase of $\frac{[Nd]_p}{[Nd]_d}$, which is an increase in strength of reversible scavenging, the ϵ_{Nd} values are increasingly shifted downward (Figure 2.1.7b). This downward shift is stronger in the upper ocean than in the deep ocean because the larger particle fluxes in the upper ocean lead to a stronger reversible scavenging.

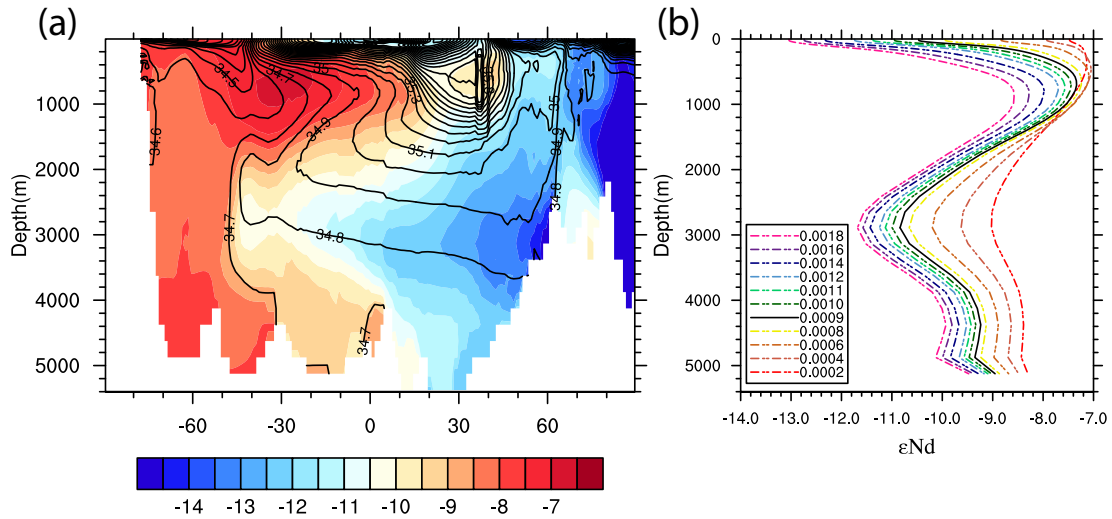


Figure 2.1.7 (a) Atlantic zonal mean p-fixed ϵ_{Nd} (color) and salinity (contour). (b) South Atlantic (0°S-30°S) mean p-fixed ϵ_{Nd} vertical profile in different experiments with varying $\frac{[Nd]_p}{[Nd]_d}$ ($f_{\text{boundary}} = 4 \times 10^9 \text{ g yr}^{-1}$).

2.1.4 ϵ_{Nd} in Idealized Hosing Experiment

To test how ϵ_{Nd} responds to the change of AMOC strength and study whether the productivity change will influence ϵ_{Nd} distribution (Rempfer et al., 2011), idealized fresh water forcing experiment (HOSING) is carried out with both p-fixed and p-coupled Nd. 1 Sv of fresh water is applied to 50°N-70°N in the North Atlantic. HOSING is initialized

from CTRL and run for 1400 model years. The f_{boundary} and $\frac{[Nd]_p}{[Nd]_d}$ used in HOSING are the same as in CTRL.

In response to the 1 Sv fresh water forcing in the North Atlantic in HOSING, AMOC strength reduces from 16 Sv in CTRL (AMOC_{on} state) to 2 Sv (AMOC_{off} state) (Figure 2.1.8). Before discussing the p-coupled ϵ_{Nd} in HOSING, which includes effects from changes in the particle flux and the circulation, the p-fixed ϵ_{Nd} response is discussed, which is caused purely by the circulation change.

The p-fixed ϵ_{Nd} in the Atlantic during the AMOC_{off} state shows less southward penetration of NADW and less northward penetration of AAIW (Figure 2.1.9b). The “zig-zag” pattern is reduced in the vertical profile of ϵ_{Nd} in the Atlantic (Figure 2.1.10 green line), indicating less water mass penetration. The difference of p-fixed ϵ_{Nd} between AMOC_{off} and AMOC_{on} is shown in Figure 2.1.9c. The pattern of changes resembles the result in Rempfer et al., (2012). In the upper 1000m, the maximum change towards more unradiogenic ϵ_{Nd} values (about -4 ϵ_{Nd} unit) is located at the equator. In 1000m to 3000m depth range, the most radiogenic change (about 3 ϵ_{Nd} unit) is located at 30° S. With the fresh water forcing in the North Atlantic, the formation of NADW is greatly inhibited and less unradiogenic NADW is transported to the South Atlantic. Therefore, p-fixed ϵ_{Nd} in the South Atlantic experiences a radiogenic shift. Below 4000m, AABW shows a radiogenic change (about 1 ϵ_{Nd} unit), which is much more uniform across different latitudes than in the upper ocean because of little change in the strength of the lower cell of AABW (Figure 2.1.9a and b). Overall, p-fixed ϵ_{Nd} in HOSING suggests weakened northward penetration of AAIW and weakened southward penetration of NADW due to the weakening of AMOC.

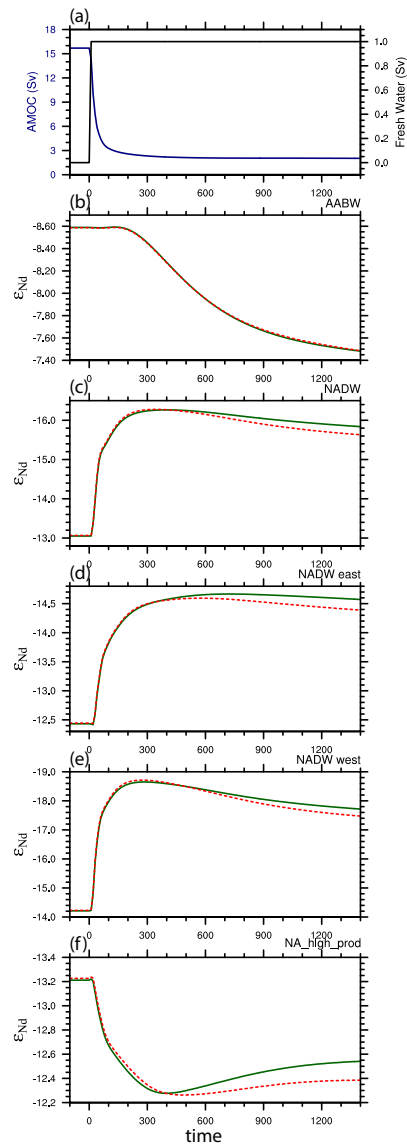


Figure 2.1.8 Time evolutions (decadal mean) in HOSING. (a) Fresh water forcing (black) and AMOC strength (navy). (b) ϵ_{Nd} value for AABW end-member, which is calculated as the average of 60°S - 70°S below 4000m. (c) ϵ_{Nd} value for NADW end-member, which is calculated as the average of 50°N - 60°N between 2500m to 3000m. (d) ϵ_{Nd} value for NADW in the east Atlantic, which is calculated as the average of 50°N - 60°N between 2500m to 3000m east of 20°W . (e) ϵ_{Nd} value for NADW in the west Atlantic, which is calculated as the average of 50°N - 60°N between 2500m to 3000m west of 50°W . (f) ϵ_{Nd} value at 2890m at (40°N , 40°W), where productivity experiences great changes in HOSING. In the ϵ_{Nd} time series (b-f), green is p-fixed ϵ_{Nd} and red is p-coupled ϵ_{Nd} .

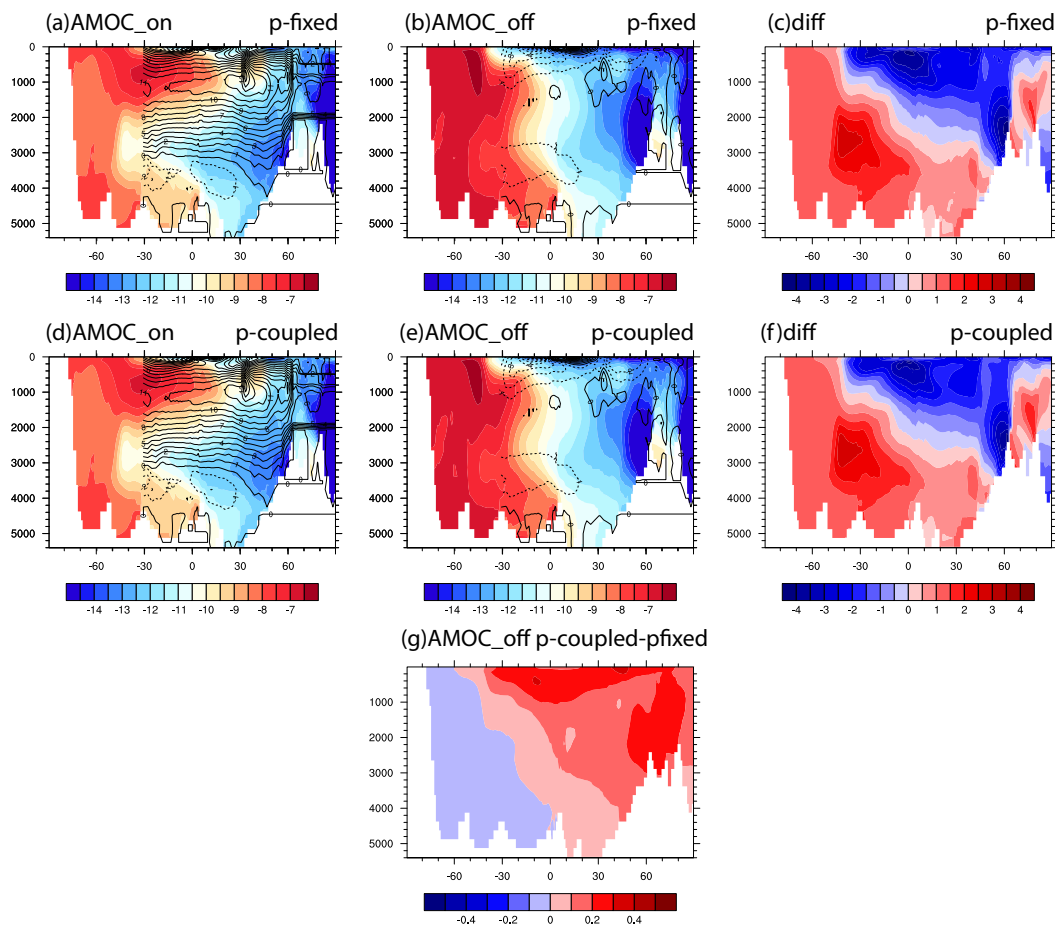


Figure 2.1.9 Atlantic zonal mean p-fixed ϵ_{Nd} (color) and Atlantic meridional overturning streamfunction (contour) in AMOC_on (a) and AMOC_off (b). The difference of Atlantic zonal mean p-fixed ϵ_{Nd} between AMOC_off and AMOC_on (c). (d), (e) and (f) are the same as (a), (b) and (c) for p-coupled ϵ_{Nd} . The difference between p-coupled and p-fixed ϵ_{Nd} during AMOC_off.

The prevalent interpretation of reconstructed ϵ_{Nd} in the Atlantic is based on the assumption that the ϵ_{Nd} end-member value does not change. In HOSING, the end-member value of AABW is calculated as the average ϵ_{Nd} from 60°S to 70°S below 4000m in the Southern Ocean. The AABW end-member ϵ_{Nd} value shifts from -8.6 in AMOC_on to -7.5 in AMOC_off (Figure 2.1.8b). ϵ_{Nd} of water from circum-Antarctic derives from the mixture of radiogenic Pacific waters and unradiogenic NADW (von Blanckenburg, 1999; Goldstein and Hemming, 2003). During AMOC_off, less NADW transported from the North Atlantic to the Southern Ocean, leads to a radiogenic shift in the AABW end-member value. The uniform 1 ϵ_{Nd} unit radiogenic change in the abyssal Atlantic (Figure 2.1.9c) is mainly due to the radiogenic change in AABW end-member value.

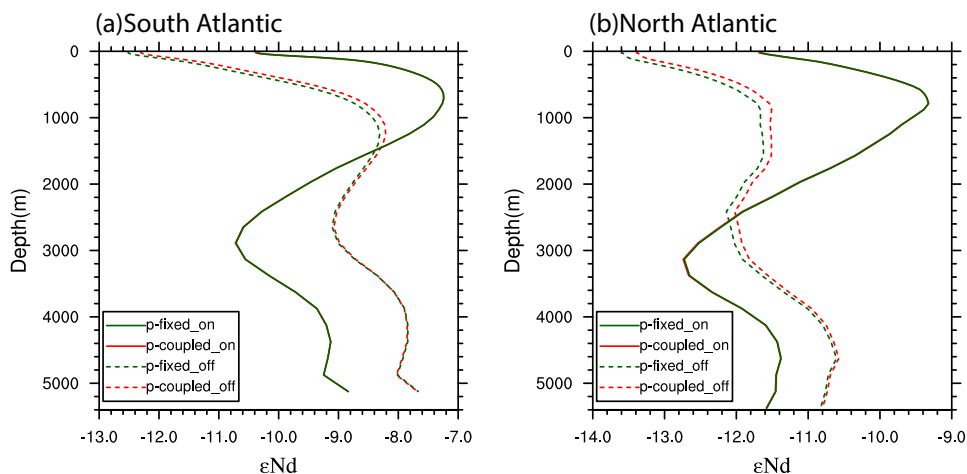


Figure 2.1.10 South Atlantic (a) and North Atlantic (b) mean ϵ_{Nd} profile during AMOC_on (solid line) and AMOC_off (dash line) for p-fixed (green) and p-coupled (red) ϵ_{Nd} .

NADW end-member shows an unradiogenic shift in HOSING. The NADW end-member value is calculated as average ϵ_{Nd} from 50°N to 60°N in the Atlantic between 2500m and 3000m (Figure 2.1.8c). The NADW end-member value shows a 2.8 ϵ_{Nd} unit unradiogenic shift from AMOC_on to AMOC_off. NADW ϵ_{Nd} in the eastern Atlantic (east of 20°W) and the western Atlantic (west of 50°W) are also calculated. NADW in the western North Atlantic is more unradiogenic and has a larger magnitude of change than in the eastern North Atlantic (Figure 2.1.9d and e) because water from the Labrador Sea, in the western North Atlantic, has the most unradiogenic ϵ_{Nd} . This unradiogenic shift of NADW is also shown in Figure 2.1.9c, indicating that this unradiogenic shift originates at depth. At 2500m, this unradiogenic shift starts at the west of Greenland at 60°N (Figure 2.1.11b) and expands to the whole North Atlantic from 50°N to 60°N and further to the eastern Atlantic south of 50°N (Figure 2.1.11c-f). South of 50°N, the ϵ_{Nd} experiences opposite changes between western and eastern Atlantic (Figure 2.1.11). In the western Atlantic, the radiogenic shift is because of less unradiogenic ϵ_{Nd} transported from the high latitude North Atlantic, due to the reduced western boundary current. In the eastern Atlantic, the unradiogenic shift is caused by the unradiogenic shift in the NADW endmember. Therefore, whether the NADW end-member change will affect the interpretation of ϵ_{Nd} in the Atlantic is location dependent. For example, during

AMOC_off, the north-south gradient of ϵ_{Nd} in the Atlantic becomes even larger than AMOC_on. The radiogenic ϵ_{Nd} shift from 2000m to 3000m in the South Atlantic (Figure 2.1.9c) cannot be attributed to the unradiogenic change in the NADW end-member value because of the opposite direction of that change. However, the unradiogenic change of ϵ_{Nd} in the western North Atlantic at 2500m (Figure 2.1.11f) can be explained, at least in part, by the NADW end-member change. Therefore, end-member ϵ_{Nd} values may be important when interpreting ϵ_{Nd} reconstructions depending on the location of sites.

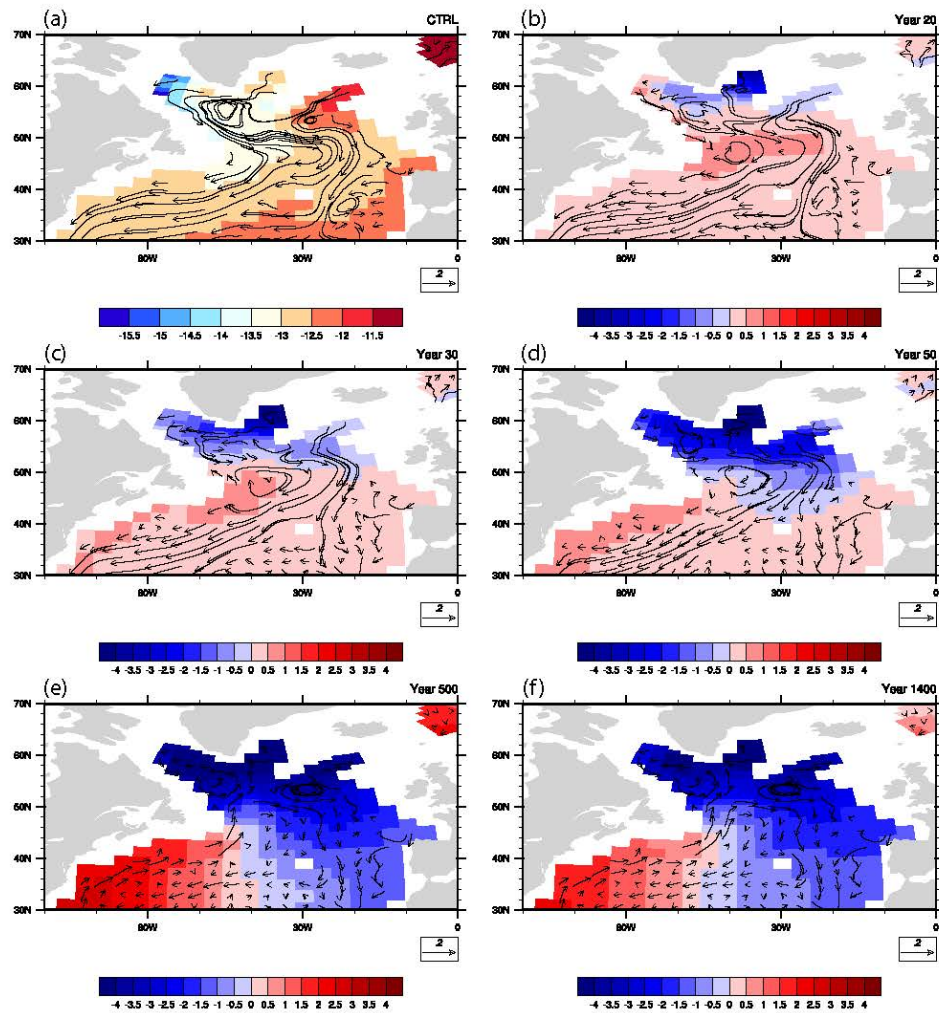


Figure 2.1.11 ϵ_{Nd} (p-fixed) at 2500m in CTRL (a) and the difference between different times in HOSING and CTRL (b-f). Velocity (cm/s) at different times is overlaid in each plot.

In HOSING, the productivity of CaCO_3 , opal, and POC in the North Atlantic is greatly reduced because of reduced nutrient supply resulting from the increase of

stratification (Schmittner, 2005). The resulting particle flux changes could also lead to a change in p-coupled ϵ_{Nd} (Rempfer et al., 2011). However, a comparison of p-coupled and p-fixed suggests that, ϵ_{Nd} changes in HOSING are mainly controlled by circulation. The changes in ϵ_{Nd} caused by productivity are much smaller than the ϵ_{Nd} changes caused by circulation (Figure 2.1.9c, f and g). The p-coupled ϵ_{Nd} shows almost identical changes to p-fixed ϵ_{Nd} (Figure 2.1.8, 2.1.9 and 2.1.10). The small difference between p-fixed and p-coupled ϵ_{Nd} in HOSING indicates that the effect of particle flux changes on the ϵ_{Nd} distribution is negligible compared with the effect of circulation change caused by fresh water forcing, consistent with the findings of Rempfer et al., (2012).

2.1.5 Conclusion and Discussion

Nd isotopes are implemented in POP2 mainly following the approach in Rempfer et al., (2011). The major difference from Rempfer et al., (2011) is Nd isotopes in the POP has both p-fixed and p-coupled versions. Nd concentration and ϵ_{Nd} in CTRL are in good agreement with observations under present day climate forcing: Nd concentration shows nutrient-like behavior, increasing with depth and along circulation pathway; ϵ_{Nd} in our model traces different water masses.

Furthermore, ϵ_{Nd} in the Atlantic in the idealized hosing experiment shows the effect of circulation changes on ϵ_{Nd} distribution. With a reduced AMOC strength, the simulated ϵ_{Nd} distribution shows a retreat of the northward propagating AAIW and southward propagating NADW. The AABW end-member value shows a radiogenic shift under reduced AMOC because of less unradiogenic input from the North Atlantic. The NADW end-member value shows a unradiogenic shift, which leads to the nonuniform ϵ_{Nd} changes between the eastern and western North Atlantic south of $50^{\circ}N$ at NADW depths. Therefore, the idealized hosing experiment suggests that whether the NADW end-member change influences the interpretation of ϵ_{Nd} at NADW depths in the North Atlantic is location dependent. Comparing with the hosing experiment in Bern3D model (Rempfer et al., 2012a), the largest changes in the equatorial Atlantic at intermediate depth and in the South Atlantic in the deep ocean are similar, but the response in the North Atlantic in

the deep ocean is different. From AMOC_{on} to AMOC_{off}, the unradiogenic shift in the high latitude North Atlantic (60°N) expands to the whole North Atlantic from the eastern Atlantic in our simulation. In Rempfer et al., (2012), high latitude North Atlantic also experiences an unradiogenic shift from AMOC_{on} to AMOC_{off}, but it is confined in the north of 50°N. The difference may be caused by the much lower model resolution in Rempfer et al., (2012).

Last but not least, in response to the fresh water forcing in the North Atlantic, particle fluxes change a lot, but the p-fixed and p-coupled ϵ_{Nd} shows very similar changes. That means that, in response to fresh water forcing, ϵ_{Nd} appears to be mainly influenced by circulation change and the effect of particle flux change on ϵ_{Nd} distribution can be neglected. This is also suggested by Rempfer et al., (2012), in which particle fluxes are scaled in deep water formation region and the effect of the changes in particle fluxes on ϵ_{Nd} is much smaller compared with the effect of the ocean circulation.

2.2 ^{231}Pa and ^{230}Th Development

^{231}Pa and ^{230}Th have been simulated in previous modeling studies (Dutay et al., 2009; Luo et al., 2010; Marchal et al., 2000; Rempfer et al., 2017; Siddall et al., 2005). Marchal et al., (2000) simulates ^{231}Pa and ^{230}Th in a zonally averaged circulation model, using the reversible scavenging model of Bacon and Anderson, (1982). One step further, Siddall et al. (2005) extends Marchal et al., (2000) by including particle dissolution with prescribed particle export production in a 3-D circulation model. Rempfer et al., (2017) further couples ^{231}Pa and ^{230}Th with active biogeochemical model and includes boundary scavenging and sediment resuspensions to improve model performance in simulating water column ^{231}Pa and ^{230}Th activity. Implementing ^{231}Pa and ^{230}Th in POP2 follows previous studies.

2.2.1 ^{231}Pa and ^{230}Th Implementation

The conservation equation for ^{231}Pa and ^{230}Th is shown in Eq 2.2.1, where $i = ^{231}\text{Pa}$ and ^{230}Th . Each term in Eq 2.2.1 is described as follows.

$$\frac{\partial A_t^i}{\partial t} = \beta^i - \lambda^i A_t^i - w_s \frac{\partial A_p^i}{\partial z} + Transport \quad (\text{Eq 2.2.1})$$

^{231}Pa and ^{230}Th are produced from the α decay of ^{235}U and ^{234}U uniformly everywhere at constant rate β^i ($\beta^{\text{Pa}} = 2.33 \cdot 10^{-3} \text{ dpm m}^{-3} \text{ yr}^{-1}$, $\beta^{\text{Th}} = 2.52 \cdot 10^{-2} \text{ dpm m}^{-3} \text{ yr}^{-1}$). ^{231}Pa and ^{230}Th are also subjective to radioactive decay with the decay constant of λ^i ($\lambda^{\text{Pa}} = 2.13 \cdot 10^{-5} \text{ yr}^{-1}$, $\lambda^{\text{Th}} = 9.22 \cdot 10^{-6} \text{ yr}^{-1}$). In addition to ocean transport, which includes advection, convection, and diffusion, another important process contributes to ^{231}Pa and ^{230}Th activity is the reversible scavenging (term $w_s \frac{\partial A_p^i}{\partial z}$ in Eq 2.12) by sinking particles with a sinking velocity w_s . w_s used in the implementation is 1000 m yr^{-1} (Arsouze et al., 2009; Dutay et al., 2009; Kriest, 2002). This reversible scavenging process can be referred to the similar process in Nd implementation, therefore omitted here. The scavenging coefficient used in reversible scavenging is the same as in Siddall et al., (2005), which follows Chase et al., (2002) (Table 2.2.1).

Similar to the Nd isotopes in Chapter 2.1, there are two versions of ^{231}Pa and ^{230}Th in POP2: one standard ^{231}Pa and ^{230}Th are coupled with active marine ecosystem model (“p-coupled”) and therefore is influenced by both ocean circulation change and particle flux change; another ^{231}Pa and ^{230}Th use prescribed particle fluxes (“p-fixed”) to help to understand the influence of the particle flux. By comparing the p-fixed $^{231}\text{Pa}/^{230}\text{Th}$ with the p-coupled $^{231}\text{Pa}/^{230}\text{Th}$, the effect of circulation change can be separated from particle flux change. P-fixed ^{231}Pa and ^{230}Th use particle fluxes prescribed as annual mean particle fluxes generated from the marine ecosystem module under present day climate forcing (Figure 2.1.1). In addition, the p-fixed ^{231}Pa and ^{230}Th can be run without the marine ecosystem module, reducing computational cost by a factor of 3 in the ocean-alone model simulation, making it a computationally efficient tracer for sensitivity studies. P-fixed and p-coupled ^{231}Pa and ^{230}Th can be turned on at the case build time and the p-coupled ^{231}Pa and ^{230}Th require the ecosystem module to be turned on at the same time.

Comparing with previous studies of modeling ^{231}Pa and ^{230}Th , our p-fixed version is the same as Siddall et al., (2002), except that different prescribed particle fluxes are

used. The p-coupled version allows coupling to biogeochemical module, which is similar to Rempfer et al., (2017), but we do not include boundary scavenging and sediment resuspensions as in Rempfer et al., (2017) because boundary scavenging and sediment resuspensions are suggested to be unimportant to influence the relationship between $^{231}\text{Pa}_p/^{230}\text{Th}_p$ and AMOC strength (Rempfer et al., 2017).

	^{231}Pa	^{230}Th
K_{CaCO_3}	$2.5*10^5$	$1.0*10^7$
K_{opal}	$1.67*10^6$	$5*10^5$
K_{POC}	$1.0*10^7$	$1.0*10^7$

Table 2.2.1. Partition coefficients for different particle types for ^{231}Pa and ^{230}Th , which follow Chase et al., (2002) and Siddall et al., (2005).

2.2.2 Model Validation

Under present day forcing by CORE-II data (Large and Yeager, 2008) (control experiment: CTRL), p-fixed and p-coupled version of ^{231}Pa and ^{230}Th show identical results (Figure 2.2.1, 2.2.2 and 2.2.3). P-fixed and p-coupled dissolved and particulate ^{231}Pa and ^{230}Th in CTRL are highly correlated with each other with correlations greater than 0.995 and regression coefficients are all near 1.0 ($R^2 > 0.995$). The correlation coefficient between p-fixed and p-coupled sediment $^{231}\text{Pa}/^{230}\text{Th}$ activity ratios in CTRL is 0.99 and the regression coefficient is 0.9 ($R^2 = 0.98$). This is expected because the particle fields used in p-fixed version are prescribed as the climatology of the particle fields used in the p-coupled version. Therefore, under the same climate forcing, p-fixed and p-coupled version of ^{231}Pa and ^{230}Th should be very similar. For the discussion of results in CTRL below, only the p-fixed version is discussed.

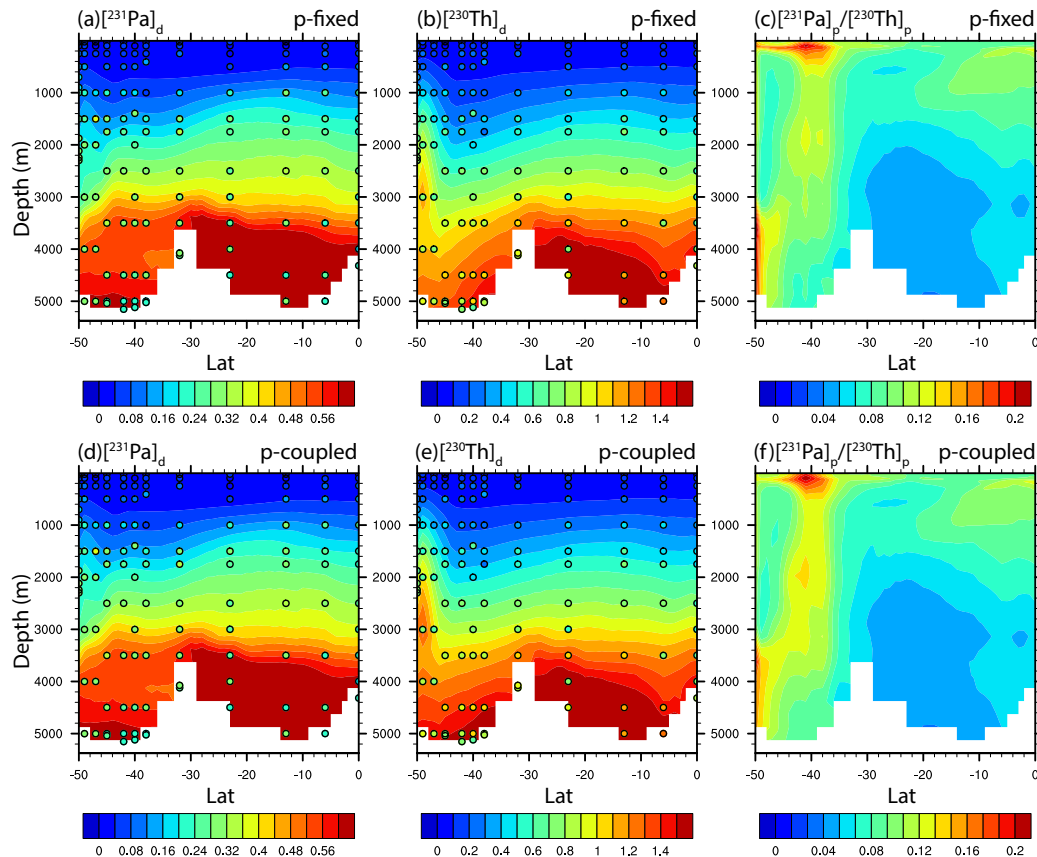


Figure 2.2.1 Dissolved ^{231}Pa , dissolved ^{230}Th and particulate $^{231}\text{Pa}/^{230}\text{Th}$ in CTRL along GEOTRACES transect GA02S (Deng et al., 2014) for both p-fixed (top row) and p-coupled (bottom row) ^{231}Pa and ^{230}Th (colored contour). Observations of dissolved ^{231}Pa and ^{230}Th activity are superimposed as colored circles using the same color scale.

The residence time of both ^{231}Pa and ^{230}Th in CTRL are comparable with observations. The residence time is calculated as the ratio of global average total isotope activity and the radioactive ingrowth of the isotope. Residence time in CTRL is 118 yr for ^{231}Pa and 33 yr for ^{230}Th , which are of the same magnitude as 111 yr for ^{231}Pa and 26 yr for ^{230}Th in observation (Yu et al., 1996).

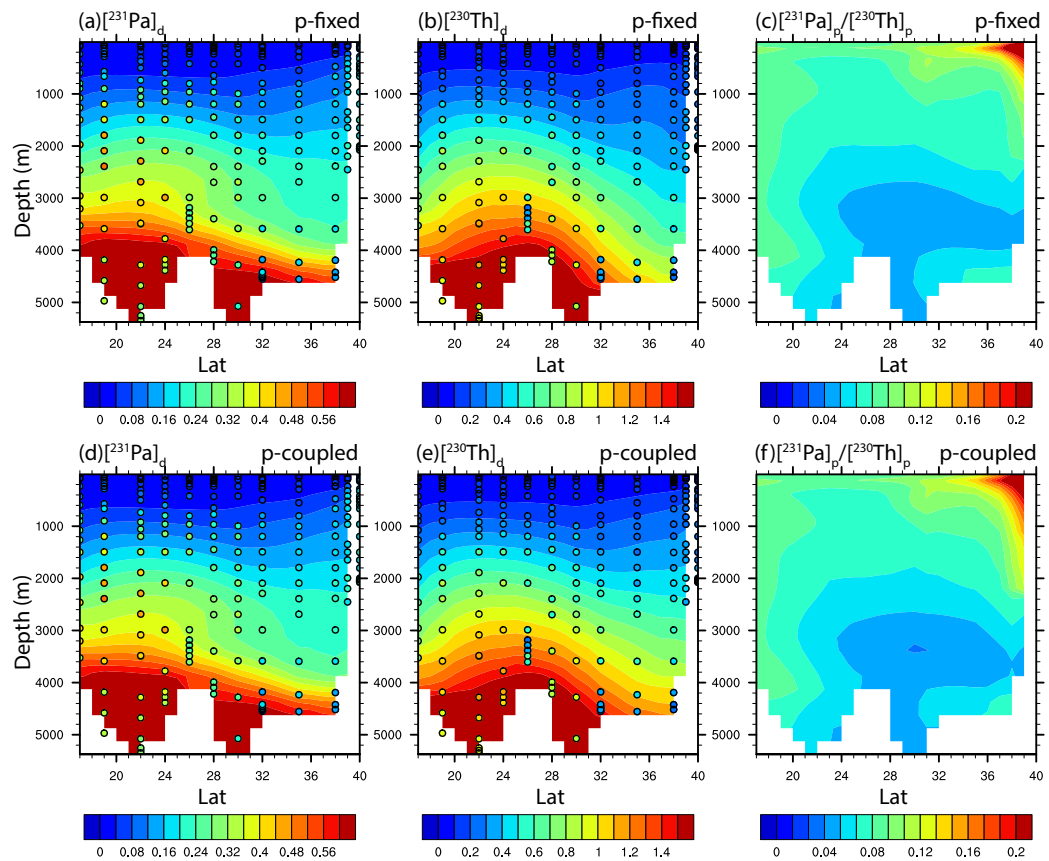


Figure 2.2.2 Dissolved ^{231}Pa , dissolved ^{230}Th and particulate $^{231}\text{Pa}/^{230}\text{Th}$ in CTRL along GEOTRACES transect GA03 (Hayes et al., 2015) for both p-fixed (top row) and p-coupled (bottom row) ^{231}Pa and ^{230}Th (colored contour). Observations of dissolved ^{231}Pa and ^{230}Th activity are superimposed as colored circles using the same color scale.

The general features of dissolved water column ^{231}Pa and ^{230}Th activities are simulated in CTRL. Dissolved ^{231}Pa and ^{230}Th activities increase with depth, as shown in two GEOTRACES transects (Deng et al., 2014; Hayes et al., 2015) in the Atlantic (Figure 2.2.1 and 2.2.2). The dissolved ^{231}Pa and ^{230}Th activities in CTRL are also at the same order of magnitude as in observations in the most of the ocean, except that simulated values are larger than observations in the abyssal, which is also the case in Siddall et al., (2005) and Rempfer et al., (2017) (their Fig. 2 and 3, experiment Re3d). Our model is unable to simulate the realistic dissolved ^{231}Pa and ^{230}Th activities in the abyssal probably

because boundary scavenging and sediment resuspensions are not included in our model. In Rempfer et al., 2017, without boundary scavenging and sediment resuspension, dissolved ^{231}Pa and ^{230}Th activities are quite large in the deep ocean. However, if boundary scavenging and sediment resuspension are included, the water column dissolved ^{231}Pa and ^{230}Th activity is in the right magnitude compared with observation. Therefore, if boundary scavenging and sediment resuspensions are added in POP2, dissolved ^{231}Pa and ^{230}Th activities in the abyssal should be greatly reduced.

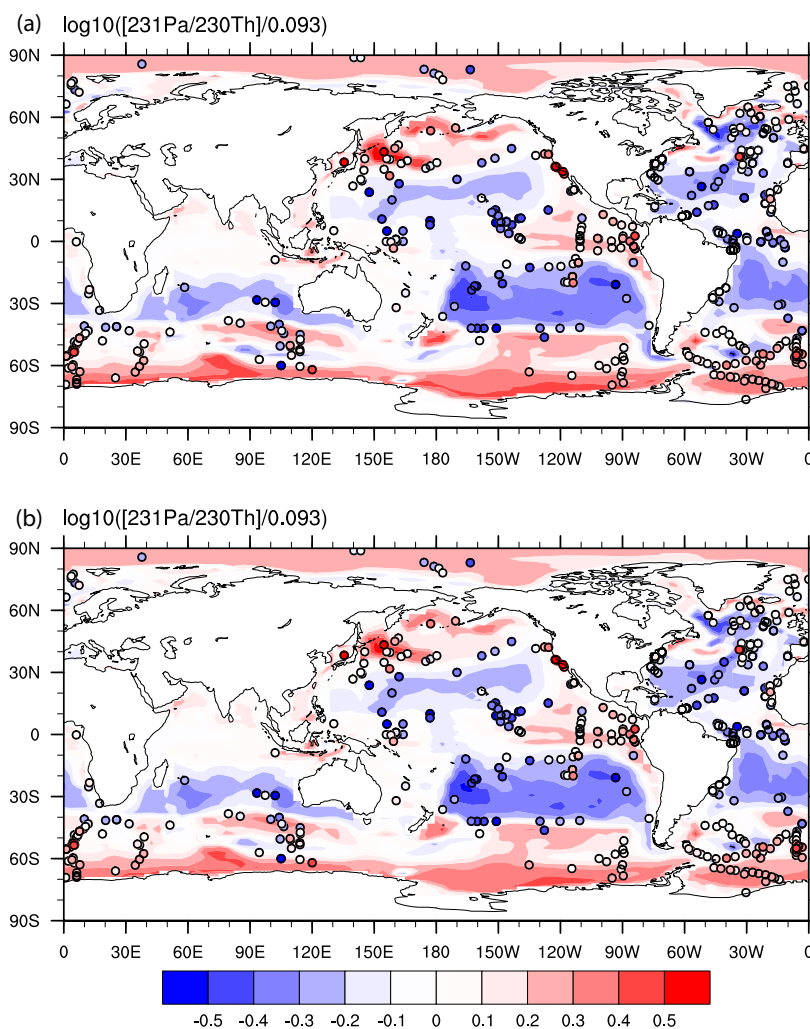


Figure 2.2.3 Sediment $^{231}\text{Pa}/^{230}\text{Th}$ activity ratio in CTRL for both p-fixed (a) and p-coupled version (b). Observations are attached as filled cycles using the same color map. The $^{231}\text{Pa}/^{230}\text{Th}$ activity ratio is plotted relative to the production ratio of 0.093 on a \log_{10} scale.

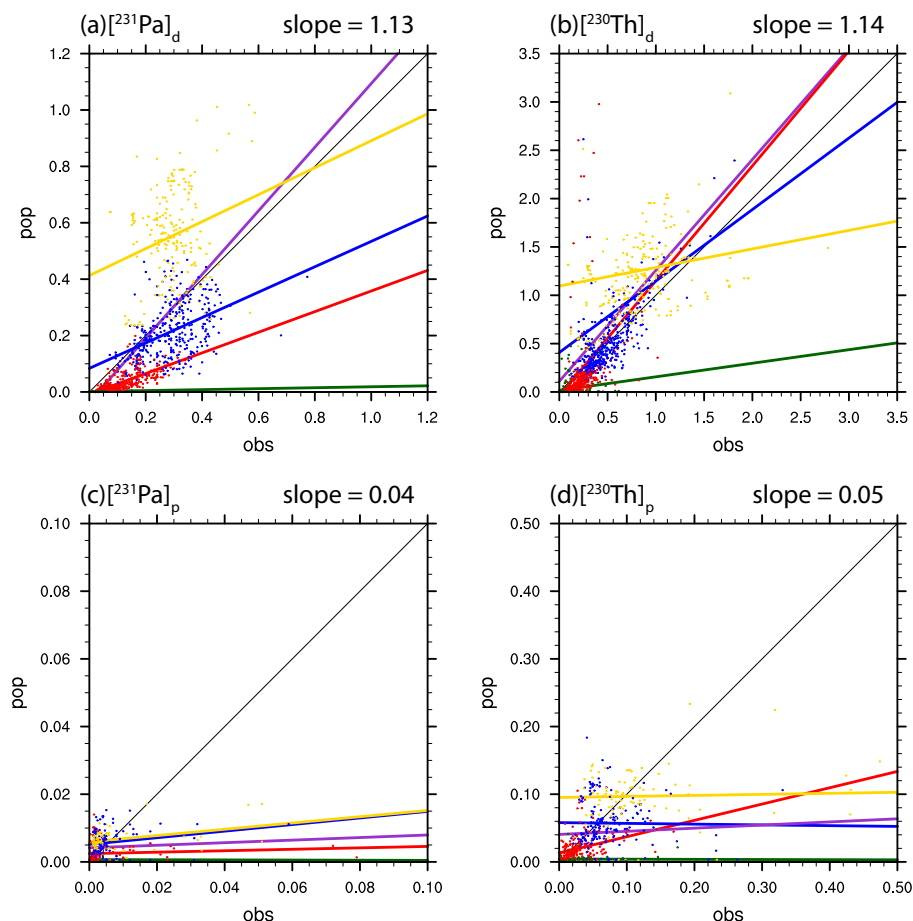


Figure 2.2.4 Scatter plot of global dissolved and particulate ^{231}Pa and ^{230}Th between observation and CTRL (p-fixed) (unit: dpm/m^3). (a) dissolved ^{231}Pa ; (b) particulate ^{231}Pa ; (c) dissolved ^{230}Th ; (d) particulate ^{230}Th . Observations in different depth range are indicated by different colors: green for 0-100m; red for 100m-1,000m; blue for 1,000m-3,000m and yellow for deeper than 3,000m. Purple line is the least squared linear regression line for all depth range, the slope of which is indicated at the top right of each plot. Green line is the least squared linear regression line for depth from 0-100m. Red line is the least squared linear regression line for depth from 100m - 1,000m. Blue line is the least squared linear regression line for depth from 1,000m-3,000m. Yellow line is the least squared linear regression line for depth deeper than 3,000m.

Dissolve and particulate ^{231}Pa and ^{230}Th are compared directly with observations from a compilation of observations listed in Table 2.2.2 (Figure 2.2.4). The linear regression coefficient between model results and observations is an indication of model ability to simulate ^{231}Pa and ^{230}Th activity (Dutay et al., 2009). The linear regression is near 1.0 for dissolved ^{231}Pa and ^{230}Th (1.02 for $^{231}\text{Pa}_d$ and 1.14 for $^{230}\text{Th}_d$), suggesting the good ability for the model to simulate the dissolved ^{231}Pa and ^{230}Th . However, the

simulation of the particulate activity is not as good as the dissolved activity. Particulate activity is overall larger than observation in the surface ocean and smaller than observation in the deep ocean for both particulate ^{231}Pa and ^{230}Th . The regression coefficient for particulate ^{231}Pa and ^{230}Th is 0.02 for $[\text{}^{231}\text{Pa}]_p$ and 0.05 for $[\text{}^{230}\text{Th}]_p$. The poor performance in simulating water column particulate ^{231}Pa and ^{230}Th activities is also in previous modeling studies (Dutay et al., 2009; Siddall et al., 2005), probably because of similar modeling scheme applied.

However, the simulated $^{231}\text{Pa}_p/^{230}\text{Th}_p$ is in reasonable agreement with observations. The $^{231}\text{Pa}_p/^{230}\text{Th}_p$ along two GEOTRACES transects (Figure 2.2.1 and 2.2.2) show the similar pattern and magnitude as in Rempfer et al., (2017), consistent with observations. Decrease of $^{231}\text{Pa}_p/^{230}\text{Th}_p$ with depth is well simulated, which is suggested to be caused by the lateral transport of ^{231}Pa from the North Atlantic to the Southern Ocean in deep ocean by AMOC (Gherardi et al., 2009; Lippold et al., 2011, 2012a; Luo et al., 2010; Rempfer et al., 2017).

The sediment $^{231}\text{Pa}/^{230}\text{Th}$ is also in good agreement with observations. Sediment $^{231}\text{Pa}/^{230}\text{Th}$ activity ratio in the North Atlantic is low because ^{231}Pa is more subject to the southward transport by active ocean circulation than ^{230}Th because of its longer residence time. The Southern Ocean maximum in the sediment $^{231}\text{Pa}/^{230}\text{Th}$ activity ratio is also simulated in CTRL. High opal fluxes in the Southern Ocean, which preferentially removes ^{231}Pa into sediment ($K_{opal}^{231Pa} > K_{opal}^{230Th}$) (Chase et al., 2002), leading to increased sediment $^{231}\text{Pa}/^{230}\text{Th}$ activity ratio. In addition, upwelling in the Southern Ocean brings up deep water enriched with ^{231}Pa , which is transported from the North Atlantic, to shallower depth and further contribute to the scavenging. CTRL can also produce higher sediment $^{231}\text{Pa}/^{230}\text{Th}$ activity ratio in regions with high particle production due to the “particle flux effect”. However, this particle flux effect is less effective in the North Atlantic than in the North Pacific and the Indian Ocean due to active deep ocean circulation transporting ^{231}Pa southward in the Atlantic (Yu et al., 1996). Quantitatively, the regression coefficient between sediment $^{231}\text{Pa}/^{230}\text{Th}$ in CTRL and observation in the Atlantic is 0.86, which is larger than in other basins. This suggests that sediment

$^{231}\text{Pa}/^{230}\text{Th}$ is better simulated in the Atlantic than in other basins. One possible explanation is that sediment $^{231}\text{Pa}/^{230}\text{Th}$ in the Atlantic is controlled by both ocean circulation and particle flux, while in other basins sediment $^{231}\text{Pa}/^{230}\text{Th}$ is controlled almost only by particle flux. With active AMOC, the north south gradient of sediment $^{231}\text{Pa}/^{230}\text{Th}$ can be simulated. However, for example, in the Southern Ocean, sediment $^{231}\text{Pa}/^{230}\text{Th}$ is dominantly controlled by opal flux, which varies on small scales and is difficult for simulation. Therefore, model performance in simulating sediment $^{231}\text{Pa}/^{230}\text{Th}$ in the Southern Ocean is not as good as in the Atlantic.

WATER COLUMN ACTIVITY	Holocene core-top $^{231}\text{Pa}/^{230}\text{Th}$
(Guo et al., 1995)	(Yu, 1994)
(Cochran et al., 1987)	(DeMaster, 1979)
(Nozaki et al., 1987)	(Bacon and Rosholt, 1982)
(Bacon and Anderson, 1982)	(Mangini and Diester-Hass, 1983)
(Bacon et al., 1989)	(Kumar, 1994)
(Huh and Beasley, 1987)	(Yang et al., 1986)
(Rutgers van der Loeff and Berger, 1993)	(Anderson et al., 1983)
(Nozaki et al., 1981)	(Anderson et al., 1994)
(Nozaki and Nakanishi, 1985)	(Ku, 1966)
(Mangini and Key, 1983)	(Ku et al., 1972)
(Nozaki and Horibe, 1983)	(Frank et al., 1994)
(Moore, 1981)	(Shimmield et al., 1986)
(Nozaki and Yamada, 1987)	(Frank, 1996)
(Roy-Barman et al., 1996)	(Yong Lao et al., 1992)
(Nozaki and Yang, 1987)	(Francois et al., 1993)
(Moran et al., 1995)	(Anderson et al., 1990)
(Luo et al., 1995)	(Mangini and Sonntag, 1977)
(Colley et al., 1995)	(Schmitz et al., 1986)
(Scholten et al., 1995)	(Shimmield and Price, 1988)
(Cochran et al., 1995)	(Yong-Liang Yang et al., 1995)
(Vogler et al., 1998)	(Müller and Mangini, 1980)
(Moran et al., 1997)	(Mangini and U., 1987)
(Edmonds et al., 1998)	(Scholten et al., 1995)
(Moran et al., 2001)	(Walter et al., 1997)
(Edmonds et al., 2004)	(Lippold et al., 2011)
(Okubo et al., 2007b)	(Lippold et al., 2012b)
(Coppola et al., 2006)	(Bradt Miller et al., 2007)

(Moran et al., 2002)	(Gherardi et al., 2005)
(Okubo et al., 2004)	(Gutjahr et al., 2008)
(Okubo et al., 2007a)	(Hall et al., 2006)
(Okubo et al., 2012)	(Lippold et al., 2011)
(Robinson et al., 2004)	(Roberts et al., 2014)
(Thomas et al., 2006)	(Bradtmitter et al., 2014)
(Trimble et al., 2004)	(Burckel et al., 2016)
(Venchiarutti et al., 2011)	(Hoffmann et al., 2013)
(Hsieh et al., 2011)	(Jonkers et al., 2015)
(Scholten et al., 2008)	(Negre et al., 2010)
(Luo et al., 2010)	
(Deng et al., 2014)	
(Hayes et al., 2013)	
(Hayes et al., 2015)	

Table 2.2.2. References for observations of water column ^{231}Pa and ^{230}Th activity (left column) and Holocene core-top $^{231}\text{Pa}/^{230}\text{Th}$ (right column).

2.2.3 ^{231}Pa and ^{230}Th in Idealized Hosing Experiment

Potential changes in the export of biogenic particles make using $^{231}\text{Pa}/^{230}\text{Th}$ ratio to reconstruct AMOC strength under debate. In response to fresh water perturbation in the North Atlantic, both biological productivity and AMOC strength will change and will influence sediment $^{231}\text{Pa}/^{230}\text{Th}$ in different ways. To test how sediment $^{231}\text{Pa}/^{230}\text{Th}$ ratio responds to the change of AMOC in POP2 and how the particle fluxes change influence sediment $^{231}\text{Pa}/^{230}\text{Th}$ ratio, both the p-fixed and $^{231}\text{Pa}/^{230}\text{Th}$ evolution in HOSING are examined (the same experiment described in Chapter 2.1).

In HOSING, after applying freshwater forcing to the North Atlantic, AMOC strength quickly decreases to a minimum of 2 Sv (AMOC_off) (Figure 2.2.6a). During the AMOC_off state, compared with CTRL with active AMOC (AMOC_on), p-fixed sediment $^{231}\text{Pa}/^{230}\text{Th}$ shows an overall increase in the North Atlantic and a decrease in the South Atlantic (Figure 2.2.7b) because of the reduced southward transport of ^{231}Pa from the North Atlantic by AMOC, consistent with paleo proxy evidence there (e.g. Gherardi et al., 2005, 2009; McManus et al., 2004). The overall increase of sediment $^{231}\text{Pa}/^{230}\text{Th}$

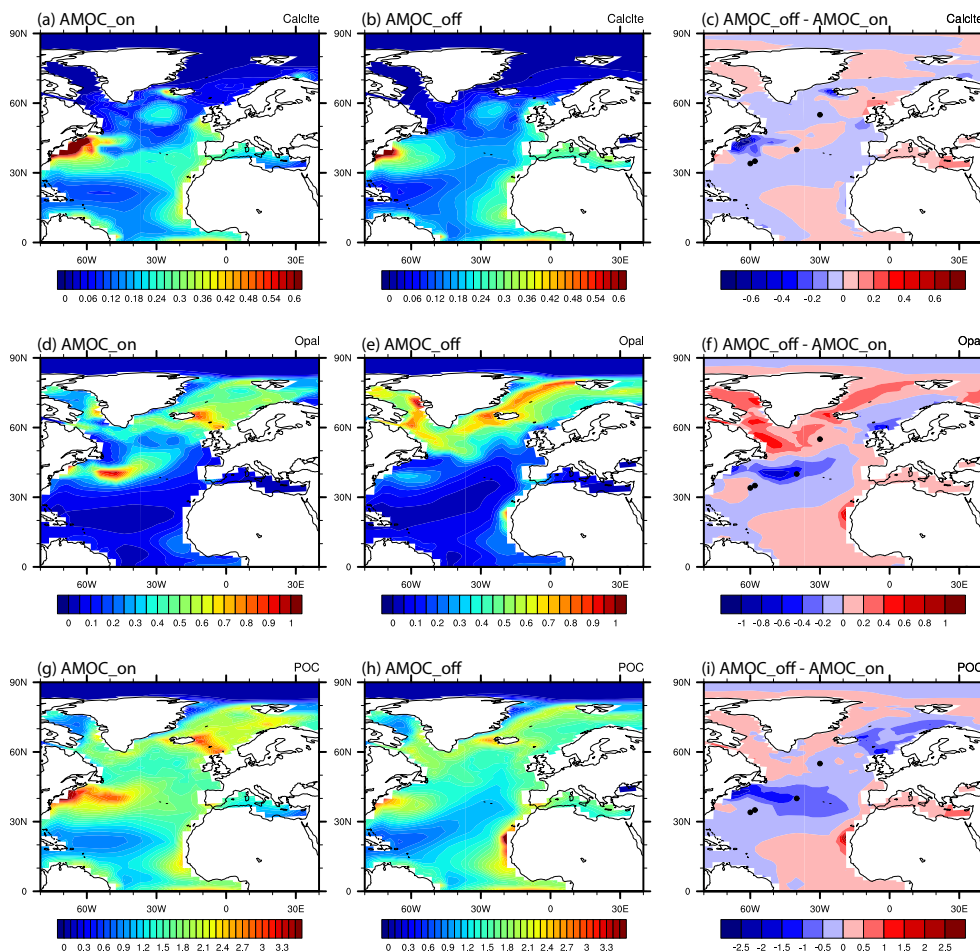


Figure 2.2.5 Comparison of particle fluxes between AMOC_on and AMOC_off. CaCO_3 flux at 105m ($\text{mol m}^{-2} \text{yr}^{-1}$) during AMOC_on (a), AMOC_off (b) and difference between AMOC_off and AMOC_on (c). (b) Opal flux at 105m ($\text{mol m}^{-2} \text{yr}^{-1}$) during AMOC_on (d), AMOC_off (e) and difference between AMOC_off and AMOC_on (f). POC flux at 105m ($\text{mol m}^{-2} \text{yr}^{-1}$) during AMOC_on (g), AMOC_off (h) and difference between AMOC_off and AMOC_on (i).

ratio in the North Atlantic in response to the AMOC collapse can be seen more clearly in the time evolution of the sediment $^{231}\text{Pa}/^{230}\text{Th}$ ratio averaged from 20°N to 60°N in the North Atlantic (Figure 2.2.7b, green). Quantitatively, the $^{231}\text{Pa}/^{230}\text{Th}$ increases from 0.074 in AMOC_on to 0.098 in AMOC_off in the p-fixed version, approaching the production ratio of 0.093. This increase of $^{231}\text{Pa}/^{230}\text{Th}$ is also in the subtropical North Atlantic from the two sites near Bermuda Rise (Figure 2.2.7e and f), which is of comparable magnitude with the change from the LGM to theHS1 in reconstructions there (McManus et al., 2004).

In addition, the pattern of p-fixed (Figure 2.2.8a) sediment $^{231}\text{Pa}/^{230}\text{Th}$ ratio during the Atlantic in AMOC_off state is similar to the opal distribution (Figure 2.1.1b) because, without active circulation, sediment $^{231}\text{Pa}/^{230}\text{Th}$ ratio is more controlled by particle flux effect, which is similar to the Pacific in CTRL. The p-fixed sediment $^{231}\text{Pa}/^{230}\text{Th}$ ratio in HOSING behaves similarly to that in Siddall et al., (2007).

The overall increase in p-fixed sediment $^{231}\text{Pa}/^{230}\text{Th}$ ratio in the North Atlantic is not homogenous and the magnitude of the change between AMOC_on and AMOC_off varies with location, depending on the distribution of particle flux, especially the opal flux (Figure 2.2.6 and 2.2.7). The maximum increase in p-fixed sediment $^{231}\text{Pa}/^{230}\text{Th}$ ratio occurs near 40°N western Atlantic (Figure 2.2.7a), where the opal production in POP2 is maximum in the North Atlantic (Fig. 2.1.1b). The sediment $^{231}\text{Pa}/^{230}\text{Th}$ ratio in this region during AMOC_on is larger than production ratio of 0.093 because opal maximum provides extra ^{231}Pa to this region (“particle flux effect”), which overwhelms the active ocean circulation transporting ^{231}Pa southward outside this region (Figure 2.2.6d, green). During AMOC_off, without active ocean circulation, the particle flux effect becomes even stronger because less ^{231}Pa is transported out of the North Atlantic and p-fixed sediment $^{231}\text{Pa}/^{230}\text{Th}$ ratio becomes even larger. It should be noted that the opal maximum in this region is not in the observation (Fig. 7.2.5 in Sarmiento and Gruber 2006). However, the sediment $^{231}\text{Pa}/^{230}\text{Th}$ response in HOSING is self-consistent with the particle flux in the model since the location of maximum $^{231}\text{Pa}/^{230}\text{Th}$ increase matches the location of opal flux in the model.

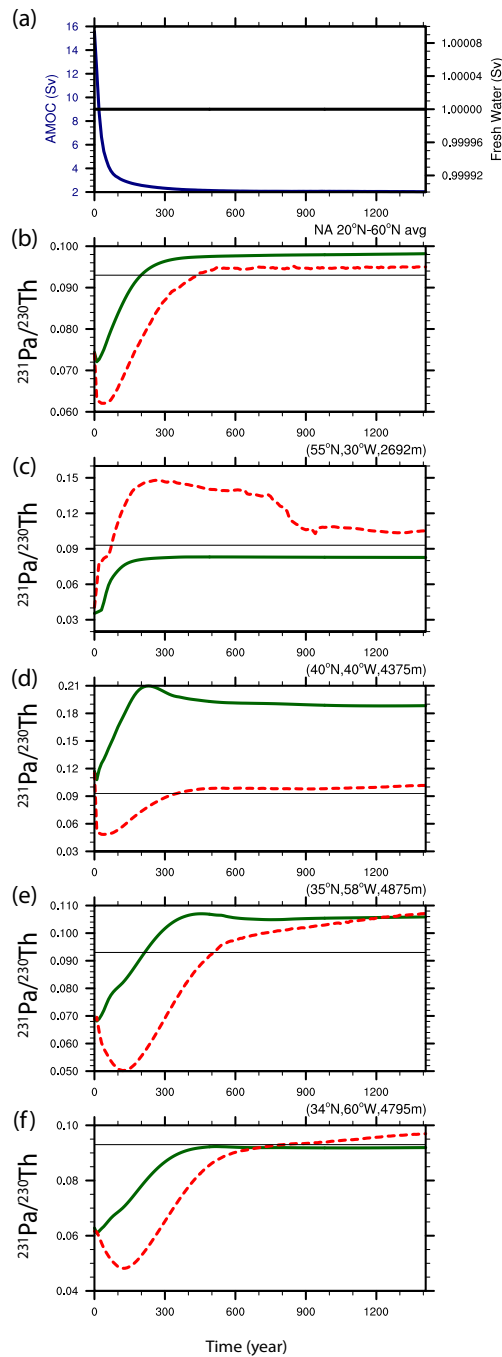


Figure 2.2.6 Time evolutions in HOSING. (a) Freshwater forcing (black) and AMOC strength (navy), which is defined as the maximum of the overturning streamfunction below 500m in the North Atlantic. (b) North Atlantic average sediment $^{231}\text{Pa}/^{230}\text{Th}$ activity ratio from 20°N to 60°N: p-fixed (green) and p-coupled (red). Production ratio of 0.093 is indicated by a solid black line (similar in c, d, e and f). (c) Sediment $^{231}\text{Pa}/^{230}\text{Th}$ activity ratio at (55°N, 30°W). (d) Sediment $^{231}\text{Pa}/^{230}\text{Th}$ activity ratio at (40°N, 40°W). (e) Sediment $^{231}\text{Pa}/^{230}\text{Th}$ activity ratio at (35°N, 58°W). (f) Sediment $^{231}\text{Pa}/^{230}\text{Th}$ activity ratio at (34°N, 60°W). (e) and (f) are near Bermuda Rise. Locations of each site are shown as dots in Figure 2.2.5b.

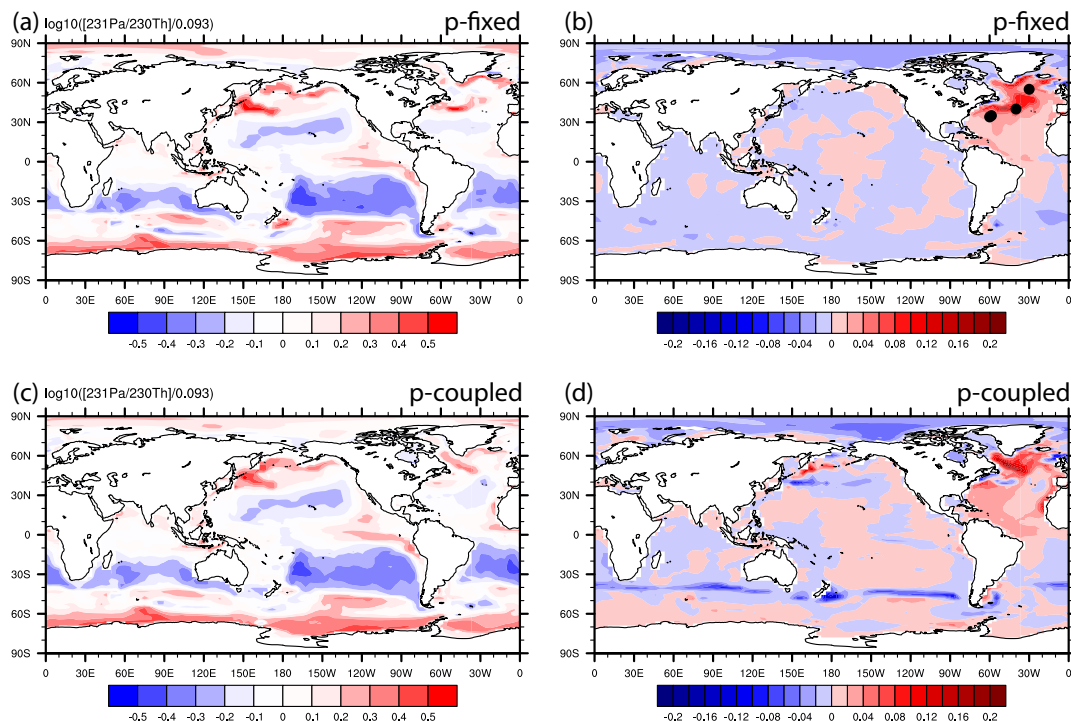


Figure 2.2.7 Sediment $^{231}\text{Pa}/^{230}\text{Th}$ activity ratio during AMOC off state and the difference between AMOC off and CTRL. (a) P-fixed $\log_{10}([^{231}\text{Pa}/^{230}\text{Th}]/0.093)$ in AMOC_off. (b) Difference of p-fixed sediment $^{231}\text{Pa}/^{230}\text{Th}$ activity ratio between AMOC_off and AMOC_on. (c) and (d) are similar to (a) and (b) for p-coupled sediment $^{231}\text{Pa}/^{230}\text{Th}$ activity ratio.

In most regions of the Atlantic, p-coupled sediment $^{231}\text{Pa}/^{230}\text{Th}$ shows a similar response to p-fixed $^{231}\text{Pa}/^{230}\text{Th}$ in HOSING. The evolution of p-fixed and p-coupled sediment $^{231}\text{Pa}/^{230}\text{Th}$ activity ratio in HOSING are highly correlated (Figure 2.2.8a). The change of sediment $^{231}\text{Pa}/^{230}\text{Th}$ ratio from AMOC_on to AMOC_off are similar in both the p-fixed and p-coupled version (Figure 2.2.8b). The correlation between p-fixed and p-coupled sediment $^{231}\text{Pa}/^{230}\text{Th}$ ratio change from AMOC_on to AMOC_off is 0.72 (1455points) and the linear regression coefficient is 0.71 ($R^2 = 0.52$). A high correlation between p-fixed and p-coupled response mainly happens over low productivity regions (Figure 2.1.1, 2.2.7 and 2.2.8), where circulation effect on sediment $^{231}\text{Pa}/^{230}\text{Th}$ is more important than the particle flux change in HOSING.

However, the responses of p-fixed and p-coupled sediment $^{231}\text{Pa}/^{230}\text{Th}$ to the fresh water forcing can differ significantly in high productivity regions because of the

productivity change. With persistent freshwater forcing over the North Atlantic, most regions in the North Atlantic show reduced production of CaCO_3 , opal and POC (Figure 2.2.5). In our model, the productivity in the mid-latitude North Atlantic is indeed greatly reduced after the freshwater forcing is applied, as suggested by Schmittner, (2005). For example, opal production from 30°N - 50°N in the Atlantic at the end of HOSING is reduced by 50%~90% of its original value in CTRL. However, opal production increases in high latitude North Atlantic (north of 50°N). The pattern of opal production changes with high opal production region shifts northward in HOSING. These particle flux changes will influence sediment $^{231}\text{Pa}/^{230}\text{Th}$ as discussed below.

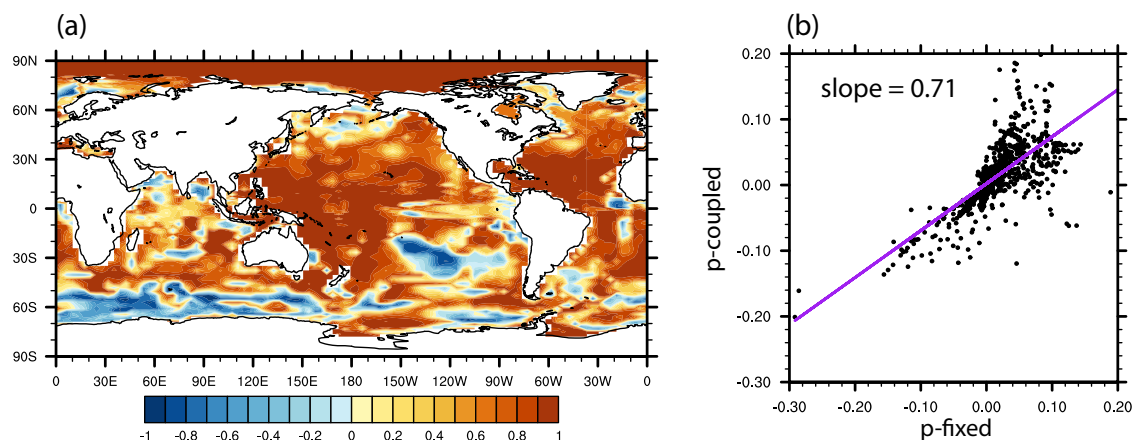


Figure 2.2.8 (a) Correlation of p-fixed and p-coupled evolution of sediment $^{231}\text{Pa}/^{230}\text{Th}$ activity ratio in HOSING. (b) Scatter plot of p-fixed and p-coupled sediment $^{231}\text{Pa}/^{230}\text{Th}$ activity ratio change from AMOC_on to AMOC_off in the Atlantic and the Southern Ocean (70°W - 20°E). Purple line is the least squared linear regression line and slope is the linear regression coefficient.

North of 50°N in the Atlantic, opal productivity increases during AMOC_off (Figure 2.2.5f) will result in an increase in sediment $^{231}\text{Pa}/^{230}\text{Th}$. The increase caused by greater opal productivity enhances the sediment $^{231}\text{Pa}/^{230}\text{Th}$ increase caused by reduced AMOC. Therefore, the increase in p-coupled sediment $^{231}\text{Pa}/^{230}\text{Th}$ from AMOC_on to AMOC_off is larger than p-fixed sediment $^{231}\text{Pa}/^{230}\text{Th}$ change (Figure 2.2.6c).

In the mid-latitude North Atlantic, opal productivity decreases during AMOC_off (Figure 2.2.5f) and will lead to a decrease in sediment $^{231}\text{Pa}/^{230}\text{Th}$, which is opposite to

the effect of reduced AMOC. P-coupled sediment $^{231}\text{Pa}/^{230}\text{Th}$ shows an initial decrease in first 200 years (Figure 2.2.6 d, e, and f, red dash lines) caused by the reduced opal productivity. But this decreasing trend is reversed eventually, suggesting that the influence of particle flux change is overwhelmed by the effect of reduced AMOC. In the long run, most regions in the subtropical and mid-latitude Atlantic show increased sediment $^{231}\text{Pa}/^{230}\text{Th}$ in HOSING (Figure 2.2.7d), indicating the dominant effect of reduced AMOC. However, sediment $^{231}\text{Pa}/^{230}\text{Th}$ at 40°N west Atlantic, where opal productivity is maximum during AMOC_on, show a decrease from AMOC_on to AMOC_off (Figure 2.2.6 d and Figure 2.2.7 d). During AMOC_on, the opal productivity maximum at 40°N west Atlantic lead to regional maximum sediment $^{231}\text{Pa}/^{230}\text{Th}$ because of the particle flux effect (Figure 2.2.3). During AMOC_off, this opal productivity maximum is eliminated (Figure 2.2.5e) and there is no more extra ^{231}Pa supplied by surroundings to this region, which leads to a decrease in sediment $^{231}\text{Pa}/^{230}\text{Th}$. This decrease in sediment $^{231}\text{Pa}/^{230}\text{Th}$ caused by productivity change is greater than the increase caused by the reduced AMOC. Therefore, sediment $^{231}\text{Pa}/^{230}\text{Th}$ experiences a decrease from AMOC_on to AMOC_off at this location. At the same location, ϵ_{Nd} changes for both p-fixed and p-coupled version show (Figure 2.1.8f) comparable magnitude, suggesting that ϵ_{Nd} is much less sensitive to the particle fluxes change comparing to $^{231}\text{Pa}/^{230}\text{Th}$. The results in HOSING suggest that although the circulation effect is more dominant than the particle flux change in controlling sediment $^{231}\text{Pa}/^{230}\text{Th}$ on long time scale over most of North Atlantic (Figure 2.2.8), particle flux change can be important on short time scale and in high productivity regions. With p-fixed and p-coupled ^{231}Pa and ^{230}Th , this model can help to detangle the circulation effect and particle flux effect.

It has been suggested that the particulate $^{231}\text{Pa}/^{230}\text{Th}$ response to the change of AMOC depends on the location and depth. Above 2km and high latitude North Atlantic, particulate $^{231}\text{Pa}/^{230}\text{Th}$ decreases with the increased AMOC (Rempfer et al., 2017). Results in HOSING supports this finding (Figure 2.2.9 a and b). Both p-fixed and p-coupled particulate $^{231}\text{Pa}/^{230}\text{Th}$ show similar patterns of change from AMOC_on to AMOC_off: decrease in particulate $^{231}\text{Pa}/^{230}\text{Th}$ at shallow depth and north of 60°N and

increase in particulate $^{231}\text{Pa}/^{230}\text{Th}$ below 2km and south of 60°N during AMOC_off. Therefore, sediment depth should also be taken into consideration when interpreting sediment $^{231}\text{Pa}/^{230}\text{Th}$. Since the pattern in p-coupled is similar to the pattern in p-fixed, the opposite particulate $^{231}\text{Pa}/^{230}\text{Th}$ changes in shallow and deep North Atlantic is associated with AMOC change. During AMOC_on, upper limb of AMOC (about upper 1km) transport water northward, which provides extra ^{231}Pa to North Atlantic and particulate $^{231}\text{Pa}/^{230}\text{Th}$ is larger than the production ratio of 0.093. In contrast, the lower limb of AMOC (2km-3km) features southward transport, which transports ^{231}Pa to the Southern Ocean and particulate $^{231}\text{Pa}/^{230}\text{Th}$ is smaller than the production ratio of 0.093 (Figure 2.2.9c solid). During AMOC_off, ocean transport of ^{231}Pa is greatly reduced. Therefore, shallow (deep) depth experiences a decrease (increase) in particulate $^{231}\text{Pa}/^{230}\text{Th}$ and the vertical gradient in the particulate $^{231}\text{Pa}/^{230}\text{Th}$ is also greatly reduced (Figure 2.2.9 c dash). The results in HOSING supports that the depth dependence of particulate $^{231}\text{Pa}/^{230}\text{Th}$ is mainly caused by lateral transport of ^{231}Pa by circulation (Gherardi et al., 2009; Lippold et al., 2011, 2012a; Luo et al., 2010; Rempfer et al., 2017).

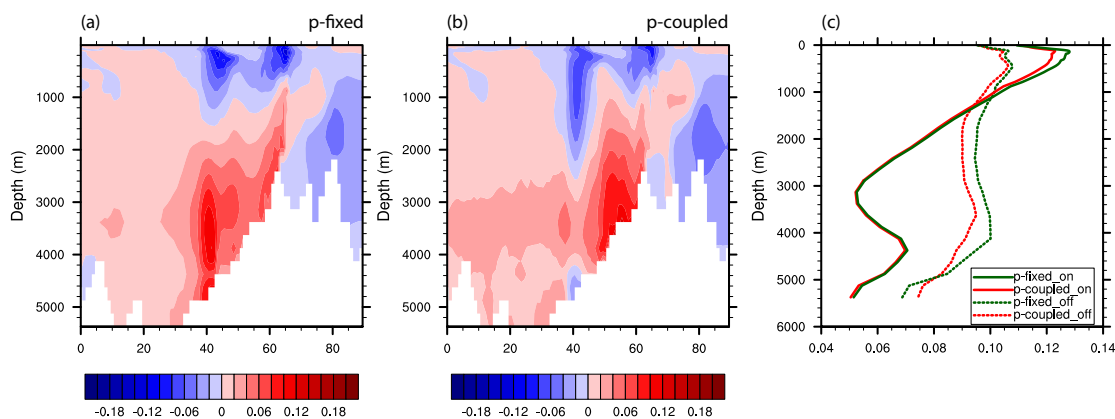


Figure 2.2.9 Difference of Atlantic zonal mean particulate $^{231}\text{Pa}/^{230}\text{Th}$ between AMOC_off and AMOC_on: (a) p-fixed and (b) p-coupled. (c) North Atlantic (20°N-60°N) average profile during AMOC_on (solid) and AMOC_off (dash) for p-fixed (green) and p-coupled (red) particulate $^{231}\text{Pa}/^{230}\text{Th}$.

2.2.4 Conclusion and Discussion

^{231}Pa and ^{230}Th are implemented in the ocean model of the CESM in both the p-coupled and p-fixed forms. Under present day forcing, water column ^{231}Pa and ^{230}Th activity and sediment $^{231}\text{Pa}/^{230}\text{Th}$ activity ratio in the model are consistent with observations. Furthermore, the correct magnitude of the sediment $^{231}\text{Pa}/^{230}\text{Th}$ ratio response to the freshwater forcing is simulated. It is suggested that the change of circulation is the dominant factor that influences sediment $^{231}\text{Pa}/^{230}\text{Th}$ on long time scale over most of the globe in the idealized hosing experiment, although the detailed difference between p-fixed and p-coupled sediment $^{231}\text{Pa}/^{230}\text{Th}$ ratio response to freshwater forcing in different locations can be complicated.

However, much remains to be improved in the ^{231}Pa and ^{230}Th module in the future. For example, the model can be further improved by including nepheloid layers to better simulate water column ^{231}Pa and ^{230}Th activity as in Rempfer et al. (2017). In addition, partition coefficient for different particles can be further tuned, which can improve our understanding of the affinity of ^{231}Pa and ^{230}Th to different particles, complementing the limited observational studies available (e.g. Chase et al., (2002); Scholten et al., (2005); Walter et al., (1997)).

3. Deglacial Northward Penetration of AAIW in the Atlantic

In this chapter, the deglacial AAIW in the Atlantic is first examined in the transient simulation using iPOP2 since proxy records and modeling studies (Chapter 1.3) suggest different AAIW response to the change of AMOC. Furthermore, why ϵ_{Nd} evolutions from three nearby tropical Atlantic sites show opposite trends from LGM to HS1 is investigated. It is argued that site MD99-2198 in Pahnke et al., 2008 lies beneath the modern AAIW depth range and fails to record the AAIW northward penetration signals (Xie et al., 2012). However, present day hydrographic data from the Gulf of Mexico show much warmer and saltier water mass than AAIW, suggesting that if any AAIW has arrived at this site, it has already been modified by other water masses. Therefore, site KNR166-2-26JPC in Xie et al., 2012 from the Gulf of Mexico did not record the deglacial AAIW changes (Osborne et al., 2014; Pena et al., 2013). Currently, it still remains uncertain how to resolve the discrepancies in ϵ_{Nd} reconstructions and how AAIW northward penetration in the Atlantic changed during the last deglaciation.

3.1 Transient Deglacial Simulation and Nd Module Setup

A transient simulation simulating the deglacial ocean changes is carried out using iPOP2 (iPOP2_TRACE) (Zhang et al., 2017). iPOP2 is forced by the monthly output from coupled transient experiment TraCE21K using the Community Climate System Model version 3 (CCSM3) under realistic climate forcing (He, 2011; Liu et al., 2009), which captures many features of the climate change during the last deglaciation. The surface wind stress is directly from TraCE21K, while surface heat and freshwater are applied using hybrid boundary condition, which is a combination of flux forcing and surface restoring. iPOP2_TRACE is able to simulate deglacial ocean evolution (Zhang et al., 2017).

However, when iPOP2_TRACE was run, Nd module was in an earlier version than the Nd module discussed in Chapter 2.1. The parameters used in the Nd module in iPOP2_TRACE follows Rempfer et al., (2011). But this will not affect the results in this chapter since the ϵ_{Nd} distribution under present day forcing in this earlier version can still

capture the major features, consistent with observations. The vertical structure of ϵ_{Nd} , indicating the influences of water mass from different origins is well simulated (Figure 3.1.1). For example, the zig-zag pattern in observations (Goldstein and Hemming, 2003) are successfully simulated in the model (Figure 3.1.1 profile 9 and 10), as AAIW and AABW carry radiogenic ϵ_{Nd} northward and NADW carries unradiogenic ϵ_{Nd} southward. In particular, the model successfully captures the relative magnitude among different water masses, suggesting it can be used to study the relative changes of different water masses during the deglaciation. Another important feature is that the model is able to simulate the very radiogenic water from the Caribbean Sea (Figure 3.1.1 profile 7) (Osborne et al., 2014). This turns out to be an important water mass that is the source of some of the discrepancies in the ϵ_{Nd} reconstructions, as will be discussed later. This Nd module can simulate the major ϵ_{Nd} features of the main water masses over both global scale and local scale of the tropical Atlantic and therefore should help to interpret ϵ_{Nd} reconstructions in the tropical Atlantic in the past.

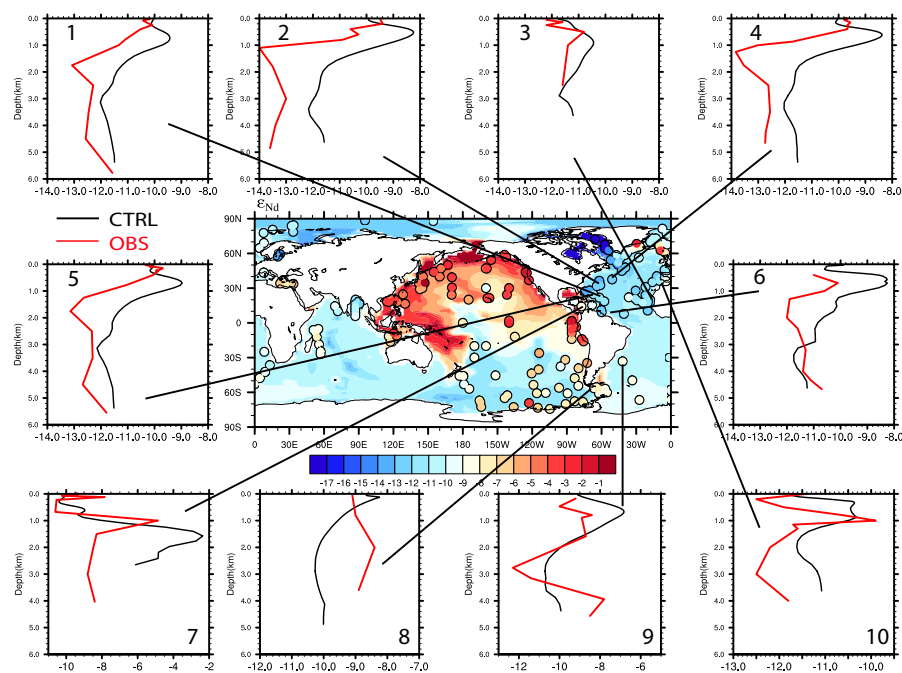


Figure 3.1.1 Comparison of present day ϵ_{Nd} fields between model and observation. (A) Global map of ϵ_{Nd} at the sea floor. Observations (van de Flierdt et al., 2016) are superimposed as filled

circles, using the same color scale. Selected vertical profiles, focusing on tropical Atlantic, show observed (red) and simulated (black) ϵ_{Nd} values.

In iPOP2_TRACE, Nd sources and ϵ_{Nd} in Nd sources are kept unchanged during the deglacial simulation. Surface dust flux and origin (Grousset et al., 1998; Lupker et al., 2010; Wolff et al., 2006) and river runoff magnitude and origin (Burton and Vance, 2000; Harris and Mix, 1999; Lézine et al., 2005; Nurnberg and Tiedemann, 2004; Rincon-Martinez et al., 2010; Stoll et al., 2007) were reported to be changing throughout time. Boundary source of Nd is not well constrained (Amakawa et al., 2000; Johannesson and Burdige, 2007; Rickli et al., 2010), therefore it is hard to estimate the change in the past, although it is highly likely to happen due to changes in different processes such as groundwater discharge (Johannesson and Burdige, 2007; Zektser and Loaiciga, 1993) and continental erosion (Tütken et al., 2002). Results from a modeling study suggest that changes in the sources are unlikely to be important, as the magnitude of the reconstructed glacial-deglacial ϵ_{Nd} variations is hard to obtain by only changing the Nd sources and/or ϵ_{Nd} in Nd sources (Rempfer et al., 2012b). In iPOP2_TRACE simulation, the change of the ocean circulation is the only factor that affects ϵ_{Nd} distribution.

3.2 Coherent AAIW response and AMOC strength

3.2.1 Reduced AAIW Northward Penetration but Increased Depth and Thickness of AAIW Water Mass during Weaker AMOC

In the modern ocean, AAIW can be identified by a low salinity (or radiogenic ϵ_{Nd}) tongue originating from the subantarctic surface ocean extending northward at the intermediate depth (Talley, 1996) (Figure 3.2.1). Here, consistent with convention, the σ_{AAIW} is defined as the potential density at the salinity minimum point in the South Atlantic mean potential temperature-salinity (θ -S) diagrams. For convenience, the AAIW depth is defined as the zonal mean depth of σ_{AAIW} at the equatorial Atlantic. The AAIW ϵ_{Nd} is defined as the zonal mean ϵ_{Nd} value at σ_{AAIW} (or AAIW depth) at the equatorial Atlantic. The σ_{AAIW} in iPOP2 under present day forcing is 27.36 kg/m^3 , which is comparable to the observation value of 27.3 kg/m^3 (Talley, 1996). The isopycnal line of

σ_{AAIW} is also consistent with the low salinity and the high ϵ_{Nd} tongue in the Atlantic (Figure 3.2.1, green line), suggesting that this is a good approximation for the location of AAIW core layer.

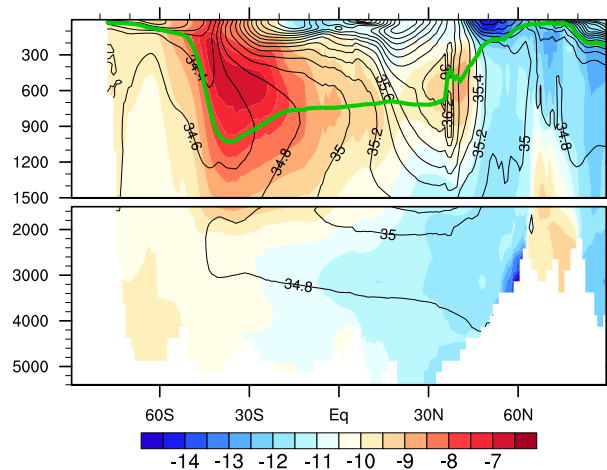


Figure 3.2.1 Model Atlantic zonal mean ϵ_{Nd} (color shading) and salinity (black contour) under present day forcing. The green line is the isopycnal line of σ_{AAIW} .

iPOP2-TRACE simulates the key oceanic changes during the last deglaciation. The simulated AMOC collapses during HS1 in response to freshwater forcing in the North Atlantic and then recovers rapidly in the BA warming (Figure 3.2.2 b, black), consistent with $^{231}\text{Pa}/^{230}\text{Th}$ records from Bermuda Rise (McManus et al., 2004)(Figure 3.2.2 b, green).

In iPOP2-TRACE, the northward penetration of AAIW in the Atlantic is closely linked to the change of AMOC. During LGM and HS1, σ_{AAIW} surface also tends to follow the low salinity, or the radiogenic ϵ_{Nd} , tongue of AAIW (green lines in Figure 3.2.3 c and d). To better quantify the northward penetration of AAIW in the Atlantic, the AAIW northward penetration latitude is estimated using Atlantic zonal mean ϵ_{Nd} : the maximum ϵ_{Nd} value in the South Atlantic above 1,200 meters is first calculated, then the latitude of AAIW northward penetration is defined as the latitude at which the ϵ_{Nd} value of 1.3 ϵ_{Nd} unit less than the maximum can reach above 1,200 meters. The AAIW northward extent varies over an approximately 15° latitude range during the deglaciation in iPOP2_TRACE

(Figure 3.2.2 c, blue dots), with a high positive correlation with the AMOC intensity. AAIW in the Atlantic can reach 2°N during the LGM, and withdraws southward after 19ka, when the AMOC starts to decrease in response to the meltwater input in the North Atlantic. By the late HS1, the AAIW retreats to its southernmost latitude of 17°S, followed by a rapid intrusion during the BA to 1°N, in response to the AMOC recovery. This HS1 southward retreat of the AAIW tongue is also obvious in the Atlantic zonal mean salinity or ϵ_{Nd} (Figure 3.2.3 c and d) and the horizontal distribution of ϵ_{Nd} at σ_{AAIW} surface (Figure 3.2.3 e and f).

Physically, the change of latitudinal extent is also consistent with that of the cross-equator transport of the AAIW (Figure 3.2.2 b red), which is defined as the northward transport between the isopycnal surfaces of $\sigma_{AAIW} \pm 0.5$ in the model. The AAIW transport is reduced during the HS1 and increased again during the BA, also following the evolution of AMOC. This result is insensitive to the choice of density interval (d), between $\sigma_{AAIW} - d$ and $\sigma_{AAIW} + d$, because similar results are produced with density intervals (d) ranging from 0.1 to 0.4 (Figure 3.2.4).

The equatorial Atlantic ϵ_{Nd} at the AAIW depth (AAIW ϵ_{Nd}) also varies closely with the AAIW northward penetration, as hypothesized in previous ϵ_{Nd} reconstructions (Huang et al., 2014; Pahnke et al., 2008; Xie et al., 2012). iPOP2_TRACE shows an almost linear relationship between the equatorial AAIW ϵ_{Nd} (Figure 3.2.2 d, solid black, which follows σ_{AAIW} and varies with depth) and the northward penetration latitude of AAIW (Figure 3.2.2 c, navy dot), with decreased ϵ_{Nd} during HS1 and its subsequent increase during BA corresponding to the southward withdraw and the subsequent northward re-advance in the penetration latitude, respectively. In the model, the ϵ_{Nd} of the AAIW southern end-member is calculated as the average of ϵ_{Nd} in the AAIW production region. It remains unchanged at -8.3 during the deglaciation prior to BA and shifts abruptly to -9.1 during BA due to the quick AMOC recovery during BA, which brings unradiogenic ϵ_{Nd} water from the North Atlantic to the Southern Ocean. The evolution of the ϵ_{Nd} difference between the equatorial Atlantic and its southern end-member (Figure 3.2.2 d, red) is similar to the evolution of the ϵ_{Nd} in the equatorial Atlantic (Figure 3.2.2

d, solid black). Therefore, ϵ_{Nd} in the equatorial Atlantic at AAIW depth can indeed be used as an indicator for AAIW northward penetration in the Atlantic.

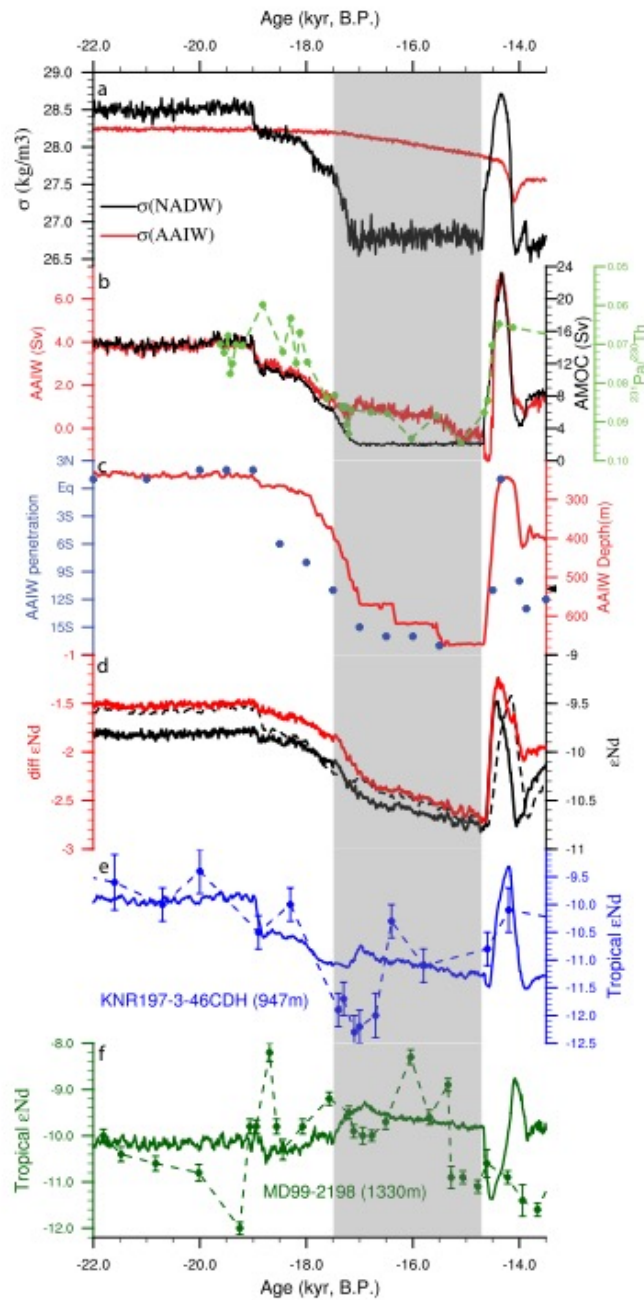


Figure 3.2.2 Evolution during the last deglaciation in reconstructions and iPOP2-TRACE. (a) Winter surface density in NADW (black) and AAIW (red) production region. (b) Model maximum AMOC transport (under 500m) in iPOP2-TRACE (black), Sedimentary $^{231}\text{Pa}/^{230}\text{Th}$ record of OCE326-5GGC (McManus et al., 2004) (dashed green) and AAIW transport which is defined as the meridional transport at equatorial Atlantic of layers between ($\sigma_{\text{AAIW}} - 0.5$) and

($\sigma_{AAIW} + 0.5$) (red). (c) Estimation of AAIW northward penetration latitude (navy dots). AAIW depth at equatorial Atlantic (red). Black triangle on the right of Y axis indicates the late Holocene AAIW depth. (d) Zonal mean AAIW ϵ_{Nd} value at equatorial Atlantic (solid black), the difference between AAIW ϵ_{Nd} value at equatorial Atlantic and AAIW end-member ϵ_{Nd} value (red) and ϵ_{Nd} value at 1,000 m at western boundary equatorial Atlantic (dashed black). (e) ϵ_{Nd} reconstruction in Demerara Rise (dashed navy) and ϵ_{Nd} evolution at this location in iPOP2-TRACE (solid navy). (f) ϵ_{Nd} records from Tobago Basin (dashed green) and ϵ_{Nd} evolution at this location in iPOP2-TRACE (solid green). HS1 is indicated by grey shading.

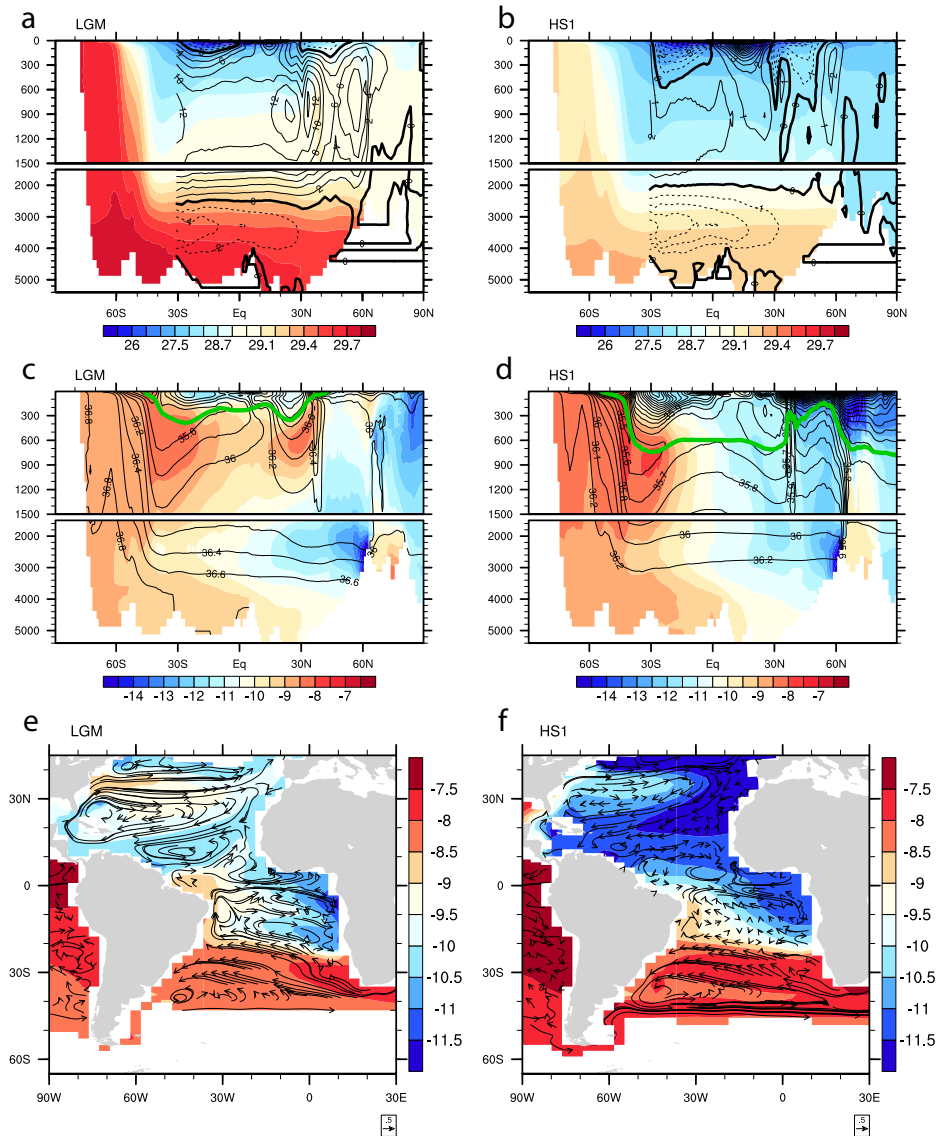


Figure 3.2.3 Comparison between LGM (20 kyr B.P.) and HS1 (16 kyr B.P.) in iPOP2-TRACE experiment. Atlantic overturning streamfunction (black contour) and Atlantic zonal mean potential density (color shading) during (a) LGM and (b) HS1. Atlantic zonal mean ϵ_{Nd} (color

shading), salinity (black contour) and isopycnal line for σ_{AAIW} (green line) at (c) LGM and (d) HS1. Circulation (vectors) and ϵ_{Nd} (color) at σ_{AAIW} surface: (e) LGM and (f) HS1.

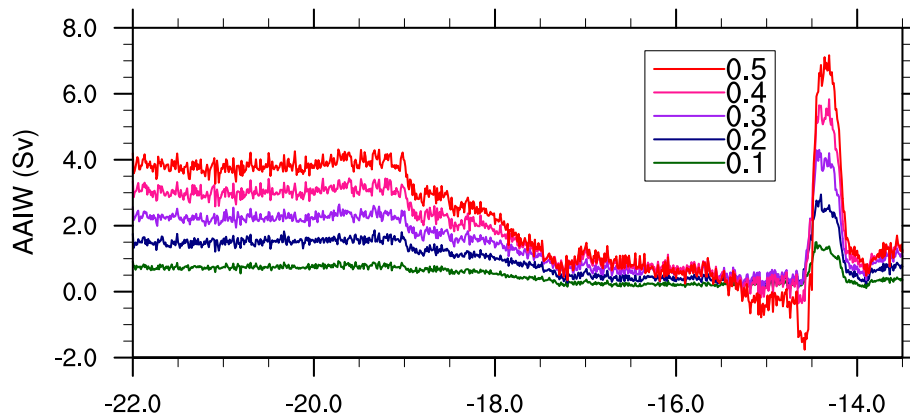


Figure 3.2.4 Northward transport at equatorial Atlantic of layers between ($\sigma_{AAIW} - d$) and ($\sigma_{AAIW} + d$): $d = 0.5$ (red), 0.4 (magenta), 0.3 (purple), 0.2 (navy) and 0.1 (green).

Another important feature of AAIW is that AAIW depth changes significantly during the last deglaciation in iPOP2-TRACE. The AAIW depth is also closely linked to the AMOC evolution, deepening from around 230-m during LGM to around 670-m during HS1, shoaling back to 240-m during BA (Figure 3.2.2 c, red) and deepening again slowly to ~ 530 -m in the Holocene (Figure 3.2.2 c, triangle on right Y axis), which is consistent with the present day observation (Talley, 1996). This deepening of AAIW from LGM to HS1 has been illustrated in previous modeling studies [e.g. *Vallis, 2000; Wolfe and Cessi, 2010*]. When the surface density in the source region of NADW is between the surface density in the source region of AAIW and AABW ($\sigma_{AAIW} < \sigma_{NADW} < \sigma_{AABW}$), which is the case during LGM in our simulation (Figure 3.2.2 a), NADW fills the mid-depth and AAIW is shallow and partially entrained in the main thermocline. However, when the surface density in the source region of NADW is less than AAIW, which is the case during HS1 in our simulation, as no NADW is produced due to the melt water input to the North Atlantic (Figure 3.2.2 a), AAIW fills the mid-depth between abyssal and main thermocline. Therefore, AAIW becomes deeper and thicker during HS1. In addition,

this magnitude of deepening of mid-depth water during HS1 has also been suggested by the deglacial atmospheric radiocarbon decline (Hain et al., 2014). Finally, the Holocene deepening compared with the glacial period may be caused partly by the sea ice retreat in the Southern Ocean (Ferrari et al., 2014).

The depth change of AAIW core layer may also contribute to ϵ_{Nd} change at a fixed depth. As the AAIW deepens, any site above (below) AAIW core layer would experience a less (more) radiogenic ϵ_{Nd} shift, which may complicate the interpretation of ϵ_{Nd} evolution as AAIW northward penetration. However, the ϵ_{Nd} in the western boundary of equatorial Atlantic shows a change of about 1 unit ϵ_{Nd} change from the LGM to the HS1 at a fixed intermediate depth of 1000m (Figure 3.2.2 d, black dash), and this change at fixed depth is comparable with the ϵ_{Nd} change at the AAIW core depth that changes with time (Figure 3.2.2 d, black solid). Therefore, the ϵ_{Nd} change from the tropical Atlantic is dominated by the change in the AAIW northward penetration change rather than AAIW depth change.

Overall, iPOP2_TRACE shows a coherent response between the AMOC intensity and the AAIW northward penetration latitude, northward transport, AAIW ϵ_{Nd} value and AAIW depth.

3.2.2 Mechanism

How does a weaker AMOC reduce the AAIW northward penetration in the Atlantic? Intuitively, one might think the AAIW northward penetration of AAIW is determined mainly by its production rate: a larger AAIW production rate would favor a stronger northward penetration towards the North Atlantic. This is not the case in iPOP2-TRACE: AAIW northward penetration is not controlled by upstream AAIW production. The AAIW subduction rate is calculated, which is the subduction across the base of the ocean mixed layer in the South Atlantic AAIW formation region (Goes et al., 2008). The AAIW subduction rate is 4.6 Sv during LGM and 6.0 Sv during HS1 in iPOP2-TRACE, indicating the upstream AAIW production during HS1 is not lower but even higher. This stronger HS1 AAIW production rate during HS1 also occurs in the fully coupled experiment TraCE21K, which shows a subduction rate of 16 Sv during LGM (consistent

with *Wainer et al.*, (2012)) and 19 Sv during HS1, although the overall magnitudes of the subduction rate are different. The relatively smaller magnitude of AAIW subduction in the ocean-alone simulation (iPOP2-TRACE) than in the fully coupled simulation (TRACE21k) is because the AAIW subduction rate depends on the mixed layer depth, which is much smaller in iPOP2-TRACE than in TRACE21k, probably because that iPOP2-TRACE is forced by monthly atmospheric forcings, in which the high frequency signals are filtered out. Regardless of these differences, the results from both simulations indicate that the retreat of AAIW northward penetration during HS1 cannot be caused by AAIW formation in the Southern Ocean.

Since the meltwater flux to the North Atlantic can reverse the density contrast between AAIW and NADW such that AAIW becomes heavier than NADW, it could encourage the northward penetration of AAIW and the southward compensating flow from the North Atlantic above AAIW, forming a reversed counterclockwise shallow overturning cell that circulates in the opposite direction to the modern AMOC (Keeling and Stephens, 2001; Saenko et al., 2003; Weaver et al., 2003). In our model, the higher surface density in the NADW formation region during LGM ($\sigma_{\text{NADW}}=28.5 \text{ kg/m}^3 > \sigma_{\text{AAIW}}=28.2 \text{ kg/m}^3$) is indeed reduced to lower than that of AAIW during HS1 ($\sigma_{\text{AAIW}}=28.0 \text{ kg/m}^3 > \sigma_{\text{NADW}}=26.8 \text{ kg/m}^3$) (Figure 3.2.2 a). However, no reversed AAIW cell is generated (Figure 3.2.3 b). The detailed mechanism of the reversed AAIW cell will be discussed in Chapter 3.2.3. In iPOP2_TRACE, during LGM, the AAIW lies above NADW, contributing to the return flow of NADW as in modern observation (Lumpkin and Speer, 2003); in response to the freshwater input during HS1, the southward export of NADW at depth collapses, which then reduces the compensating flow in the upper ocean, including AAIW. As such, the AAIW retreats to south of the equator during HS1 (Figure 3.2.3 b, d and f). This response is consistent with the present day observational (Zhang et al., 2011) and modeling studies of the multi-decadal variability of the North Brazil Current (NBC), which is found to be determined predominantly by the changes of the AMOC and NADW formation (Rühs and Getzlaff, 2015).

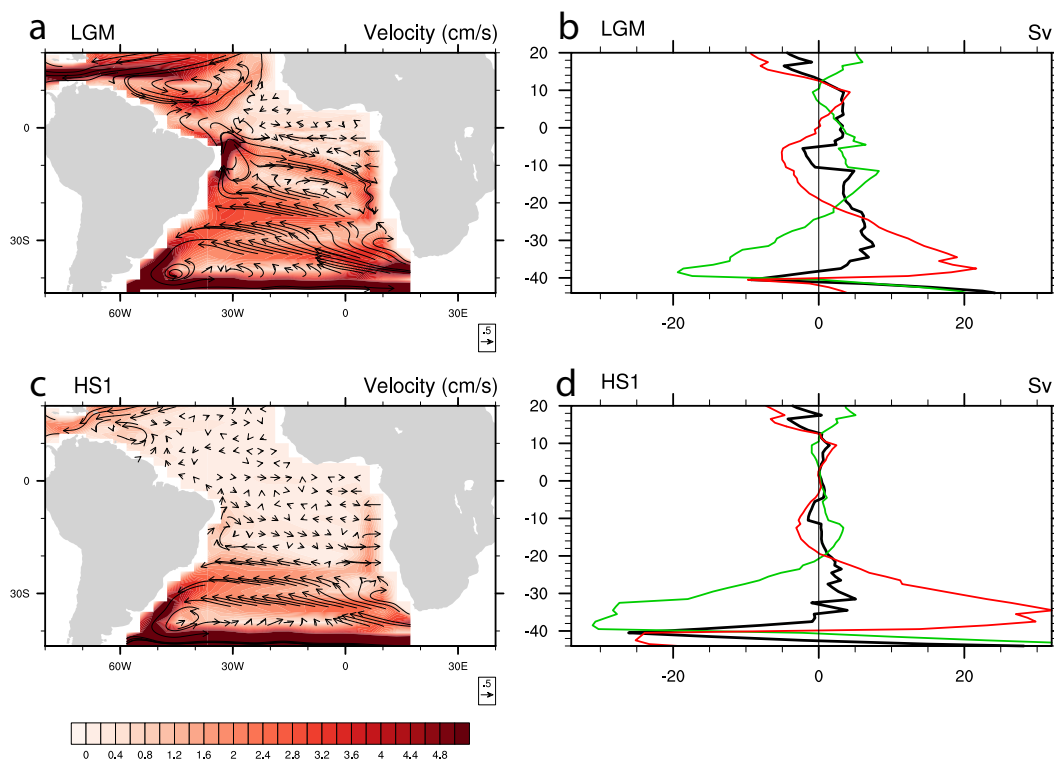


Figure. 3.2.5 Velocity and meridional transport at annual mean σ_{AAIW} surface during LGM and HS1. (a) Vectors indicate direction and magnitude of (u,v) (cm/s) and color indicate magnitude (cm/s) during LGM. (b) meridional transport (Sv) at different latitudes during LGM, green for western boundary transport, red for interior and black for total transport. Same for (c) and (d) during HS1.

iPOP2_TRACE suggests a remote dynamical control on the AAIW northward penetration from the North Atlantic, as opposed to a local control of AAIW production and transport from the Southern Ocean. Typically, the AAIW is transported northward first through the southern subtropical gyre circulation and then across the equator by the western boundary current, as in modern observations (Schmid et al., 2000). During the LGM, the AAIW flows northwestward to $\sim 20^\circ\text{S}$ in a broad interior pathway, following the counterclockwise subtropical gyre in the South Atlantic at intermediate depth (Figure 3.2.5 a); most of the AAIW water, however, recirculates back through the southward Brazil Current along the western boundary (Figure 3.2.5 b). A small residual of AAIW advances beyond 20°S northward along the western boundary into the tropical Atlantic;

this part of AAIW then crosses the equator as a part of the subsurface component of the NBC along the western boundary, generating a low salinity/high ϵ_{Nd} tongue there. During HS1, there is little AAIW transported across the equator (Figure 3.2.5 d), confining the low salinity/high ϵ_{Nd} tongue south of the equator (Figure 3.2.3 d). Upstream in the subantarctic South Atlantic, however, the northward transport of AAIW is actually increased relative to the LGM (Figure 3.2.5 b and d); this increased AAIW transport, however, is returned southward almost entirely in the Brazil Current, leaving little AAIW penetrating into the equatorial Atlantic (Figure 3.2.5 d). Thus, the deglacial evolution of the AAIW penetration to the tropical Atlantic appears to be determined predominantly by the remote processes in the North Atlantic, rather than by the local forcing in the South Atlantic subantarctic region. This remote control of AAIW in the Atlantic is similar to that in the Pacific, where the cross-equator penetration of AAIW is caused predominantly by the opening of the Indonesia Throughflow, rather than the climate forcing in the South Pacific subantarctic region (McCreary and Lu, 2001).

3.2.3 AAIW Depth, Pycnocline Depth and Shallow Reverse Cell

In Chapter 3.2.1, the evolution of AMOC strength in iPOP2_TRACE is mainly caused by the melt water forcing in the North Atlantic and AAIW depth is negatively correlated with AMOC strength. Under this North Atlantic buoyancy forcing scenario, AAIW becomes deeper when AMOC is weaker. *Toggweiler and Samuels, (1995)* suggests that NADW formation in the North Atlantic is also controlled by wind forcing in the Southern Ocean: weaker winds over the Drake Passage will lead to weaker NADW formation and shallower pycnocline depth. Since the AAIW occupies the pycnocline in the Atlantic and the AAIW depth in the modern ocean and AAIW depth does not have a specific common definition, the pycnocline depth is treated as AAIW depth. If the AAIW depth was the pycnocline depth, under the Southern Ocean wind forcing, the AAIW depth would be positively correlated with AMOC strength, which is opposite to the finding under the North Atlantic fresh water forcing. Pycnocline depth here refers to the depth of

1027.5 kg/m³ at the equator, which is the permanent pycnocline which separates the stratified upper ocean waters from dense abyssal waters (Gnanadesikan, 1999).

As noted previously, some modeling studies produce a counterclockwise shallow overturning cell that circulates in the opposite direction to the modern AMOC in the Atlantic above 1,500m during the collapse of AMOC (Keeling and Stephens, 2001; Saenko et al., 2003; Weaver et al., 2003). This counterclockwise cell is referred to as “AAIW cell” and suggests the reversal of water mass formation (Saenko et al., 2003; Stouffer et al., 2007; Weaver et al., 2003). However, as discussed in 3.2.2, the density of AAIW and NADW during LGM and HS1 in iPOP2_TRACE is reversed but no AAIW cell is produced in iPOP2_TRACE during HS1. But in the South Atlantic, the depth of the subtropical cell is deeper during HS1 than during LGM by about 400m (Figure 3.2.6 b). Is this difference between results from iPOP2_TRACE and previous studies caused by model difference or is the “AAIW cell” in previous studies just the deepening of the subtropical cell instead of reverse water mass formation?

To answer these questions, I carried out a series of sensitivity experiment modifying the surface wind stress under present day forcing and applying different magnitude of fresh water forcing to the North Atlantic. The control experiment used in Chapter 2 is the control experiment used here (CTRL). First, the Southern Ocean wind perturbation experiment is carried out (WD_SO), which reduces the surface wind stress to the 1% of the wind stress over 40°S to 60°S in the Southern Ocean. Experiment reducing the surface wind stress to the 1% of the magnitude in CTRL over 0°S to 40°S in the Atlantic is also carried out (WD_0040S). In addition to that, fresh water forcing with the magnitudes of 0.1 Sv, 0.3 Sv, 0.7 Sv and 1.0 Sv are applied to 50°N-70°N in the North Atlantic with the wind stress the same as CTRL, named as HOSING_01, HOSING_03, HOSING_05, HOSING_07 and HOSING_10 respectively. The last experiment is the experiment with 1% of the wind stress over 0°S to 40°S in the Atlantic and 1.0 Sv fresh water over 50°N-70°N in the North Atlantic (WD_0040S_hosing). All the experiments are forced by CORE-II data (Large and Yeager, 2008) with the additional

modification described above using iPOP2. The results discussed below are the equilibrium results.

When there is almost no Southern Ocean wind, AMOC is weakened and the pycnocline depth is shallower comparing to CTRL, consistent with the theory by Gnanadesikan, (1999) which predicts that the pycnocline is deepened by Southern Ocean wind and shallowed by NADW formation. At the same time, Southern Ocean wind will also influence NADW formation. Therefore, the relationship between pycnocline depth and AMOC strength depends on what forcing it is: Southern Ocean wind forcing or North Atlantic buoyancy forcing. Modeling results by iPOP2 are consistent with the theory. The pycnocline depth changes from 912m in CTRL to 542 m in WD_SO and the AMOC strength changes from 15.6 Sv in CTRL to 7.1 Sv in WD_SO (Table 3.2.1 and Figure 3.2.6), consistent with Gnanadesikan, (1999) and Toggweiler and Samuels, (1995). Increase wind stress over the Southern Ocean will increase the slope of isopycnal in the subantarctic region and leads to the deepening of isopycnal. The pycnocline depth is positively correlated with AMOC strength if the forcing is the Southern Ocean wind. If the forcing in the North Atlantic, with the increase of fresh water forcing in the North Atlantic, AMOC decreases (Figure 3.2.7 a) and the pycnocline depth increase (Figure 3.2.7 d), consistent with Gnanadesikan, (1999).

However, the AAIW depth behaves differently from the pycnocline depth. In WD_SO, the AAIW depth is slighter deeper than CTRL, which is opposite to the pycnocline change in WD_SO. The deepening of AAIW is caused by the shift in the AAIW density. The AAIW density is 1027.38 kg/m^3 in CTRL, which increased to 1027.64 kg/m^3 in WD_SO. The depth of 1027.38 kg/m^3 isopycnal in WD_SO is 437m, which is consistent with the shallowing of pycnocline in WD_SO. However, this shallowing of the isopycnal of a specific value is overwhelmed by the shift of AAIW density. The increase of AAIW density in WD_SO is probably caused by the southward shift in the AAIW formation region (Figure 3.2.6 c and d). With almost no wind over 40°S - 60°S , there is no more northward Ekman transport. Therefore, the fresh AAIW is formed in the further south beyond 60°S and the AAIW density increases. The WD_SO

suggests that the pycnocline depth and AAIW depth are different but both of them are influenced by the Southern Ocean wind and NADW formation.

	CTRL	WD_SO
AMOC (Sv)	15.6	7.1
AAIW density (kg/m^3)	1027.38	1027.64
AAIW depth (m)	730	773
Pycnocline depth (m)	912	542

Table 3.2.1 AMOC strength, AAIW depth and Pycnocline depth in CTRL and WD_SO.

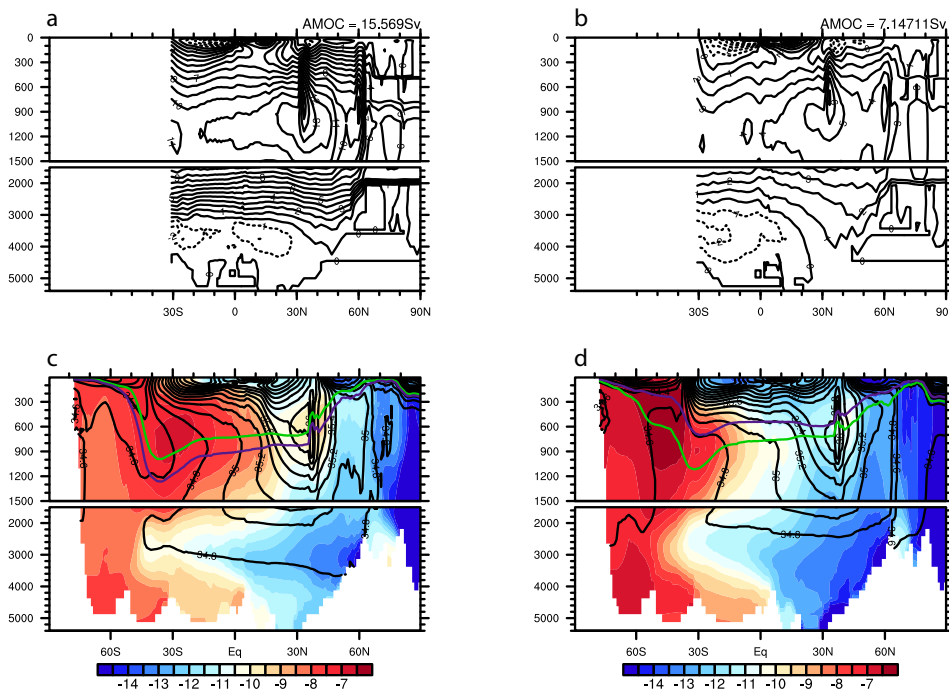


Figure 3.2.6 AMOC in CTRL (a) and WD_SO (b). Atlantic zonal mean ϵ_{Nd} (color contour) and salinity (line contour) in CTRL (c) and WD_SO (d). Green line indicates the AAIW depth and the purple line indicates the pycnocline depth.

iPOP2 can produce the similar counterclockwise shallow cell in the upper 1,000m in the Atlantic as in previous studies with the increase of hosing magnitude. With the increase of hosing magnitude, AMOC strength decreases and the shallow reverse cell

develops (Figure 3.2.7). In HOSING_10, when the freshwater forcing in the North Atlantic is 1 Sv, AMOC is reduced to 2 Sv, which is almost collapsed (AMOC_off). The counterclockwise shallow cell forms in the upper ocean in the South Atlantic, which is similar to the cell in previous studies (Saenko et al., 2003; Stouffer et al., 2007; Weaver et al., 2003). This shallow cell gets stronger and deeper with the reduce of AMOC (Figure 3.2.8). The depth of this cell is defined as the depth of 0 contour of this cell at 15°S in the overturning streamfunction. The strength of this cell is the maximum streamfunction in the upper 1,000m in the South Atlantic. These sensitivity experiments suggest that iPOP2 can also produce this counterclockwise shallow cell in the South Atlantic. The AMOC pattern during HS1 in iPOP2_TRACE is similar to the AMOC pattern in HOSING_05. Therefore, no reverse cell in HS1 is not because of model difference but is cause by different forcings.

The formation of this shallow reverse cell is suggested to be caused by the change of density reverse between AAIW and NADW (Saenko et al., 2003; Weaver et al., 2003). Although in the HOSING experiment, with the freshening of NADW, the density of NADW becomes smaller than the AAIW density (Figure 3.2.2 a), sensitivity experiments suggest that the reverse cell is caused by the deepening of the wind driven subtropical cell in the South Atlantic. Comparing with HOSING_10, in WD_0040S_HOSING, with reduced with stress over 0°S to 40°S in the Atlantic, the reverse cell depth and strength is greatly reduced, suggesting the role of surface wind in this shallow cell. The deepening of this wind driven subtropical cell during weak AMOC is caused by the reduced upper ocean stratification in response to the North Atlantic fresh water forcing.

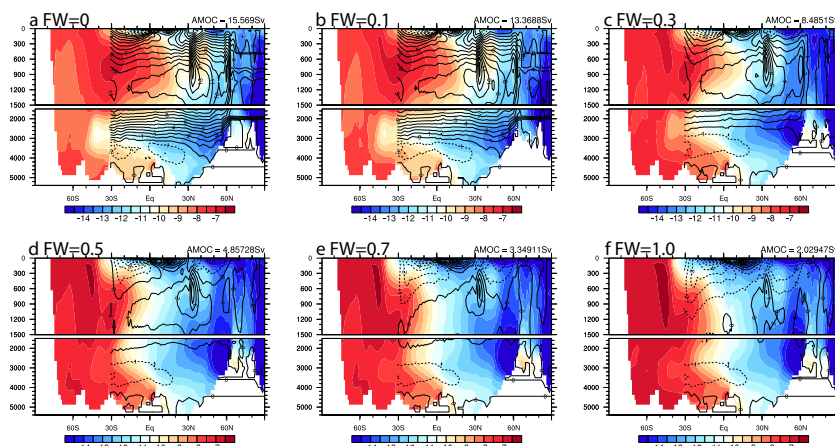


Figure 3.2.7 AMOC in CTRL (a), HOSING_01 (b), HOSING_03 (c), HOSING_05 (d), HOSING_07 (e) and HOSING_10 (f).

The counterclockwise cell during AMOC_{off} cannot transport AAIW to the North Atlantic as previously suggested (Saenko et al., 2003; Weaver et al., 2003). With the decrease of AMOC strength, the northward penetration of AAIW also becomes weaker (Chapter 3.2.2). The difference of the average ϵ_{Nd} of water in the density range from 1027.4 kg/m^3 - 1027.6 kg/m^3 between equator and 40°S can be used to be an index for the AAIW northward penetration. Hosing experiments show that the northward penetration of AAIW is positively correlated with AMOC strength, consistent with the results in Chapter 3.2.2. In HOSING_10, with the maximum strength of the reverse cell, the northward penetration of AAIW is the weakest.

A series of sensitivity experiments in this chapter answer the AAIW related questions in Chapter 3.2.2. Firstly, AAIW depth is not the pycnocline depth. AAIW depth is controlled by AMOC strength as well as the density of water at AAIW formation. Secondly, iPOP2 can produce the counterclockwise shallow cell if the freshwater forcing is large enough and this shallow cell is not related to AAIW transport. Therefore, this study suggests a consistent picture of a deeper but less northward AAIW during weak AMOC state.

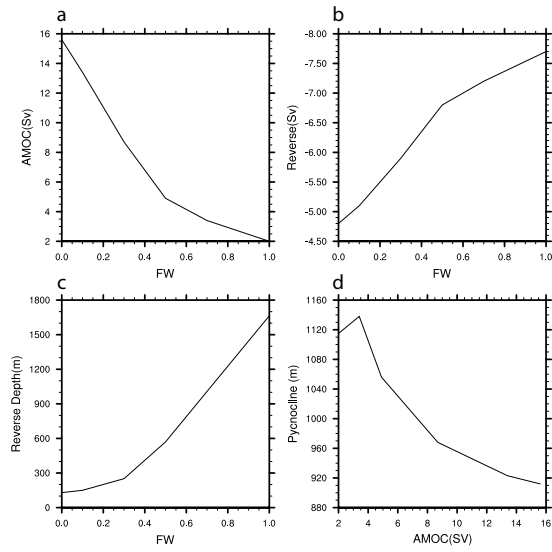


Figure 3.2.8 AMOC strength, reverse cell strength, reverse cell depth and pycnocline depth in CTRL, HOSING_01, HOSING_03, HOSING_05, HOSING_07 and HOSING_10.

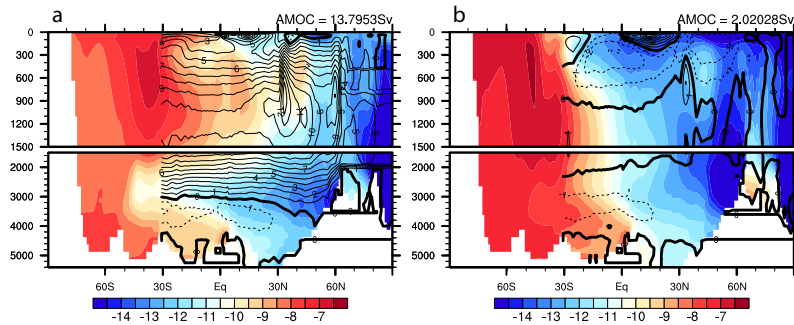


Figure 3.2.9 AMOC in WD_0040S (a) and WD_0040S_HOSING (b).

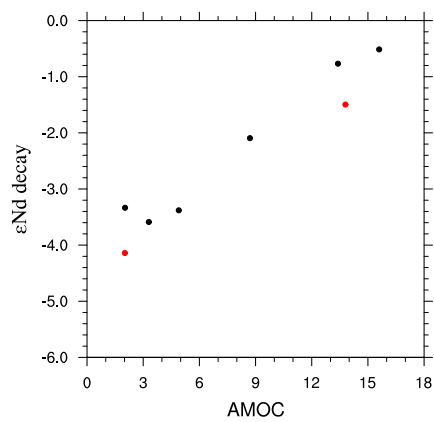


Figure 3.2.10 The AAIW ϵ_{Nd} decay and the AMOC strength in the sensitivity experiments. The black dots are experiments with no change of wind stress. The red dots are the experiments with the change of wind stress over 0°S to 40°S in the Atlantic.

3.3 Reconciling ϵ_{Nd} Reconstructions Controversy with Core Depth

As noted above, available tropical ϵ_{Nd} reconstructions show contradictory ϵ_{Nd} evolutions across the last deglaciation. The ϵ_{Nd} reconstruction from the Tobago Basin (MD99-2198, 12.09°N, 61.23°W, 1330m) (Pahnke et al., 2008) shows an increase (becomes more radiogenic) during the HS1 (Figure 3.2.2 f), which was interpreted as enhanced northward advection of AAIW. However, ϵ_{Nd} records from the Florida Strait (KNR166-2-26JPC, 24°19.62'N, 83°15.14'W, 546m) (Xie et al., 2012) (Figure 3.3.1 c) and the Demerara Rise (KNR197-3-46CDH, 7.836°N, 53.663°W, 947m) (Huang et al., 2014) (Figure 3.2.2 e) show decreases (become less radiogenic) during the HS1, and were interpreted to indicate decreased penetration of AAIW into tropical North Atlantic.

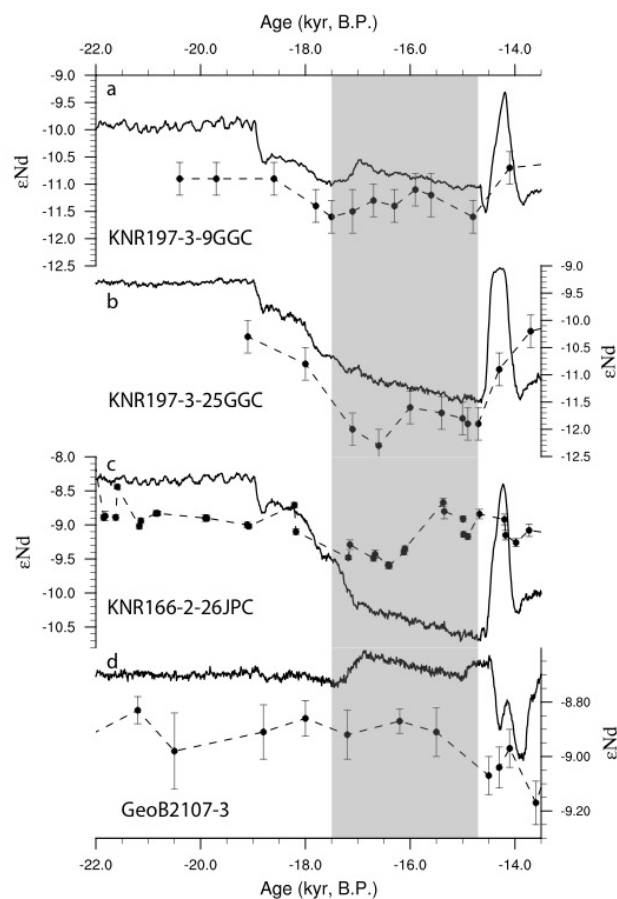


Figure 3.3.1 Comparison between model ϵ_{Nd} (solid) with reconstructions (dash). (a) KNR197-3-9GGC in Demerara Rise ($7^{\circ}55.8'N$, $53^{\circ}34.51'W$, 1100m) (Huang et al., 2014). (b) KNR197-3-25GGC in Demerara Rise ($7^{\circ}42.27'N$, $53^{\circ}47.12'W$, 671m) (Huang et al., 2014). (c) KNR166-2-26JPC in the Florida Straits ($24^{\circ}19.62'N$, $83^{\circ}15.14'W$, 546m) (Xie et al., 2012). (d) GeoB2107-3 in southern Brazil margin ($27.2^{\circ}S$, $46.5^{\circ}W$, 1050m) (Howe et al., 2016a)

iPOP2_TRACE is able to reproduce the ϵ_{Nd} evolutions at different sites from intermediate depth. The ϵ_{Nd} from the Demerara Rise ($\sim 950m$) (Figure 3.2.2 e and Figure 3.3.1 a and b) and from the Florida Strait ($\sim 540m$) (Figure 3.3.1 c) exhibit less radiogenic excursion during HS1, while ϵ_{Nd} from the Tobago Basin ($\sim 1330m$) shows a more radiogenic shift during HS1 (Figure 3.2.2 f). The diverse ϵ_{Nd} evolutions simulated in iPOP2_TRACE, which are consistent with the reconstructions at these three tropical North Atlantic sites, suggest that the opposite ϵ_{Nd} evolutions at these locations are physically consistent with a common deglacial ocean circulation change. The interpretation, however, is more complex than suggested in previous studies because it

involves both the change of the AAIW depth and the radiogenic water from the Gulf of Mexico and the Caribbean Sea, as discussed below.

iPOP2_TRACE shows that the less radiogenic shift of ϵ_{Nd} from the Florida Strait site (KNR166-2-26JPC) during HS1 (Xie et al., 2012) is due to the reduced influence of the radiogenic water from the bottom in the Gulf of Mexico and the Caribbean Sea. Deep water from the Gulf of Mexico and the Caribbean Sea features very radiogenic ϵ_{Nd} sources from boundary exchange (Jeandel et al., 2007; Osborne et al., 2014). During LGM, active AMOC drives strong upwelling in this region (Figure 3.3.2 a, black contour), which, in turn, influences the shallow layers with very radiogenic ϵ_{Nd} water in this region and the nearby open ocean in the subtropical North Atlantic. The influence of this regional radiogenic ϵ_{Nd} source can also be seen in the Atlantic zonal mean ϵ_{Nd} as a high ϵ_{Nd} center located at 600m-900m from 20°N to 40°N (Figure 3.2.3 c). During HS1, however, this radiogenic ϵ_{Nd} bottom water is trapped in the bottom locally because of reduced upwelling (Figure 3.3.2 a, black contour). This leads to a great reduction in the transport of radiogenic ϵ_{Nd} water from bottom to shallow layers, and therefore, a unradiogenic ϵ_{Nd} shift in the upper 1,500 m in the Gulf of Mexico and the Caribbean Sea (Figure 3.3.2 color contour) and, eventually, in the upper 1,000 m in subtropical North Atlantic as there is no more a radiogenic ϵ_{Nd} center in subtropical North Atlantic in the zonal mean ϵ_{Nd} (Figure 3.2.3 d). Furthermore, the ϵ_{Nd} from the Florida Strait site is dominated by radiogenic horizontal advection (Figure 3.3.3 a) by an eastward flow from the Gulf of Mexico (Figure 3.3.3 b). ϵ_{Nd} at this site experiences an unradiogenic shift during HS1 because with reduced input of deep radiogenic waters, the upper ocean in the Gulf of Mexico becomes less radiogenic and at the same time, the eastward flow also becomes weaker (Figure 3.3.3 b). Thus, ϵ_{Nd} variations in the Florida Strait are not due to variations in AAIW as previously suggested (Xie et al., 2012).

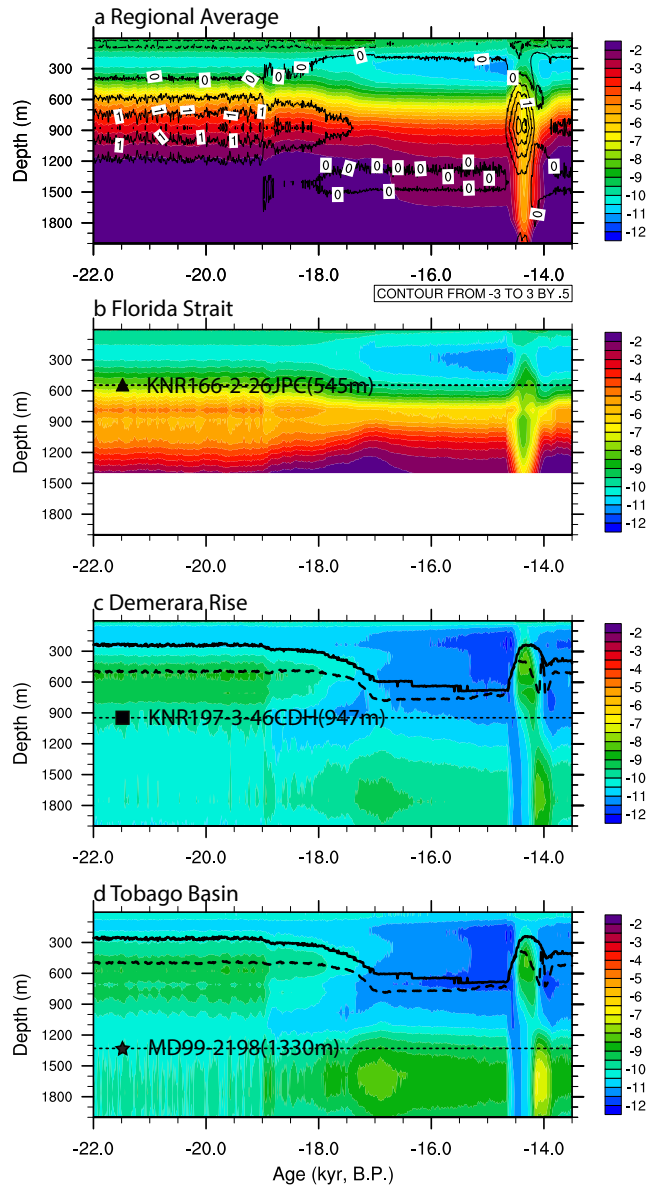


Figure 3.3.2: ϵ_{Nd} evolution for the upper 2,000m at four different locations in the tropical North Atlantic sites. (a) Area average from Gulf of Mexico and Caribbean Sea (15°N - 30°N , 85°W - 100°W). Black contours are vertical velocity in 10^{-4} cm/s. (b) (24.33°N , 83.25°W), which is the horizontal location for site KNR166-2-26JPC in Florida Strait (c) (7.84°N , 53.66°W), which is the horizontal location for site KNR197-3-46CDH in Demerara Rise and (d) (12.09°N , 61.23°W), which is the horizontal location for site MD99-2198 in Tobago Basin. The depth of each core is indicated by a thin black dash line with filled symbol: KNR166-2-26JPC(triangle), KNR197-3-46CDH (square) and MD99-2198 (star). The depth of σ_{AAIW} is indicated by thick black lines in C and D: σ_{AAIW} by salinity (solid, defined in text) and σ_{AAIW} by ϵ_{Nd} (dash, defined as average of potential density where ϵ_{Nd} reaches maximum vertically Atlantic average from 40°S to equator). The maximum ϵ_{Nd} tongue is shifted slightly deeper in the minimum salinity tongue, because of the reversible scavenging by settling particles (Rempfer et al., 2011).

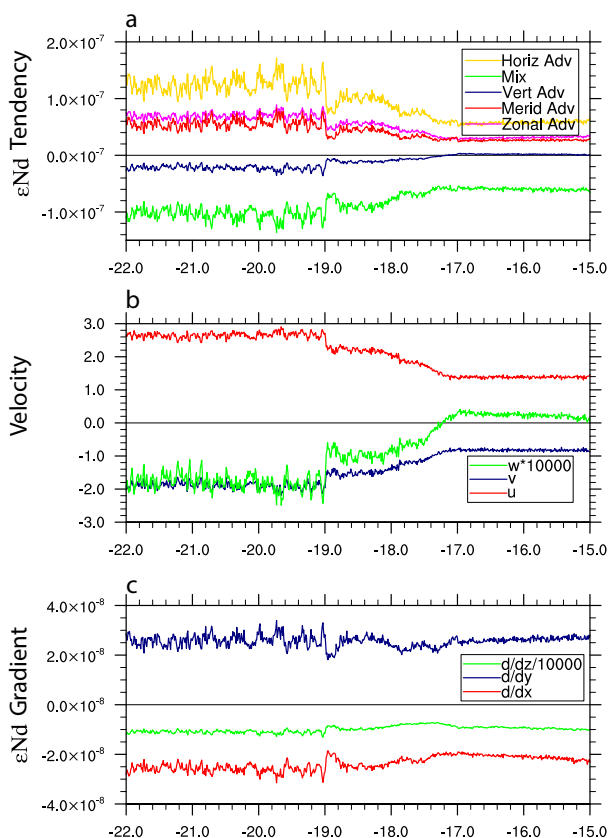


Figure 3.3.3 ϵ_{Nd} tracer budget analysis for ($12^{\circ}N$, $75^{\circ}W$, 1330m), which is near MD99-2198. (a), time series of ϵ_{Nd} tendency terms: zonal advection (magenta), meridional advection (red), horizontal advection (zonal advection + meridional advection) (yellow), vertical advection (navy) and mixing (green). (b), evolution of velocity: zonal velocity (u) (red), meridional velocity (v) (navy) and vertical velocity multiplied by 10^4 (w) (green). (c), ϵ_{Nd} gradient: zonal gradient (red), meridional gradient (navy) and vertical gradient (green).

iPOP2_TRACEA further suggests that the opposite ϵ_{Nd} behaviors at two nearby sites from the Demerara Rise and the Tobago Basin discussed above are caused by the different depths of the sediment cores as well as the influence of radiogenic ϵ_{Nd} water from the Caribbean Sea. Both locations experience similar ϵ_{Nd} change in the upper 2,000m (Figure 3.3.2 c and d). During the LGM, the Demerara Rise site is located in the lower limb of AMOC (as shown in southward meridional velocity in Figure 3.3.4 a and Figure 3.3.5 c), with water transported from the subtropical North Atlantic and the Caribbean Sea. Starting from 19ka, AMOC begins to decrease in response to the fresh water forcing applied to the North Atlantic, ϵ_{Nd} in the subtropical North Atlantic becomes

less radiogenic due to the reduced influence of the radiogenic source water from the bottom of the Gulf of Mexico and the Caribbean Sea as discussed above. In the meantime, the meridional velocity also begins to decrease (Figure 3.3.5 c), leading to a decrease in the radiogenic ϵ_{Nd} advection term (Figure 3.3.5 a). During HS1, the flow is almost stagnant (Figure 3.3.5 c) and all the ϵ_{Nd} tendency terms are greatly reduced compared with LGM (Figure 3.3.5 a). Therefore, the less radiogenic shift in ϵ_{Nd} during HS1 from the Demerara Rise is due to the reduced influence of radiogenic water from bottom of the Gulf of Mexico and the Caribbean Sea as well as the reduced southward flow, instead of the retreat of northward advection of AAIW suggested in *Huang et al.*, [2014].

The Tobago Basin site is about 400 meters deeper than the Demerara Rise site and is mainly influenced by the NADW from the north, which features unradiogenic ϵ_{Nd} values. During LGM, strong southward western boundary current contributes to the unradiogenic ϵ_{Nd} advectations at the Tobago Basin site (Figure 3.3.4 b and Figure 3.3.5 b). When AMOC collapsed during HS1, this unradiogenic ϵ_{Nd} advection of NADW is also reduced (Figure 3.3.5 b and d), which then contributes to the more radiogenic shift of ϵ_{Nd} during HS1 as in the ϵ_{Nd} reconstruction. In addition, circulation change in the Caribbean Sea also contributes to the more radiogenic ϵ_{Nd} shift in the Tobago Basin during HS1. During LGM, flow at the location where the Caribbean Sea connects with the Atlantic (12°N, 75°W, 1330m) is westward and therefore leads to a less radiogenic ϵ_{Nd} advection into the the Caribbean Sea (Figure 3.3.5 b and Figure 3.3.6 a). During HS1, however, the westward flow is changed to eastward flow out of the Caribbean Sea, because of the reduced deep west boundary current (Figure 3.3.4 d and Figure 3.3.6 b). This eastward flow out of the Caribbean Sea transports radiogenic ϵ_{Nd} water from the Caribbean Sea out to influences the Tobago Basin site. Therefore, the more radiogenic ϵ_{Nd} shift during HS1 in Tobago Basin site is caused by both the retreat of the unradiogenic ϵ_{Nd} NADW and the leak of radiogenic ϵ_{Nd} water from the Caribbean Sea. Again, variations in the northward extent of AAIW did not control the ϵ_{Nd} evolution in this Tobago Basin site, contrary to what was suggested previously (Pahnke et al., 2008).

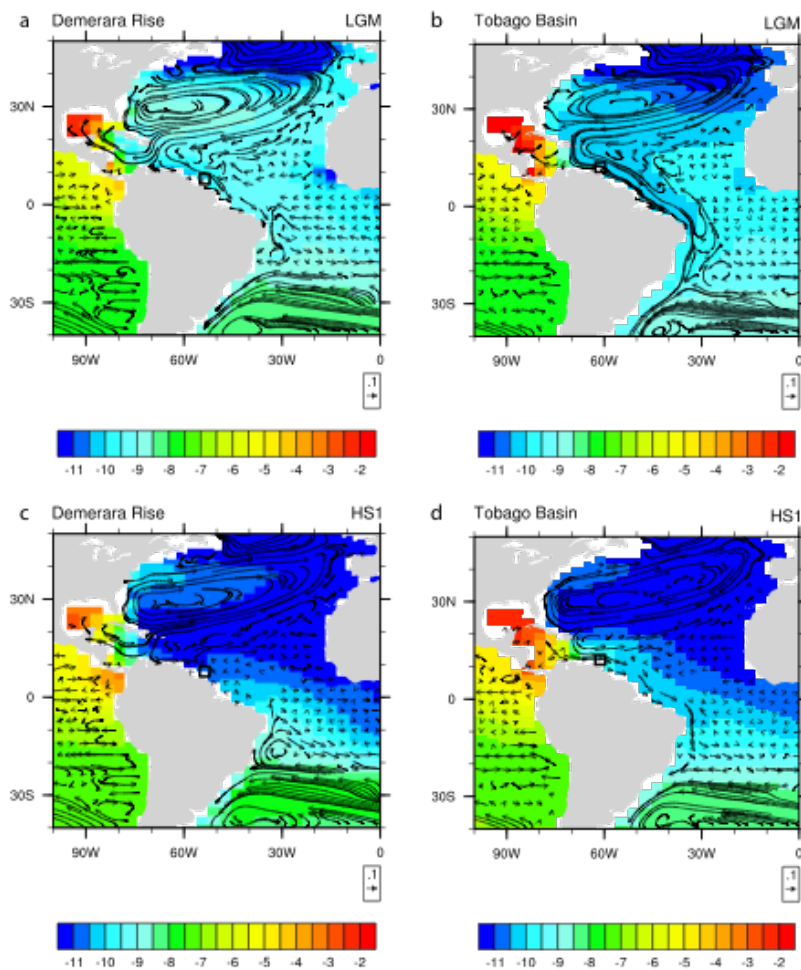


Figure 3.3.4 Ocean current (vector) and ϵ_{Nd} (color) at the depth of KNR197-3-46CDH (947m) (a and c) and MD99-2198 (1330m) (b and d) during LGM and HS1. The location of each site is indicated by a black box.

The discussion above suggests that deglacial ϵ_{Nd} in the low latitude North Atlantic at the depth of modern AAIW can be complicated by the radiogenic ϵ_{Nd} end-member from the Gulf of Mexico and the Caribbean Sea. From LGM to HS1, our model ϵ_{Nd} exhibits an unradiogenic shift above around 1,100-m and a more radiogenic shift from 1,100-m to 2,000-m at both the Demerara Rise and the Tobago Basin (Figure 3.3.2 c and d), consistent with the respective proxy records. Above 1,100-m, low latitude North Atlantic ϵ_{Nd} can be influenced by both southern sourced water of AAIW in the upper layers and northern sourced water from the Caribbean Sea, both of which become weaker and lead

to an unradiogenic shift of ϵ_{Nd} when AMOC strength is reduced. Below 1,100-m, water is influenced mainly by the NADW as well as water from the Caribbean Sea. The retreat of NADW and the advance of the Caribbean Sea water both lead to a radiogenic shift of ϵ_{Nd} during reduced AMOC. Therefore, radiogenic ϵ_{Nd} water from the Gulf of Mexico and the Caribbean Sea provides effectively the third ϵ_{Nd} end-member in addition to the radiogenic ϵ_{Nd} south sourced AAIW and unradiogenic ϵ_{Nd} north sourced water. This third source should be taken into consideration when interpreting ϵ_{Nd} reconstructions from low latitude North Atlantic at modern intermediate depth.

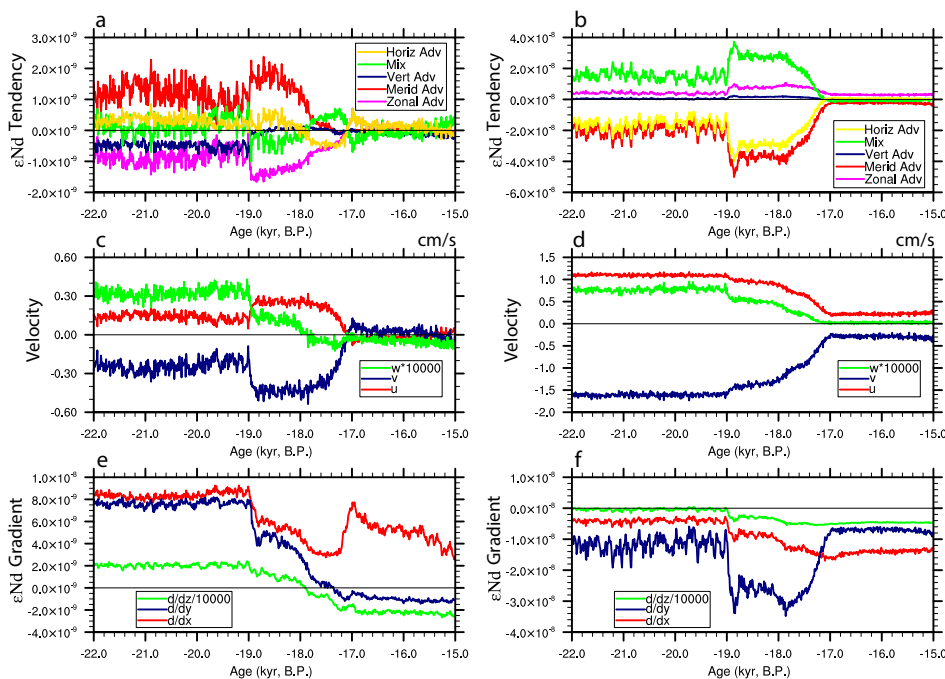


Figure 3.3.5 ϵ_{Nd} tracer budget analysis for site KNR197-3-46CDH (a, c and e) and MD99-2198 (c, d and f). (a) and (b), time series of ϵ_{Nd} tendency terms: zonal advection (magenta), meridional advection (red), horizontal advection (zonal advection + meridional advection) (yellow), vertical advection (navy) and mixing (green). (c) and (d), evolution of velocity: zonal velocity (u) (red), meridional velocity (v) (navy) and vertical velocity multiplied by 10^4 (w) (green). (e) and (f), ϵ_{Nd} gradient: zonal gradient (red), meridional gradient (navy) and vertical gradient (green).

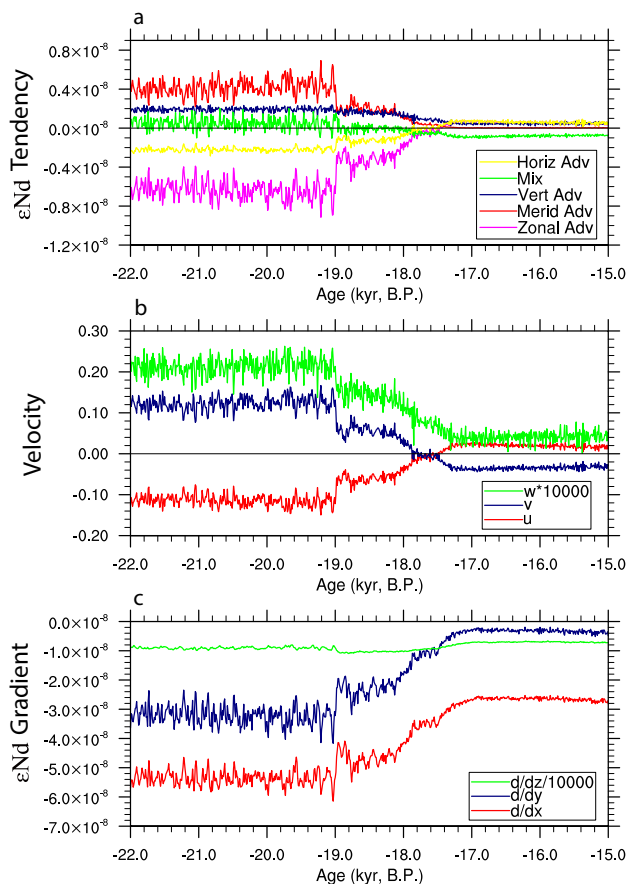


Figure 3.3.6 ϵ_{Nd} tracer budget analysis for ($12^{\circ}N$, $75^{\circ}W$, 1330m), which is near MD99-2198. (a), time series of ϵ_{Nd} tendency terms: zonal advection (magenta), meridional advection (red), horizontal advection (zonal advection + meridional advection) (yellow), vertical advection (navy) and mixing (green). (b), evolution of velocity: zonal velocity (u) (red), meridional velocity (v) (navy) and vertical velocity multiplied by 10^4 (w) (green). (c), ϵ_{Nd} gradient: zonal gradient (red), meridional gradient (navy) and vertical gradient (green).

It should also be pointed out that the interpretation of the deglacial ϵ_{Nd} records from the tropical Atlantic can also be complicated by the changing depth of the AAIW during the deglaciation. Our model shows a much shallower AAIW during LGM than the present day (Figure 3.2.1 c). Sites located at modern AAIW depth may not be influenced by AAIW in the past. In iPOP2-TRACE, in the western boundary of equatorial Atlantic, for the upper 900 meters, flow is northward which contributes to a radiogenic ϵ_{Nd} advection, indicating an AAIW influence. Therefore, we suggest that ϵ_{Nd} reconstructions shallower than 900 meters from equatorial and tropical Atlantic are more suitable to

reconstruct past AAIW northward penetration change. The complicated mechanisms controlling ϵ_{Nd} reconstruction at different sites from the tropical North Atlantic, however, also indicates that more reconstructions from different locations and depths are needed to infer past circulation changes as suggested by *van de Flierdt et al.*, [2016].

3.4 Conclusion and Discussion

Overall, our transient Nd-enabled ocean model simulation suggests a coherent AAIW response to the change of AMOC strength. The northward AAIW penetration in the tropical Atlantic is determined predominantly by the AMOC intensity or climate in the high latitude of the North Atlantic remotely, with a stronger AMOC enhancing AAIW northward penetration. In addition, AAIW water mass sinks to a greater depth and dominates a wider water depth range in response to the freshening of NADW. AAIW is a critical part of the return flow of the southward flowing NADW and, in turn, the global thermohaline circulation, and therefore can contribute significantly to the global climate change. Also, monitoring changes of AAIW can contribute to our understanding of climate changes in the past and help future projections.

In addition, ϵ_{Nd} reconstructions from the tropical and subtropical North Atlantic from within and near modern AAIW depths do not inform us about northward AAIW extent as previously assumed. iPOP2_TRACE reproduces the contrasting deglacial ϵ_{Nd} evolutions at three intermediate-depth sites in the tropical North Atlantic. The inconsistency among reconstructions relates to the individual site locations and depths. With the AAIW depth changing in the past, core sites bathed by AAIW in present day, such as the Demerara Rise site, may not be influenced by AAIW in the past. In addition, the radiogenic ϵ_{Nd} water from the Gulf of Mexico and the Caribbean Sea is important as the third end-member for regulating ϵ_{Nd} values at intermediate depth in tropical North Atlantic, which complicates the interpretation of ϵ_{Nd} reconstruction in the tropical North Atlantic. During the AMOC-on state (LGM), upwelling in the Gulf of Mexico and the Caribbean Sea brings very radiogenic water from the bottom to shallow depth, influencing the upper 1,000 m of the tropical and subtropical Atlantic (Figure 3.4.1 c).

During the AMOC-off state (HS1), this upwelling is greatly reduced and the upper 1,000 m subtropical and tropical Atlantic ϵ_{Nd} experience an unradiogenic shift (Figure 3.4.1 d), which, combined with a weak deep western boundary current, lead to the unradiogenic shift in reconstruction of the Demerara Rise site (Figure 3.4.1 c and d). The radiogenic shift in the reconstruction of the Tobago Basin site during HS1 is due to the reduced deep western boundary current as well as leakage of radiogenic water from the Caribbean Sea (Figure 3.4.1 e and f). Therefore, it is important to take the influence of radiogenic water from the Gulf of Mexico and the Caribbean Sea into consideration when interpreting ϵ_{Nd} reconstructions from the tropical Atlantic within and near modern AAIW. Eventually, more reconstructions from different depths and latitudes, and comparison of these records to simulations using Nd-enabled models, will help to improve our understanding of past circulation.

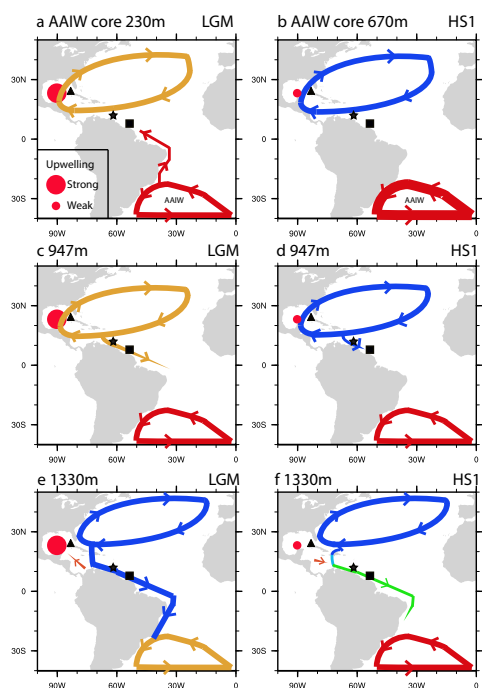


Figure 3.4.1. Schematic figure of circulation and ϵ_{Nd} during LGM and HS1 at different depth: AAIW core depth (A and B), 947 m (C and D) and 1330 m (E and F). Red filled circle represents upwelling in the Gulf of Mexico and Caribbean Sea, with larger size for stronger upwelling. Curves with arrows represents flow, with thickness for flow magnitude and color from blue to green to yellow to red for the increasing of ϵ_{Nd} . Locations of each observational site are indicated by filled symbols: KNR166-2-26JPC: (24°19.62'N, 83°15.14'W, 546m), triangle; MD99-2198: (12.09°N, 61.23°W, 1330m), star; KNR197-3-46CDH: (7.836°N, 53.663°W, 947m), square.

4. Using Horizontal $\delta^{18}\text{O}_c$ Gradient to Reconstruct Past Overturning Strength

4.1 Transient Deglacial Simulation Set Up

To explore the problems stated in Chapter 1, a transient simulation simulating the deglacial ocean changes is carried out using isotope-enabled ocean model with active ecosystem module (CTRACE). iPOP2 is first spun up under LGM condition for 4,000 years and then the transient forcing for the deglaciation starting at 22ka is applied. iPOP2 is forced by the monthly output from coupled transient experiment TraCE21K using the Community Climate System Model version 3 (CCSM3) under realistic climate forcing (He, 2011; Liu et al., 2009), which captures many features of the climate change during the last deglaciation. The surface wind stress is directly from TraCE21K, while surface heat and freshwater are applied using hybrid boundary condition, which is a combination of flux forcing and surface restoring (Zhang et al., 2017). This method has been successfully used in Zhang et al., (2017) to simulate deglacial ocean evolution using iPOP2 (iPOP2_TRACE). The differences between the new CTRACE experiment and iPOP2_TRACE are as follows:

- (1) New hybrid boundary condition parameters will be used. There are two problems in iPOP2_TRACE: one is that the AMOC strength during the Holocene is 9 Sv, which is 44% smaller than 1990-control value; the other is that in TraCE21K warming in the deep Southern Ocean begins at approximately 17ka, but in iPOP2_TRACE, the deep Southern Ocean does not warm up. In iPOP2_TRACE, the restoring time for temperature and salinity is 10-day and 30-day. After more sensitivity test on these two parameters by Jiaxu Zhang, a combination of a 30-day for temperature and 60-day for salinity is suggested to be able to solve both of the problems. Therefore, in CTRACE, new parameters for heat and freshwater restoring will be used.
- (2) Overflow and tidal mixing will be turned on following the methods in Brady et al., 2013. Overflow parameterization allows for overflow flow transport across shallow ridges such as Denmark Strait, Faroe Bank Channel, Weddell Sea and

Ross Sea (Yeager and Danabasoglu, 2012). During the LGM, because of the increased land areas and ice shelves compared with present day, the overflow is simply turned off in iPOP2_TRACE. In CTRACE, overflow in the Southern Hemisphere will be turned off while overflow in the Northern Hemisphere will be kept as present day (Brady et al., 2013).

- (3) In CTRACE, in addition to the water isotopes, age tracers, Nd isotopes, abiotic ^{14}C , additional tracers will be added, including ^{231}Pa and ^{230}Th and carbon isotopes, which are all coupled with active ecosystem module.
- (4) Improved parameterization for Nd isotopes. The parameters used for Nd isotopes have been discussed in Chapter 2.1.

Overall, the physical circulation in CTRACE mainly reproduces the TraCE21K results (He, 2011; Liu et al., 2009) (Figure 4.1.1). The good representation of the physical circulation assures the reasonable tracer field in this study.

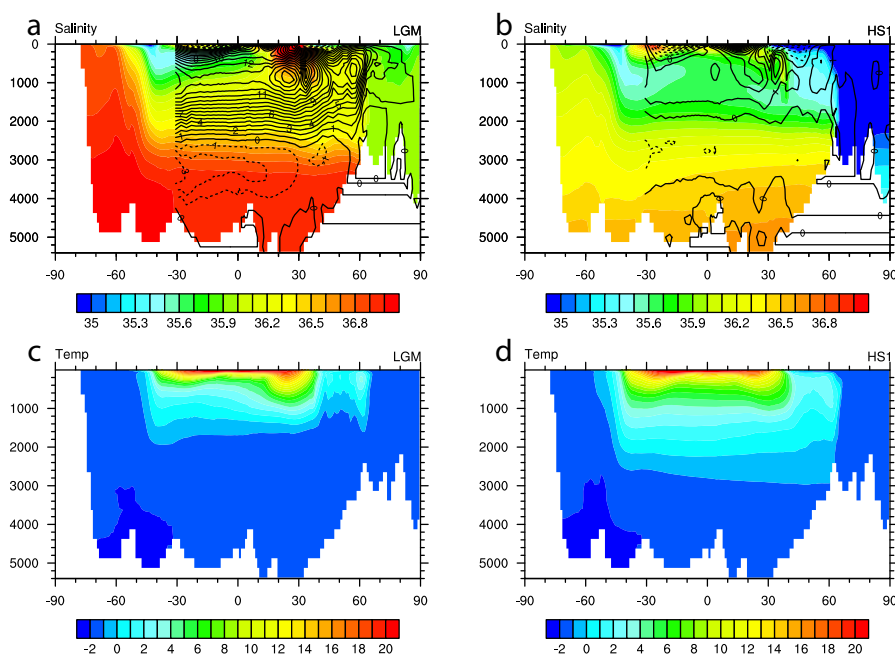


Figure 4.1.1 AMOC during LGM (a contour) and HS1(b contour) in CTRACE. Atlantic zonal mean salinity during LGM (a color) and HS1 (b color). Atlantic zonal mean temperature during LGM (c) and HS1 (d).

4.2 Deglacial Evolution of $\delta^{18}\text{O}_c$ Gradient Over Florida Straits and AMOC

In this chapter, two cores located on either side of the Florida Current at about 500m are analyzed to study whether the $\delta^{18}\text{O}_c$ gradient represents the AMOC evolution. The $\delta^{18}\text{O}_c$ gradient between these two cores is suggested to represent the density gradient, which can be used to reconstruct the flow strength of the Florida current (Lynch-Stieglitz et al., 2014). But the Florida current can also be influenced by wind-driven flow. CTRACE results suggest that $\delta^{18}\text{O}_c$ gradient, density gradient and flow strength all follow the change of AMOC and the strength of the Florida current is controlled by AMOC instead of the wind.

The evolution of AMOC in CTRACE reproduces the results in TraCE21K results (He, 2011; Liu et al., 2009). $^{231}\text{Pa}/^{230}\text{Th}$ from Bermuda Rise site (OCE326-GGC5 (33°42'N, 57°35'W, 4.55km)) in CTRACE is in good agreement with observation (McManus et al., 2004) from LGM to BA. From BA to YD, although the absolute value of $^{231}\text{Pa}/^{230}\text{Th}$ in the model is higher than the observation, the relative change is still the same. This suggests that the circulation simulated in CTRACE is a good representation of the actual ocean circulation during the last deglaciation.

The $\delta^{18}\text{O}$ in calcium carbonate ($\delta^{18}\text{O}_c$) in the model can be calculated from $\delta^{18}\text{O}$ in the water ($\delta^{18}\text{O}_w$) and temperature using
$$\delta^{18}\text{O}_c = \delta^{18}\text{O}_w - 0.27 + 0.0011t^2 - 0.245t + 3.58$$
 (Marchitto et al., 2014). $\delta^{18}\text{O}_c$ in the model can be decomposed to the water part ($\delta^{18}\text{O}_w$) and the temperature part ($\delta^{18}\text{O}_T$). The temperature part is $0.0011t^2 - 0.245t$. The $\delta^{18}\text{O}_c$ evolutions from two cores located on either side of the Florida current in CTRACE show a similar decrease as observations from the LGM to the HS1 (Figure 4.2.1 b), which is mainly caused by $\delta^{18}\text{O}_w$ (Figure 4.2.1 c). During HS1, melt water with highly depleted $\delta^{18}\text{O}$ ($\sim -30\text{‰}$) (Sima et al., 2006) is applied to the North Atlantic, causing this decrease of $\delta^{18}\text{O}_w$ (volume effect).

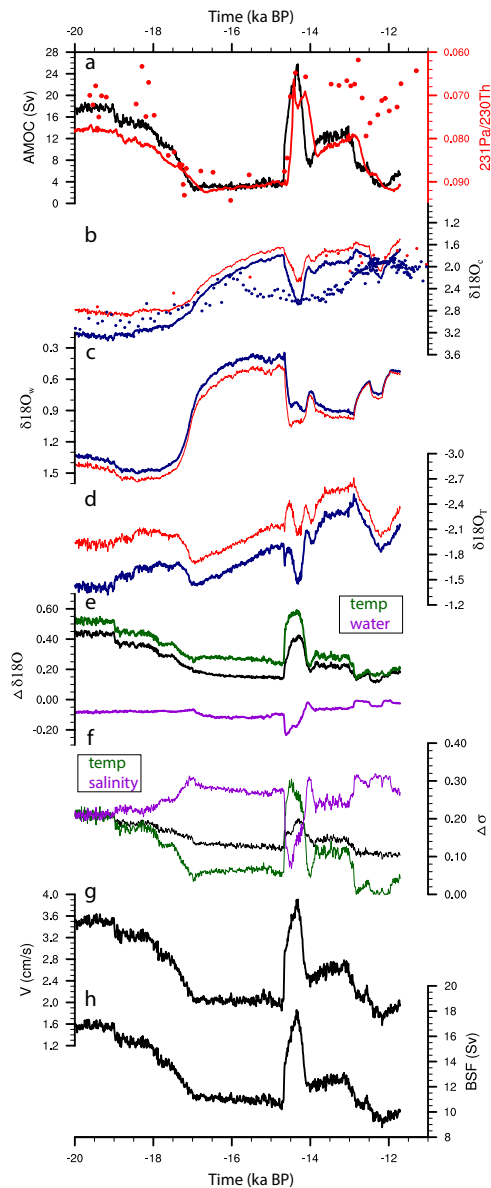


Figure 4.2.1 Time evolutions in the Florida Straits in CTRACE. (a) AMOC strength (black) and observational (red dot) (McManus et al., 2004) and model (red curve) $^{231}\text{Pa}/^{230}\text{Th}$ from site OCE326-GGC5 (33°42'N, 57°35'W, 4.55km). (b) $\delta^{18}\text{O}_c$ evolution from two cores located on either side of the Florida Current (blue for KNR166-2-26JPC; red for KNR166-2-73GC). Dots are observations (Lynch-Stieglitz et al., 2014) and curves are model results. (c) $\delta^{18}\text{O}_w$ evolution from the two cores in (b). (d) $\delta^{18}\text{O}_T$ evolution from the two cores in (b). (e) The gradient (west - east) of $\delta^{18}\text{O}$ between the two cores: black for the $\delta^{18}\text{O}_c$, green for $\delta^{18}\text{O}_T$ and purple for $\delta^{18}\text{O}_w$. (f) The density gradient (west - east) between the two cores (black), the density gradient caused

by the salinity gradient (purple) and the density gradient caused by the temperature gradient (green). (g) Meridional velocity at 530m in the Florida Straits. (h) The average barotropic streamfunction (BSF) at these two cores.

The deglacial evolution of $\delta^{18}\text{O}_c$ gradient between the two cores is a good representation of the zonal density gradient evolution across the Florida Straits. The $\delta^{18}\text{O}_c$ gradient and the density gradient all experience decrease during HS1 and YD and increase during BA. The reduced $\delta^{18}\text{O}_c$ gradient during HS1 and YD is consistent with observations (Lynch-Stieglitz et al., 2014). Unlike the $\delta^{18}\text{O}_c$, the evolution of which is dominated by $\delta^{18}\text{O}_w$, the evolution of $\delta^{18}\text{O}_c$ gradient between the two cores is dominated by the change of temperature gradient (Figure 4.2.1 e). Salinity evolution can also be decomposed into the temperature part and salinity part. The density change caused by the temperature is calculated using the deglacial temperature evolution with the salinity fixed at the LGM value and vice versa for the salinity part. Similar to $\delta^{18}\text{O}_c$ gradient, the change of zonal density gradient across the Florida Straits is also dominated by the temperature gradient change (Figure 4.2.1 f). Since both of the deglacial $\delta^{18}\text{O}_c$ gradient and the density gradient are dominated by the temperature gradient, the $\delta^{18}\text{O}_c$ gradient covaries with the density gradient.

By thermal wind balance, reduced zonal density gradient during HS1 and YD suggests reduced meridional flow strength, which is also confirmed in the model results. The evolution of the Florida currents experiences the same decrease and increase during the deglaciation as the density gradient (Figure 4.2.1 g and h). The meridional velocity at 530 m measures the flow speed, which shows similar changes as AMOC evolution in CTRACE, suggesting that the Florida current strength evolves with AMOC in the model.

However, the strength of Florida current reflects both of the western part of the wind-driven subtropical gyre and the northward surface return flow of AMOC, which are hard to separate in paleo reconstructions. AMOC consists an upper limb which transport water in upper 1,000m northward, supplying the formation of NADW and a lower limb which transport water southward through western boundary current (Figure 4.2.2). Therefore, Florida current, as part of the upper limb return flow of AMOC, changes with

AMOC evolution. However, it is also possible that wind stress also changes during the deglaciation and influences the Florida current strength.

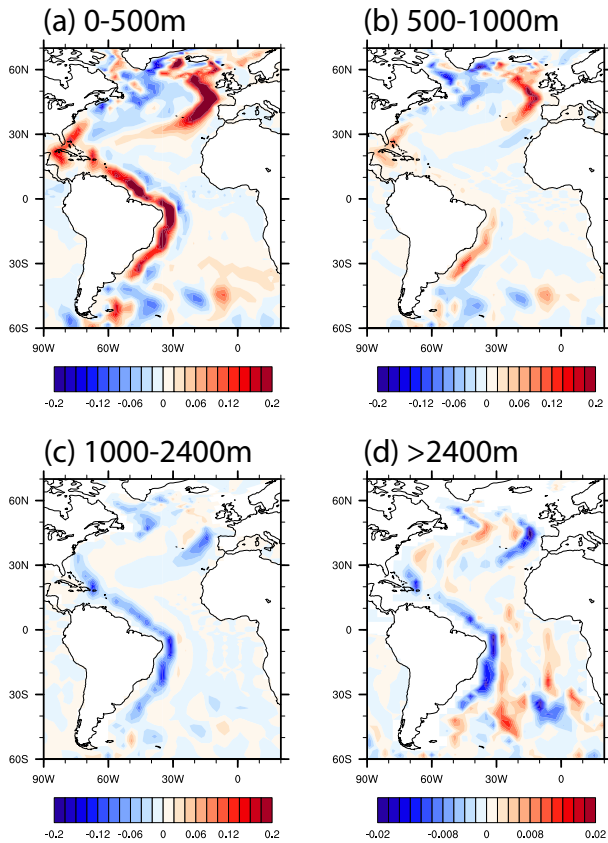


Figure 4.2.2 Regression coefficient of vertically averaged meridional velocity evolution on AMOC: (a) 0-500 m; (b) 500-1,000 m; (c) 1,000-2,400 m and (d) deeper than 2,400m.

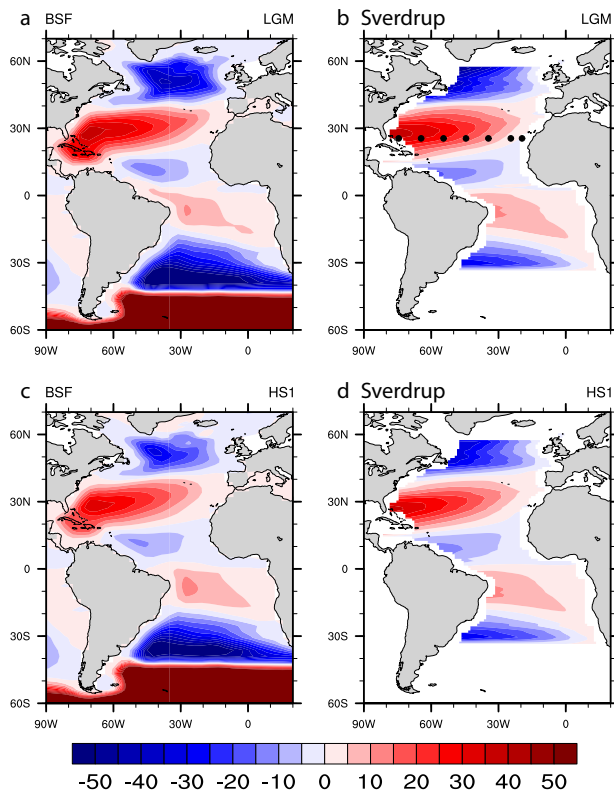


Figure 4.2.3 The barotropic streamfunction during LGM (a) and HS1 (c). The Sverdrup transport calculated from surface wind stress (b) and (d).

Modeling results from CTRACE suggest that in the western boundary, the flow strength of the Florida current is dominated by AMOC evolution instead of surface wind stress. Barotropic streamfunction (BSF) measures the vertically integrated meridional transport. Sverdrup transport can be calculated by integrating the Sverdrup relation ($\beta V = \frac{curl \tau}{\rho_0}$) from the eastern boundary, assuming no bottom topography, which can be used to represent the strength of wind-driven circulation. The BSF in the Florida Straits varies with AMOC (Figure 4.2.1 h) but the Sverdrup transport does not. Theoretically, in the stratified fluid, if there is no bottom topography, the BSF and Sverdrup transport is the same. But with bottom velocity, BSF no longer equals to the Sverdrup transport. This is confirmed in the CTRACE simulation. The pattern of BSF and Sverdrup transport show the similar wind-driven subtropical and subpolar gyre during LGM and HS1 (Figure 4.2.3). In the interior of the North Atlantic, where the horizontal gradient of bottom

topography is low (Figure 4.2.4 a), BSF is similar to the Sverdrup transport (Figure 4.2.5 a-f) and the correlation between BSF and Sverdrup in CTRACE is quite high (Figure 4.2.4 a). In the western boundary, with continental slope, BSF is different from Sverdrup transport (Figure 4.2.5 g) and the correlation between BSF and Sverdrup transport is small (Figure 4.2.4 a). The evolution of BSF in the Florida current follows AMOC during the deglaciation but the Sverdrup transport shows almost no change between LGM and HS1 (Figure 4.2.5 g), suggesting that the deglacial flow strength of Florida currents is dominated by AMOC. Previous theories and modeling studies suggest that with bottom topography and buoyancy flux in the North Atlantic, the transport in the western boundary is much larger than that predicted by the Sverdrup transport (Holland, 1972) due to the joint effect of baroclinicity and bottom relief (JEBAR) (Sarkisyan and Ivanov, 1971). In CTRACE, the BSF is highly correlated with AMOC in the western boundary of the North Atlantic, consistent with the JEBAR. Therefore, flow strength of the Florida currents is a good indicator of AMOC strength.

Results from CTRACE simulation suggest that $\delta^{18}\text{O}_c$ gradient across the Florida Straits can be used to reconstruct AMOC evolution. $\delta^{18}\text{O}_c$ gradient covaries with density gradient and represents the strength of Florida current, which is controlled by AMOC evolution.

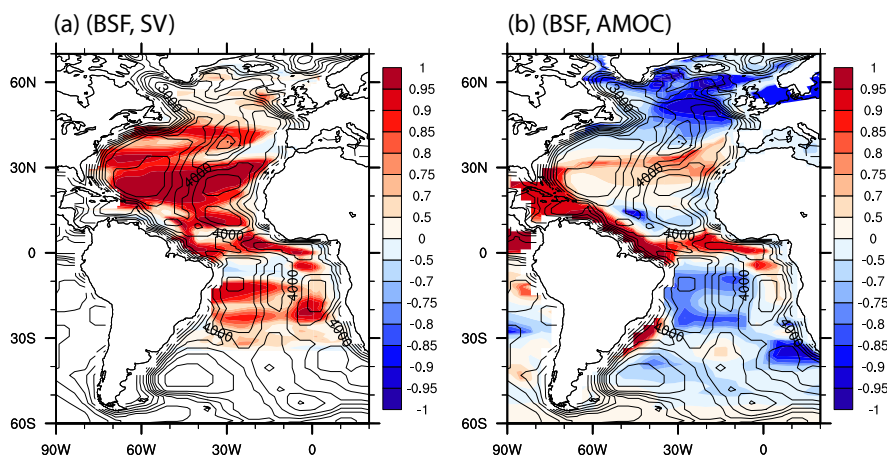


Figure 4.2.4 (a) Correlation between the barotropic streamfunction (BSF) and AMOC. (b) Correlation between the barotropic streamfunction and Sverdrup transport. Topography is overlaid as black contours.

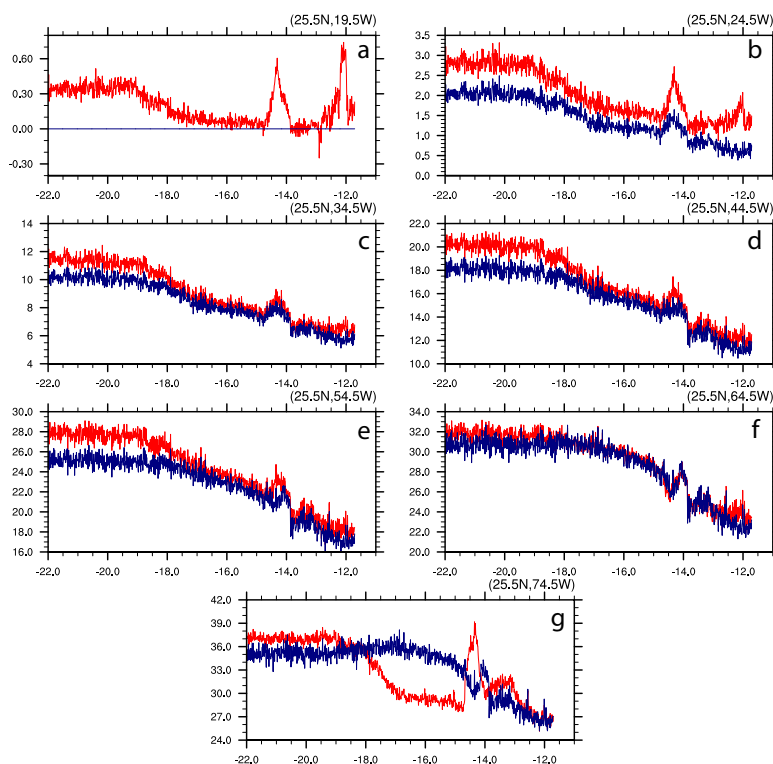


Figure 4.2.5 Evolutions of BSF (red) and Sverdrup transport (navy) from the locations indicated by the dots on Figure 4.2.3b.

4.3 Glacial and Deglacial Evolution of $\delta^{18}\text{O}_c$ Gradient across the Atlantic at 30°S

In the Atlantic, the northward flow above 1,000m and southward flow below this depth requires the density in the eastern margin in the South Atlantic to be higher than the western margin. However, if the density and $\delta^{18}\text{O}_c$ relationship during LGM is the same as present day, the $\delta^{18}\text{O}_c$ gradient between the Brazil margin and African margin suggests higher density in the western margin than the eastern margin in the upper 1,000m (Lynch-Stieglitz et al., 2006), which is contradictory to the shallower and active AMOC during LGM (Boyle and Keigwin, 1987; Curry and Oppo, 2005; Marchitto and Broecker, 2006). Model simulation using iPOP2 suggests shallower and slightly stronger AMOC during LGM than present day (17.6 Sv during and 15.8 Sv during present day). The African margin is denser than the Brazil margin during both present day and LGM in the

upper 1,000m, consistent with the physical circulation in the model (Figure 4.3.1). The $\delta^{18}\text{O}_c$ in the model cannot simulate the larger $\delta^{18}\text{O}_c$ in the western margin than the eastern in the LGM observations. $\delta^{18}\text{O}_c$ profile is similar to the density profile at the 30°S in the South Atlantic in the upper 1,000m during both present day and LGM (Figure 4.3.1).

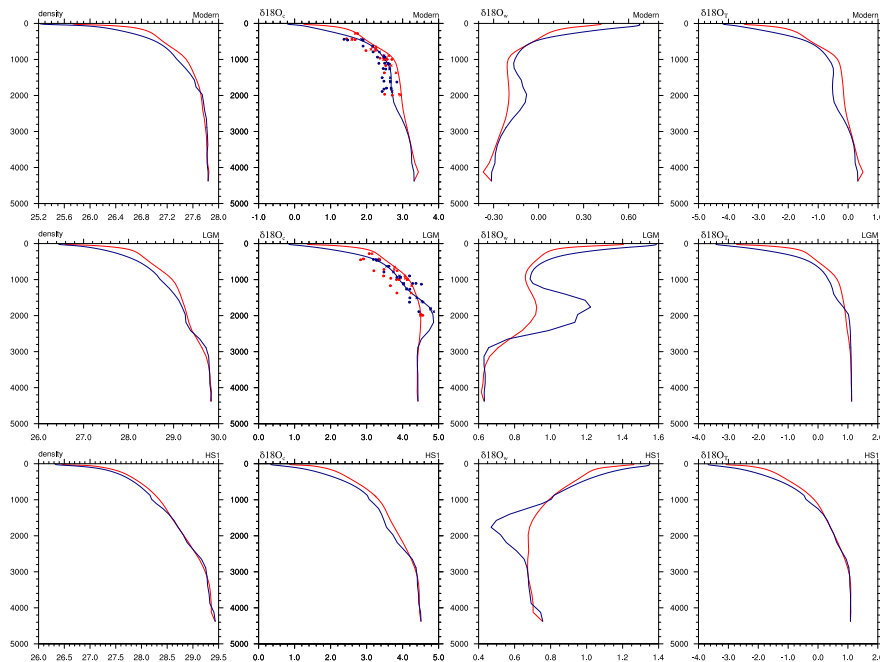


Figure 4.3.1 Density, $\delta^{18}\text{O}_c$, $\delta^{18}\text{O}_w$ and $\delta^{18}\text{O}_T$ profiles at the eastern (red) and western (navy) margin at 30°S in the Atlantic during modern climate, LGM and HS1 in the model. $\delta^{18}\text{O}_c$ observations are attached as colored dots. $\delta^{18}\text{O}_c$ values at observation sites are attached as colored cross.

However, during LGM, the model simulates the higher $\delta^{18}\text{O}_c$ in the western Atlantic than the eastern Atlantic from 1,500m to 2,600m, which is caused by the high $\delta^{18}\text{O}_w$ in the NADW in the western margin (Figure 4.3.1 and Figure 4.3.2). NADW forming in the North Atlantic features high $\delta^{18}\text{O}_w$, low ϵ_{Nd} , high $\delta^{13}\text{C}$ and low radiocarbon age. In the western margin at 30°S, NADW signals from these different tracers are consistent with maximum southward meridional velocity below 1,000m, suggesting that the high $\delta^{18}\text{O}_w$ tongue at about 2,000m in the western Atlantic during LGM is caused by the southward flowing NADW (Figure 4.3.3). The vertical distribution

of these different tracers is consistent with the shallower AMOC during LGM than the present in the model (Figure 4.3.3).

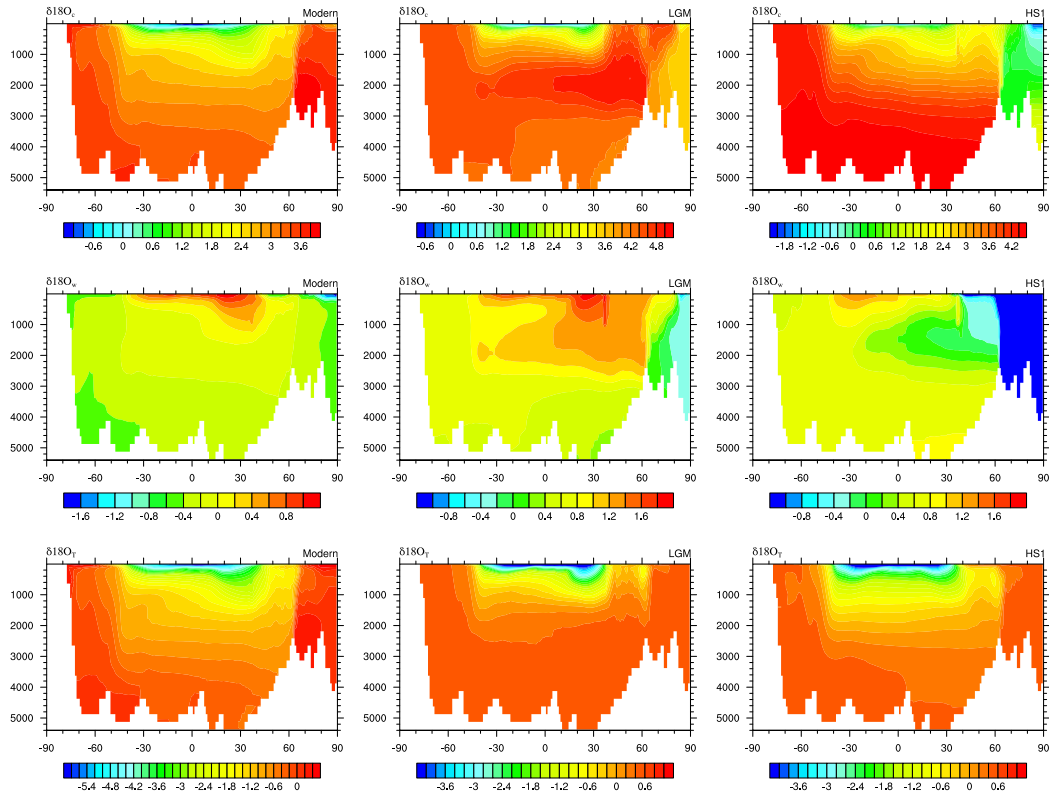


Figure 4.3.2 Atlantic zonal mean $\delta^{18}O_c$, $\delta^{18}O_w$ and $\delta^{18}O_T$ during modern climate, LGM and HS1.

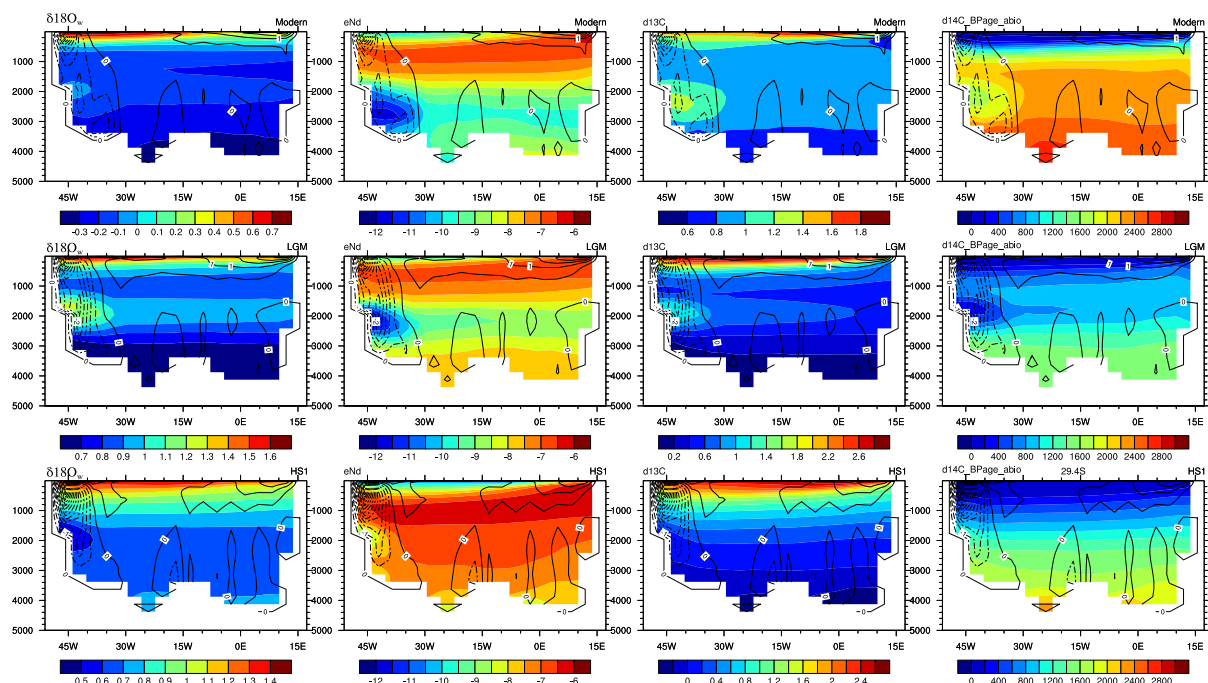


Figure 4.3.3 Zonal section at 30°S of $\delta^{18}\text{O}_w$, ϵ_{Nd} , $\delta^{13}\text{C}$ and radiocarbon age during present day, LGM and HS1. Black contours are the meridional velocity.

Since the shallower NADW during LGM is well established (Boyle and Keigwin, 1987; Curry and Oppo, 2005; Marchitto and Broecker, 2006) and model $\delta^{18}\text{O}_c$ is higher in the western margin than the eastern margin in the NADW depth range, can the model data mismatch caused by the bias in the model, specifically, the NADW is not shallow enough and deeper than observations? Model data comparisons using other tracers suggests that the NADW depth during LGM in the model is in reasonable agreement with observations. The distribution of ϵ_{Nd} during LGM agrees with observations (Howe et al., 2016b) (Figure 4.3.4 a and b). Compared with present day, LGM in the model has the shallower NADW cell and stronger AABW cell (Figure 4.3.4 a and b). During LGM, ϵ_{Nd} in the Atlantic experiences major increase below 2,500m in both observation and model simulation (Figure 4.3.4 c). This increase of ϵ_{Nd} is caused by the upward shifting of NADW and the increased strength of AABW cell. The vertical distribution of $^{231}\text{Pa}/^{230}\text{Th}$ in the North Atlantic in the model shows a similar pattern to the observations (Lippold et al., 2012b). The low $^{231}\text{Pa}/^{230}\text{Th}$ tongue at about 3,000m during present day in the average

$^{231}\text{Pa}/^{230}\text{Th}$ profile in the North Atlantic is caused by the southward NADW, which transports ^{231}Pa out of the North Atlantic (Chapter 2.2). During LGM, this NADW is shallower by about 800m, which is consistent with observations (Figure 4.3.5 a). The upward shift of NADW during LGM leads to more southward transport of ^{231}Pa to the Southern Ocean in the upper ocean and $^{231}\text{Pa}/^{230}\text{Th}$ above 2000m experiences a negative shift from present day to LGM. Below 2500m, $^{231}\text{Pa}/^{230}\text{Th}$ experiences a positive change from present day to LGM which is caused by less ^{231}Pa is transported out of North Atlantic due to the upward shifting of NADW in the deep ocean and the increase input ^{231}Pa from the South Ocean by the increased AABW cell in the abyssal (Figure 4.3.5 b). In addition, $\delta^{13}\text{C}$ in the western Atlantic also shows good agreement with observations (Hesse et al., 2011) (Figure 4.3.6 b). The change of the vertical distribution of $\delta^{13}\text{C}$ is well simulated with reduced $\delta^{13}\text{C}$ under 2,000m, consistent with observations. The high $\delta^{13}\text{C}$ tongue in the western Atlantic in the model is also at a similar depth to the observation. Therefore, the vertical distribution of ϵ_{Nd} , $^{231}\text{Pa}/^{230}\text{Th}$ and $\delta^{13}\text{C}$ all suggests that the shallower NADW during LGM compared with present day in the model is in the right depth as in observations, which rules out the possibility that the larger $\delta^{18}\text{O}$ in the western margin than the eastern margin is caused by the influence of the $\delta^{18}\text{O}$ enriched NADW water.

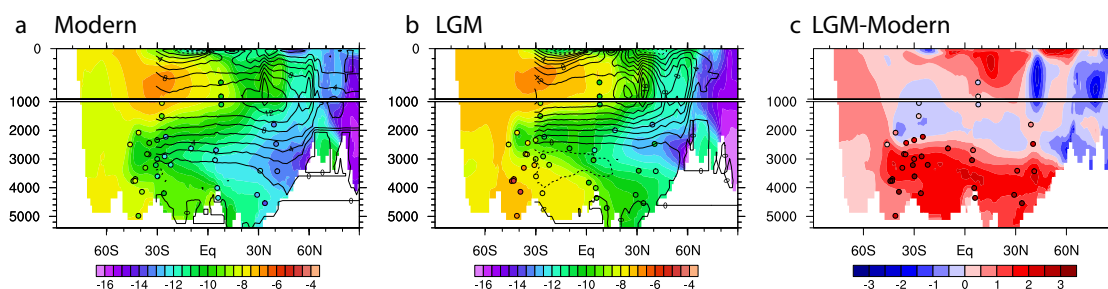


Figure 4.3.4 Atlantic zonal mean ϵ_{Nd} during present day and LGM and the difference between LGM and present day in the model. Observations (Howe et al., 2016a) are overlaid as circles. Black contours are the Atlantic meridional overturning streamfunction.

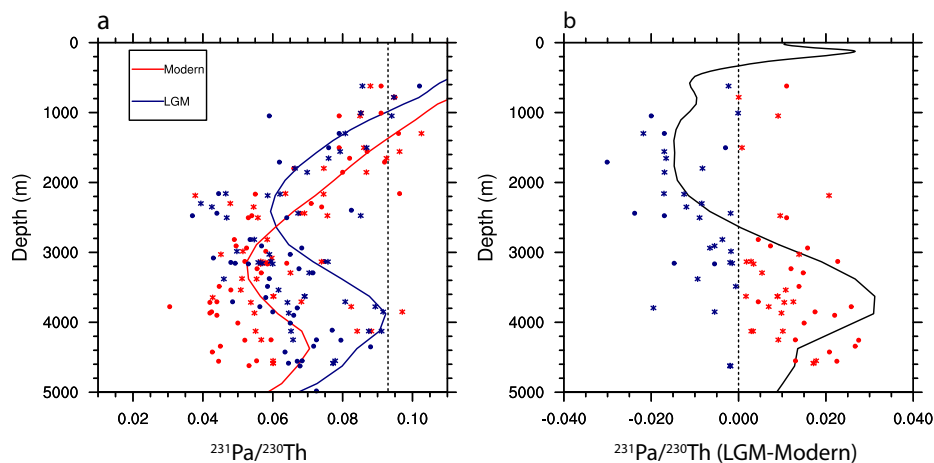


Figure 4.3.5 (a) $^{231}\text{Pa}/^{230}\text{Th}$ during present day (red) and LGM (navy): the average from 20°N - 60°N in the North Atlantic (curve) from model simulation; observations in the North Atlantic (dots) (Lippold et al., 2012b); model $^{231}\text{Pa}/^{230}\text{Th}$ at observational sites (cross). (b) The difference of $^{231}\text{Pa}/^{230}\text{Th}$ between LGM and present day: the average from 20°N - 60°N in the North Atlantic (curve) from model simulation; observations (dots) and model values at observational sites (cross) (red for positive values and navy for negative values).

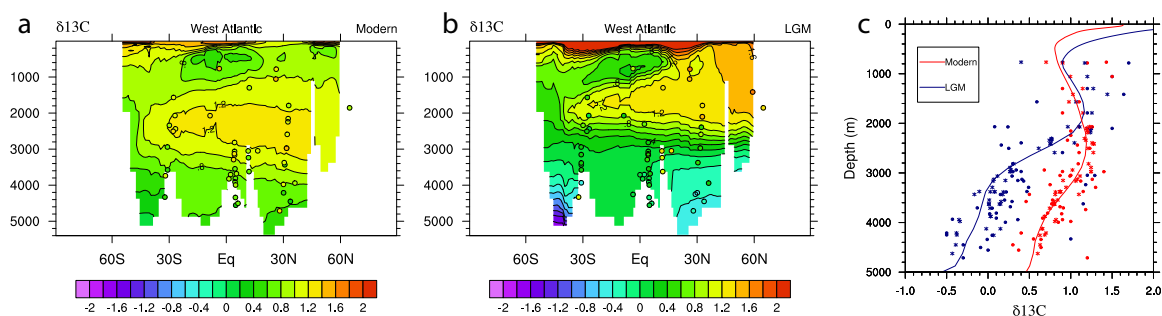


Figure 4.3.6 $\delta^{13}\text{C}$ in the western Atlantic during present day (a) and LGM (b). Observations (Hesse et al., 2011) are overlaid as circles. (c) $\delta^{13}\text{C}$ in the North Atlantic during LGM (red) and present day (navy): average vertical profile of $\delta^{13}\text{C}$ in the western Atlantic (curve); observations (dot) (Hesse et al., 2011); model values at observational sites (cross).

Gebbie and Huybers, (2006) suggests that it is possible that the $\delta^{18}\text{O}_c$ contrast between the eastern and western South Atlantic does not represent the density gradient because of different water mass properties (temperature, salinity, $\delta^{18}\text{O}_w$). Although the model simulation failed to simulate this decoupling between $\delta^{18}\text{O}_c$ gradient and density gradient during LGM, our model does simulate this decoupling through the deglaciation. During HS1, AMOC is collapsed in CTRACE simulation and the density contrast between the African and Brazil margin is greatly reduced in the upper 1,000m (Figure

4.3.1). However, the $\delta^{18}\text{O}_c$ difference between the African and Brazil margin during HS1 is of comparable magnitude with LGM (Figure 4.3.1). Evolution of the $\delta^{18}\text{O}_c$ gradient at 30°S at 530m between the African and Brazil margin shows that the $\delta^{18}\text{O}_c$ gradient is dominated by $\delta^{18}\text{O}_T$ gradient, which shows an initial decrease at 17.5ka but increases back to LGM level at the end of HS1 (Figure 4.3.7 d). However, the evolution of density gradient highly correlates with AMOC evolution during the last deglaciation and the deglacial change of the density gradient is dominated by the salinity gradient instead of the temperature gradient (Figure 4.3.7 e). During HS1, at 530m, the western and eastern margin at 30°S in the South Atlantic experience similar warming and similar increase in $\delta^{18}\text{O}_w$, compared with LGM (Figure 4.3.8). Therefore, $\delta^{18}\text{O}_c$ gradient during HS1 does not change much. However, the salinity in the western South Atlantic increases a lot during HS1. AAIW is suggested to be deeper during HS1 than LGM as has been discussed in Chapter 3. During LGM, level of 530m is influenced by AAIW and the distribution of salinity clearly shows that fresh AAIW circulating in the subtropical gyre in the South Atlantic and penetrating further northward across the equator in the western boundary. However, during HS1, the core of AAIW is deeper than 530m and the salinity distribution at 530m only shows a narrow band of fresh AAIW at 40°S and there is no fresh AAIW in the subtropical gyre at 530m. Therefore, the salinity in the western Atlantic at 30°S increases a lot during HS1, which dominates the change of density gradient between the western and eastern South Atlantic from LGM to HS1. The deglacial evolution of the density and $\delta^{18}\text{O}_c$ across the Atlantic at 30°S suggests that it is possible that the $\delta^{18}\text{O}_c$ gradient can be decoupled from the density gradient and water mass properties should be better constrained before using $\delta^{18}\text{O}_c$ to reconstruct density and in turn, the AMOC strength.

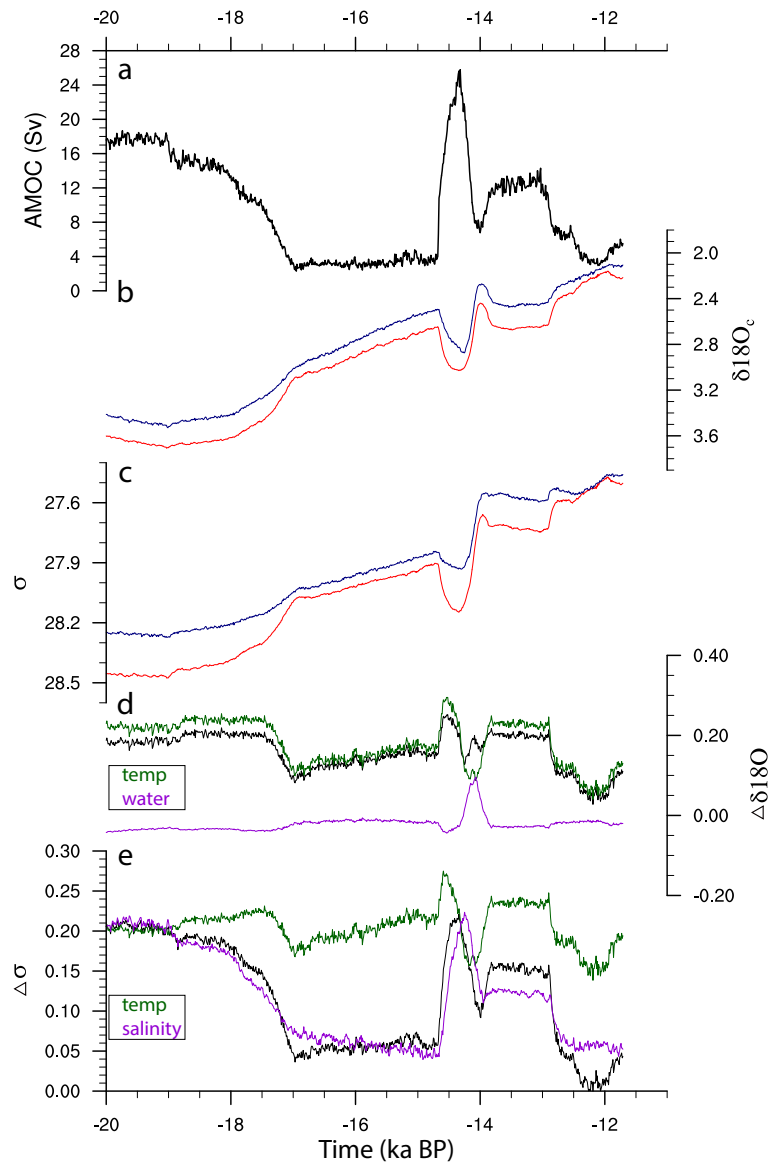


Figure 4.3.7 Time evolutions at 530 m at 30°S in CTRACE. (a) AMOC strength. (b) $\delta^{18}\text{O}_c$ evolution from the western (red) and eastern (navy) margin. (c) potential density evolution from the western (red) and eastern (navy) margin. (d) The gradient (west - east) of $\delta^{18}\text{O}$ between the two cores: black for the $\delta^{18}\text{O}_c$, green for $\delta^{18}\text{O}_T$ and purple for $\delta^{18}\text{O}_w$. (e) The potential density gradient (west - east) (black), the density gradient caused by the salinity gradient (purple) and the density gradient caused by the temperature gradient (green).

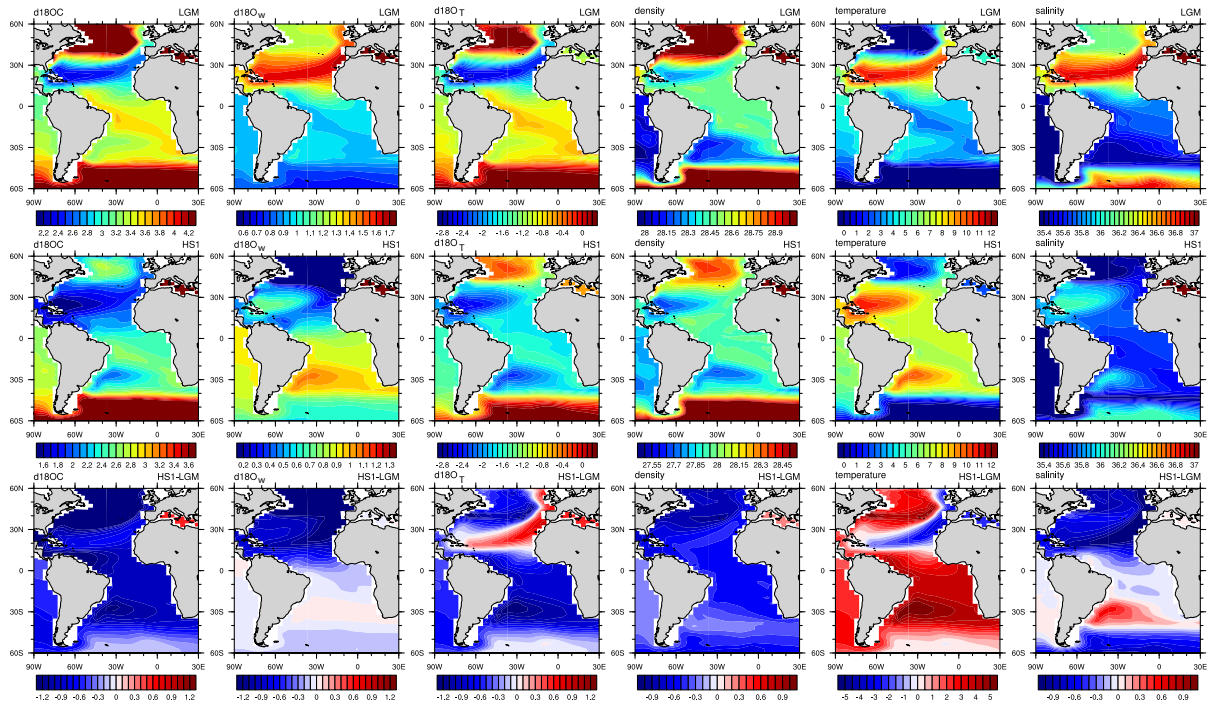


Figure 4.3.8 Distribution of $\delta^{18}O_C$, $\delta^{18}O_W$ and $\delta^{18}O_T$, potential density, temperature and salinity at 530m during LGM, HS1 and the difference between HS1 and LGM.

4.4 How Well in General Can $\delta^{18}O_C$ Gradient Across the Basin and the West Boundary in the Atlantic Represent AMOC Strength?

Since $\delta^{18}O_C$ contrast across the western boundary in the Florida Straits highly correlates with AMOC evolution in CTRACE but $\delta^{18}O_C$ contrast across the Atlantic basin does not, in this chapter, the relationship between density gradient, $\delta^{18}O_C$ gradient across both the western boundary and the Atlantic basin and AMOC at different latitude are examined. The tropical region is neglected in the analysis because of f is small.

In the extratropical region, the basin-wide density gradient at 530m is highly correlated with AMOC in both North Atlantic and South Atlantic (Figure 4.4.1 b navy), following the thermal wind balance. Overall, the density gradient across the western boundary at 530m also represents well the western boundary current strength, which is

correlated with AMOC strength. Therefore, the density gradient across the western boundary correlates with AMOC (Figure 4.4.1 b red).

Unlike the basin-wide density gradient, the basin-wide $\delta^{18}\text{O}_c$ gradient at 530m shows high correlation with AMOC in the North Atlantic but small correlation with AMOC in the South Atlantic (Figure 4.4.1 c navy), which is caused by the lower correlation between basin-wide $\delta^{18}\text{O}_c$ gradient and density gradient in the South Atlantic than the North Atlantic (Figure 4.4.1 d navy). In the South Atlantic, the basin-wide $\delta^{18}\text{O}_c$ gradient at 530m decouples from the density gradient because of the AAIW change during the deglaciation have a much larger influence on the density than $\delta^{18}\text{O}_w$ in the western Atlantic. However, in the western boundary of the South Atlantic, the density gradient and the $\delta^{18}\text{O}_c$ gradient are highly correlated. This is because in the western boundary, the water mass is with more or less uniform properties (salinity and $\delta^{18}\text{O}_w$) and both of the density gradient and the $\delta^{18}\text{O}_c$ gradient are dominated by the temperature gradient. Therefore, in general, using the $\delta^{18}\text{O}_c$ gradient to reconstruct density gradient is more reliable in the western boundary than the whole basin.

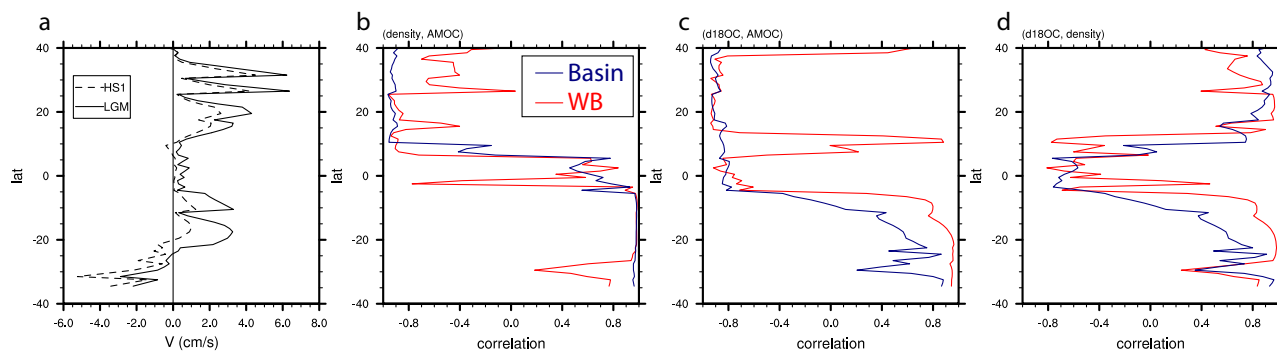


Figure 4.4.1 (a) Meridional velocity at 530m in the western boundary in the Atlantic during LGM (solid) and HS1 (dash). (b) The correlation between AMOC and the density gradient across the western boundary (red) and the Atlantic basin (navy) at 530m. (c) The correlation between AMOC and the $\delta^{18}\text{O}_c$ gradient across the western boundary (red) and the Atlantic basin (navy) at 530m. (d) The correlation between density gradient and $\delta^{18}\text{O}_c$ gradient across the western boundary (red) and the Atlantic basin (navy) at 530m. All the gradients are eastern value minus western value.

4.5 Conclusion

$\delta^{18}\text{O}_c$ is a useful proxy to reconstruct past density and in turn AMOC strength. Results from the CTRACE simulation suggests that $\delta^{18}\text{O}_c$ gradient in the Florida Straits reflects the density gradient and therefore the strength of the Florida current. The deglacial variation in the Florida current is dominated by the AMOC change instead of the surface wind stress. Therefore, the $\delta^{18}\text{O}_c$ gradient in the Florida Straits can be used to reconstruct AMOC during the last deglaciation. However, in the South Atlantic, the basin-wide $\delta^{18}\text{O}_c$ gradient can be different from density gradient during the last deglaciation because of the influence of AAIW. Although the model cannot simulate the different east-west contrast of $\delta^{18}\text{O}_c$ between LGM and present day in the observation, the example of $\delta^{18}\text{O}_c$ during the last deglaciation provides a possibility that $\delta^{18}\text{O}_c$ contrast across the basin cannot represent the density contrast. Therefore, better constraints on the past water mass property are required to use $\delta^{18}\text{O}_c$ to reconstruct density. In general, density contrast can be more correctly reconstructed in the western boundary than across the whole basin.

5. Conclusions and Future Perspectives

5.1 Conclusions

The major findings of my PhD study are:

(1) *iPOP2 development and validation*. In addition to the water isotopes and carbon isotopes in POP2, this study develops the Nd module and ^{231}Pa and ^{230}Th module in POP2, which facilitates POP2 with the most widely used proxies in paleoceanography. Under present day forcing, model Nd concentration, ϵ_{Nd} , water column ^{231}Pa and ^{230}Th activity and sediment $^{231}\text{Pa}/^{230}\text{Th}$ activity ratio are in good agreement with observations. ϵ_{Nd} in the model is able to trace different water masses. Sediment $^{231}\text{Pa}/^{230}\text{Th}$ activity ratio in the North Atlantic in the model responds to the change of AMOC as it should be. In addition, with p-fixed and p-coupled versions of $^{231}\text{Pa}/^{230}\text{Th}$, iPOP2 can separate the circulation effect and the particle flux effect on sediment $^{231}\text{Pa}/^{230}\text{Th}$.

(2) *Deglacial northward penetration of AAIW in the Atlantic*. The northward penetration of AAIW is determined predominantly by the AMOC intensity remotely, with a stronger AMOC enhancing AAIW northward penetration. In addition, AAIW sinks to greater depth and dominates a wider water depth range in response to reduced stratification during reduced AMOC. AAIW is thus a critical part of the return flow of the southward flowing NADW and, in turn, the global thermohaline circulation, and therefore can contribute significantly to global climate change. Also, monitoring changes of AAIW can contribute to our understanding of climate changes in the past and future projections. In addition, the controversial ϵ_{Nd} reconstructions from tropical Atlantic is caused by the core locations and depths. With the AAIW depth changing in the past, depth influenced by AAIW in present day, such as the Demerara Rise site, may not be influenced by AAIW during the last deglaciation. Also, the radiogenic ϵ_{Nd} water from the Gulf of Mexico and the Caribbean Sea is important in regulating ϵ_{Nd} at intermediate depth in tropical North Atlantic, which complicates the interpretation of ϵ_{Nd} reconstruction in the tropical North Atlantic and should be taken into consideration in interpreting ϵ_{Nd} reconstructions from the tropical Atlantic.

(3) *Using $\delta^{18}\text{O}_c$ gradient to reconstruct AMOC strength.* $\delta^{18}\text{O}_c$ contrast can represent the density gradient quite well in the upper ocean across the western boundary during the last deglaciation, but the $\delta^{18}\text{O}_c$ density relationship across the Atlantic basin is interrupted by the water mass property change during the deglaciation in the South Atlantic, suggesting that the $\delta^{18}\text{O}_c$ contrast during the LGM in the observation may be caused by different water mass property in the eastern and western margin. Therefore, water mass property needs to be better constrained before using basin-wide $\delta^{18}\text{O}_c$ gradient to reconstruct density gradient. Nevertheless, $\delta^{18}\text{O}_c$ is a useful proxy to reconstruct AMOC strength, as a complement dynamic tracer of $^{231}\text{Pa}/^{230}\text{Th}$. Lastly, the CTRACE simulation also suggests that the Florida current strength is controlled by AMOC strength during the last deglaciation and is less influenced by the surface wind stress.

5.2 Future Perspectives

CTRACE simulation provides a potentially useful tool to improve the understanding of the mechanisms underlying the ocean circulation and tracer evolution during the deglaciation. CTRACE simulation is the first deglacial simulation with ocean biogeochemical module and different tracers including water isotope, carbon isotope, ϵ_{Nd} and $^{231}\text{Pa}/^{230}\text{Th}$. This allow for a direct model data comparison across different proxies to study deglacial ocean circulation and to study the tracer circulation relationship in the model itself. The deglacial AAIW and using $\delta^{18}\text{O}_c$ to reconstruct past AMOC in this study show two good examples of this approach.

In the future, I will continue working on using CTRACE to study deglacial ocean circulation. For example, a record of $^{231}\text{Pa}/^{230}\text{Th}$ from Bermuda Rise suggests a very weak AMOC during HS1 (McManus et al., 2004). However, benthic $\delta^{13}\text{C}$ and $\delta^{18}\text{O}$ from upper 2,000m in the Northeast Atlantic experience a large decrease during HS1 (Oppo et al., 2015). $\Delta^{14}\text{C}$ reconstructions from the upper ocean in the North Atlantic show a large positive change in late HS1 (Chen et al., 2015). If ocean circulation is nearly collapsed during HS1, how dose these water mass change in the upper ocean during HS1. In addition, the $^{231}\text{Pa}/^{230}\text{Th}$ compilation from Bradtmiller et al., (2014) suggests that

although transport is reduced at all depth during HS1, shallower NADW during the LGM is weakened but not cessation as previously suggested. CTRACE simulation can be used to study the AMOC strength and geometry during HS1 using different tracers.

Another interesting question is a phase difference in sediment $^{231}\text{Pa}/^{230}\text{Th}$ reconstruction between two cores located in the eastern North Atlantic (Gherardi et al., 2005) and in the western North Atlantic (McManus et al., 2004). Both cores show an increased value during HS1, but the change of the eastern one lags the change of the western one by approximately 1,000 years and is with a shorter duration. It is suggested that this phase difference is caused by the difference in circulation dynamics of the two basins. The western site is near the deep convection in South Labrador Sea and therefore is more sensitive to the change of the Laurentide ice sheet, while the eastern site is more sensitive to deep convection in the east, therefore, more sensitive to the change of the European ice sheets. The time difference of the change in the deep convection from the west and the east can lead to the phase difference in the sediment $^{231}\text{Pa}/^{230}\text{Th}$ reconstruction from the two cores (Gherardi et al., 2005). It is also possible the phase difference comes from the different depth of these two cores: the east site is 1,400 m shallower than the west core. With both $^{231}\text{Pa}/^{230}\text{Th}$ and ϵ_{Nd} in the ocean model, why there is a phase difference in the two cores from the west and east can be explored, which may better constrain the deep convection change during the HS1.

Appendix: Vertical differentiation scheme in calculating the reversible scavenging term

In the calculation of $w_S \frac{\partial A_p}{\partial z}$, I consider downward as positive (w_S is positive). $w_S \frac{\partial A_p}{\partial z}$ can be calculated by Eq.(A1). Detailed notations are illustrated in Fig.S1.

$$w_S \frac{\partial A_p}{\partial z}(k) = w_S \frac{A_p u(k+1) - A_p u(k)}{dz(k)} \quad (\text{A1})$$

$A_p u$, which is the particulate isotope activity at the upper bound of the grid box, can be calculated by Eq. (A2). For the surface layer ($A_p u(1)$), we assume the particulate isotope activity at surface is 0, which is true as there is no surface flux for calcite, opal and POC. For layers between the surface and the bottom, we use liner interpolation. For the bottom layer, we assume $A_p u(kmt + 1)$, which is the particulate isotope activity at the lower bound of the bottom cell, equals particulate isotope activity at the center of the bottom cell ($A_p(kmt)$). This is a reasonable assumption, as the vertical gradient in the abyssal is very small.

$$A_p u(1) = 0$$

$$A_p u(k) = A_p(k-1) + \frac{A_p(k) - A_p(k-1)}{dz w(k-1)} \times \frac{dz(k-1)}{2} \quad (1 < k \leq kmt)$$

(A2)

$$A_p u(kmt + 1) = A_p(kmt)$$

Under this vertical differentiation scheme, if we do vertical integration of $w_S \frac{\partial A_p}{\partial z}$, we will get $w_S A_p(kmt)$, which is the column removal rate of isotope activity and this simulates the process of sedimentation.

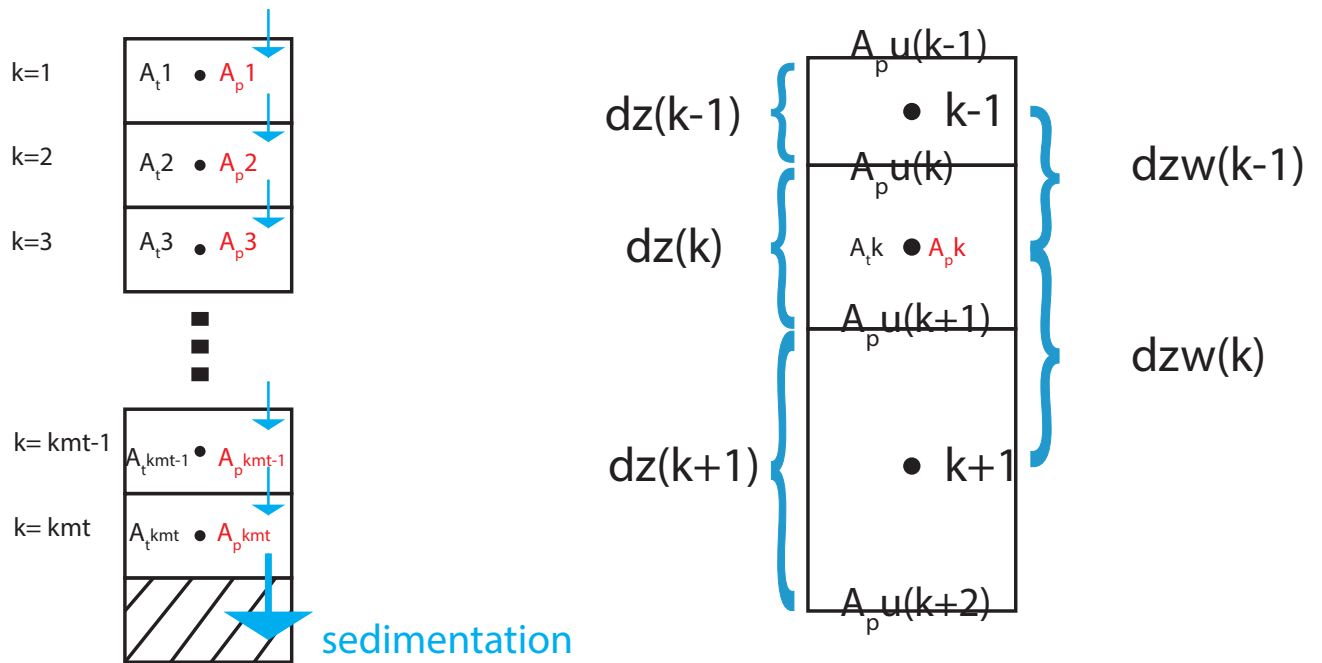


Figure A1. Schematic of model grid. k is the vertical layer. kmt is the maximum vertical layer at this location ($k=kmt$ is the bottom layer). A_t is the total isotope activity. A_p is particulate isotope activity. A_t and A_p are located at the center of the grid box. $A_{p,u}$ is the A_p value at the upper bound of the grid box. $dz(k)$ is the thickness of the layer k . $dzw(k)$ is the distance from the center of layer k to the center of layer $k+1$.

BIBLIOGRAPHY

- Albarède, F. and Goldstein, S.: World map of Nd isotopes in sea-floor ferromanganese deposits, *Geology*, 20(8), 761–763, 1992.
- Amakawa, H., Alibo, D. S. and Nozaki, Y.: Nd isotopic composition and REE pattern in the surface waters of the eastern Indian Ocean and its adjacent seas, *Geochim. Cosmochim. Acta*, 64(10), 1715–1727, doi:10.1016/S0016-7037(00)00333-1, 2000.
- Amakawa, H., Sasaki, K. and Ebihara, M.: Nd isotopic composition in the central North Pacific, *Geochim. Cosmochim. Acta*, 73(16), 4705–4719, doi:10.1016/j.gca.2009.05.058, 2009.
- Anderson, R. F., Bacon, M. P. and Brewer, P. G.: Removal of ^{230}Th and ^{231}Pa from the open ocean, *Earth Planet. Sci. Lett.*, 62(1), 7–23, doi:10.1016/0012-821X(83)90067-5, 1983.
- Anderson, R. F., Lao, Y., Broecker, W. S., Trumbore, S. E., Hofmann, H. J. and Wolfli, W.: Boundary scavenging in the Pacific Ocean: A comparison of ^{10}Be and ^{231}Pa , *Earth Planet. Sci. Lett.*, 96(3–4), 287–304, doi:10.1016/j.cognition.2008.05.007, 1990.
- Anderson, R. F., Fleisher, M. Q., Biscaye, P. E., Kumar, N., Dittrich, B., Kubik, P. and Suter, M.: Anomalous boundary scavenging in the Middle Atlantic Bight: evidence from ^{230}Th , ^{231}Pa , ^{10}Be and ^{210}Pb , *Deep. Res. Part II*, 41(2–3), 537–561, doi:10.1016/0967-0645(94)90034-5, 1994.
- Armstrong, R. A., Lee, C., Hedges, J. I., Honjo, S. and Wakeham, S. G.: A new, mechanistic model for organic carbon fluxes in the ocean based on the quantitative association of POC with ballast minerals, *Deep. Res. Part II Top. Stud. Oceanogr.*, 49(1–3), 219–236, doi:10.1016/S0967-0645(01)00101-1, 2002.
- Arsouze, T., Dutay, J. C., Lacan, F. and Jeandel, C.: Modeling the neodymium isotopic composition with a global ocean circulation model, *Chem. Geol.*, 239(1–2), 165–177, doi:10.1016/j.chemgeo.2006.12.006, 2007.
- Arsouze, T., Dutay, J.-C., Lacan, F. and Jeandel, C.: Reconstructing the Nd oceanic cycle using a coupled dynamical – biogeochemical model, *Biogeosciences*, 6(12), 2829–2846, doi:10.5194/bg-6-2829-2009, 2009.

- Bacon, M. and Anderson, R.: Distribution of Thorium Isotopes between dissolved and particulate forms in the deep sea, *J. Geophys. Res.* ..., 87(1), 2045–2056, 1982.
- Bacon, M. P. and Rosholt, J. N.: Accumulation rates of ^{230}Th , ^{231}Pa , and some transition metals on the Bermuda Rise, *Geochim. Cosmochim. Acta*, 46, 651–666, 1982.
- Bacon, M. P., Huh, C. A. and Moore, R. M.: Vertical profiles of some natural radionuclides over the Alpha Ridge, Arctic Ocean, *Earth Planet. Sci. Lett.*, 95(1–2), 15–22, doi:10.1016/0012-821X(89)90164-7, 1989.
- von Blanckenburg, F.: Tracing past ocean circulation?, *Science* (80-.), 286(5446), 1862–1863, 1999.
- Böhm, E., Lippold, J., Gutjahr, M., Frank, M., Blaser, P., Antz, B., Fohlmeister, J., Frank, N., Andersen, M. B. and Deininger, M.: Strong and deep Atlantic meridional overturning circulation during the last glacial cycle, *Nature*, doi:10.1038/nature14059, 2014.
- Boyle, E. A. and Keigwin, L.: North Atlantic thermohaline circulation during the past 20,000 years linked to high-latitude surface temperature, *Nature*, 330, 35–40, doi:10.1038/330035a0, 1987.
- Bradt Miller, L. I., Anderson, R. F., Fleisher, M. Q. and Burckle, L. H.: Opal burial in the equatorial Atlantic Ocean over the last 30 ka: Implications for glacial-interglacial changes in the ocean silicon cycle, *Paleoceanography*, 22(4), 1–15, doi:10.1029/2007PA001443, 2007.
- Bradt Miller, L. I., McManus, J. F. and Robinson, L. F.: $^{231}\text{Pa}/^{230}\text{Th}$ evidence for a weakened but persistent Atlantic meridional overturning circulation during Heinrich Stadial 1, *Nat. Commun.*, 5, 5817, doi:10.1038/ncomms6817, 2014.
- Brady, E. C., Otto-bliesner, B. L., Kay, J. E. and Rosenbloom, N.: Sensitivity to glacial forcing in the CCSM4, *J. Clim.*, 26(6), 1901–1925, doi:10.1175/JCLI-D-11-00416.1, 2013.
- Burckel, P., Waelbroeck, C., Luo, Y., Roche, D. M., Pichat, S., Jaccard, S. L., Gherardi, J., Govin, A., Lippold, J. and Thil, F.: Changes in the geometry and strength of the Atlantic meridional overturning circulation during the last glacial (20-50 ka), *Clim.*

- Past, 12(11), 2061–2075, doi:10.5194/cp-12-2061-2016, 2016.
- Burton, K. W. and Vance, D.: Glacial-interglacial variations in the neodymium isotope composition of seawater in the Bay of Bengal recorded by planktonic foraminifera, *Earth Planet. Sci. Lett.*, 176(3–4), 425–441, doi:10.1016/S0012-821X(00)00011-X, 2000.
- Came, R. E., Oppo, D. W., Curry, W. B. and Lynch-Stieglitz, J.: Deglacial variability in the surface return flow of the Atlantic meridional overturning circulation, *Paleoceanography*, 23(1), doi:10.1029/2007PA001450, 2008.
- Chase, Z., Anderson, R. F., Fleisher, M. Q. and Kubik, P. W.: The influence of particle composition and particle flux on scavenging of Th, Pa and Be in the ocean, *Earth Planet. Sci. Lett.*, 204(1–2), 215–229, doi:10.1016/S0012-821X(02)00984-6, 2002.
- Chen, T. Y., Robinson, L. F., Burke, A., Southon, J., Spooner, P., Morris, P. J. and Ng, H. C.: Synchronous centennial abrupt events in the ocean and atmosphere during the last deglaciation, *Science* (80-.), 349(6255), 1537–1541, doi:10.1126/science.aac6159, 2015.
- Clark, P. U., Pisias, N. G., Stocker, T. F. and Weaver, A. J.: The role of the thermohaline circulation in abrupt climate change, *Nature*, 415(6874), 863–869, doi:10.1126/science.1081056, 2002.
- Cochran, J. K., Livingston, H. D., Hirschberg, D. J. and Surprenant, L. D.: Natural and anthropogenic radionuclide distributions in the northwest Atlantic Ocean, *Earth Planet. Sci. Lett.*, 84(2–3), 135–152, doi:10.1016/0012-821X(87)90081-1, 1987.
- Cochran, J. K., Hirschberg, D. J., Livingston, H. D., Buesseler, K. O. and Key, R. M.: Natural and anthropogenic radionuclide distributions in the Nansen Basin, Arctic Ocean: Scavenging rates and circulation timescales, *Deep. Res. Part II*, 42(6), 1495–1517, doi:10.1016/0967-0645(95)00051-8, 1995.
- Colley, S., Thomson, J. and Newton, P. P.: Detailed Th-230, Th-232 and Pb-210 fluxes recorded by the 1989/90 BOFS sediment trap time-series at 48N, 20W, *Deep - Sea Res. Part I - Oceanogr. Res. Pap.*, 42(6), 833–848, 1995.
- Coppola, L., Roy-Barman, M., Mulson, S., Povinec, P. and Jeandel, C.: Thorium isotopes as tracers of particles dynamics and deep water circulation in the Indian sector

- of the Southern Ocean (ANTARES IV), *Mar. Chem.*, 100(3–4 SPEC. ISS.), 299–313, doi:10.1016/j.marchem.2005.10.019, 2006.
- Crocket, K. C., Vance, D., Gutjahr, M., Foster, G. L. and Richards, D. A.: Persistent Nordic deep-water overflow to the glacial North Atlantic, *Geology*, 39(6), 515–518, doi:10.1130/G31677.1, 2011.
- Cunningham, S. a, Kanzow, T., Rayner, D., Baringer, M. O., Johns, W. E., Marotzke, J., Longworth, H. R., Grant, E. M., Hirschi, J. J., Beal, L. M., Meinen, C. S. and Bryden, H. L.: Temporal Variability of the Atlantic Meridional Overturning Circulation at 26.5N, , 317(August), 935–938, 2007.
- Curry, W. B. and Oppo, D. W.: Glacial water mass geometry and the distribution of $\delta^{13}\text{C}$ of ΣCO_2 in the western Atlantic Ocean, *Paleoceanography*, 20(1), n/a-n/a, doi:10.1029/2004PA001021, 2005.
- Danabasoglu, G., Bates, S. C., Briegleb, B. P., Jayne, S. R., Jochum, M., Large, W. G., Peacock, S. and Yeager, S. G.: The CCSM4 ocean component, *J. Clim.*, 25(5), 1361–1389, doi:10.1175/JCLI-D-11-00091.1, 2012.
- DeMaster, D. J.: The marine budgets of silica and ^{32}Si , Yale., 1979.
- Deng, F., Thomas, A. L., Rijkenberg, M. J. A. and Henderson, G. M.: Controls on seawater ^{231}Pa , ^{230}Th and ^{232}Th concentrations along the flow paths of deep waters in the Southwest Atlantic, *Earth Planet. Sci. Lett.*, 390, 93–102, doi:10.1016/j.epsl.2013.12.038, 2014.
- Dokken, T. M. and Jansen, E.: Rapid changes in the mechanism of ocean convection during the last glacial period, *Nature*, 401(6752), 458–461, doi:10.1038/46753, 1999.
- Doney, S. C., Lima, I., Feely, R. A., Glover, D. M., Lindsay, K., Mahowald, N., Moore, J. K. and Wanninkhof, R.: Mechanisms governing interannual variability in upper-ocean inorganic carbon system and air-sea CO_2 fluxes: Physical climate and atmospheric dust, *Deep. Res. Part II Top. Stud. Oceanogr.*, 56(8–10), 640–655, doi:10.1016/j.dsr2.2008.12.006, 2009.
- Dutay, J.-C., Lacan, F., Roy-Barman, M. and Bopp, L.: Influence of particle size and type on ^{231}Pa and ^{230}Th simulation with a global coupled biogeochemical-ocean general circulation model: A first approach, *Geochemistry, Geophys. Geosystems*,

10(1), doi:10.1029/2008GC002291, 2009.

Edmonds, H. N., Moran, S. B., Hoff, J. A., Smith, J. N. and Edwards, R. L.: Protactinium-231 and Thorium-230 Abundances and High Scavenging Rates in the Western Arctic Ocean, *Science* (80-.), 280(5362), 405–407, doi:10.1126/science.280.5362.405, 1998.

Edmonds, H. N., Moran, S. B., Cheng, H. and Edwards, R. L.: 230Th and 231Pa in the Arctic Ocean: Implications for particle fluxes and basin-scale Th/Pa fractionation, *Earth Planet. Sci. Lett.*, 227(1–2), 155–167, doi:10.1016/j.epsl.2004.08.008, 2004.

Ferrari, R., Jansen, M. F., Adkins, J. F., Burke, A., Stewart, A. L. and Thompson, A. F.: Antarctic sea ice control on ocean circulation in present and glacial climates., *Proc. Natl. Acad. Sci. U. S. A.*, 111(24), 8753–8, doi:10.1073/pnas.1323922111, 2014.

van de Flierdt, T., Griffiths, A. M., Lambelet, M., Little, S. H., Stichel, T. and Wilson, D. J.: Neodymium in the oceans: a global database, a regional comparison and implications for palaeoceanographic research, *Philos. Trans. R. Soc. A Math. Phys. Eng. Sci.*, 374(2081), 20150293, doi:10.1098/rsta.2015.0293, 2016.

Francois, R., Bacon, M. P., Altabet, M. A. and Labeyrie, L. D.: Glacial/interglacial changes in sediment rain rate in the SW Indian Sector of subantarctic Waters as recorded by 230Th, 231Pa, U, and d15N, *Paleoceanography*, 8(5), 611–629, doi:10.1029/93PA00784, 1993.

Frank, M.: Reconstruction of Late Quaternary environmental conditions applying the natural radionuclides 230Th, 10Be, 231Pa and 238U: A study of deep-sea sediments from the eastern sector of the Antarctic Circumpolar Current System, Alfred Wegener Institute for Polar and Marine Research., 1996.

Frank, M., Eisenhauer, A., Kubik, P. W., Dittrich-hannen, B. and Segl, M.: Beryllium 10, thorium 230, and protactinium 231 in Galapagos microplate sediments: Implications of hydrothermal activity and paleoproductivity changes during the last 100,000 years, *Palaeogeography*, 9(4), 559–578, 1994.

Ganachaud, A. and Wunsch, C.: Improved estimates of global ocean circulation, heat transport and mixing from hydrographic data., *Nature*, 408(6811), 453–457, doi:10.1038/35044048, 2000.

- Gebbie, G. and Huybers, P.: Meridional circulation during the Last Glacial Maximum explored through a combination of South Atlantic $\delta^{18}\text{O}$ observations and a geostrophic inverse model, *Geochemistry, Geophys. Geosystems*, 7(11), doi:10.1029/2006GC001383, 2006.
- Geibert, W. and Usbeck, R.: Adsorption of thorium and protactinium onto different particle types: Experimental findings, *Geochim. Cosmochim. Acta*, 68(7), 1489–1501, doi:10.1016/j.gca.2003.10.011, 2004.
- Gherardi, J., Labeyrie, L., Mcmanus, J., Francois, R., Skinner, L. and Cortijo, E.: Evidence from the Northeastern Atlantic basin for variability in the rate of the meridional overturning circulation through the last deglaciation, *Earth Planet. Sci. Lett.*, 240(3–4), 710–723, doi:10.1016/j.epsl.2005.09.061, 2005.
- Gherardi, J.-M., Labeyrie, L., Nave, S., Francois, R., McManus, J. F. and Cortijo, E.: Glacial-interglacial circulation changes inferred from $^{231}\text{Pa}/^{230}\text{Th}$ sedimentary record in the North Atlantic region, *Paleoceanography*, 24(2), doi:10.1029/2008PA001696, 2009.
- Gnanadesikan, A.: A Simple Predictive Model for the Structure of the Oceanic Pycnocline, *Science* (80-.), 283(5410), 2077–2079, doi:10.1126/science.283.5410.2077, 1999.
- Goes, M., Wainer, I., Gent, P. R. and Bryan, F. O.: Changes in subduction in the South Atlantic Ocean during the 21st century in the CCSM3, *Geophys. Res. Lett.*, 35(6), L06701, doi:10.1029/2007GL032762, 2008.
- Goldstein, S. and Hemming, S.: Long-lived isotopic tracers in oceanography, paleoceanography, and ice-sheet dynamics, *Treatise on geochemistry*, 6(6), 453–489, 2003.
- Goldstein, S. L., O’Nions, R. K. and Hamilton, P. J.: A Sm-Nd isotopic study of atmospheric dusts and particulates from major river systems, *Earth Planet. Sci. Lett.*, 70(2), 221–236, doi:10.1016/0012-821X(84)90007-4, 1984.
- Greaves, M., Statham, P. and Elderfield, H.: Rare earth element mobilization from marine atmospheric dust into seawater, *Mar. Chem.*, 46(3), 255–260, 1994.
- Grousset, F. E., Biscaye, P. E., Zindler, a., Prospero, J. and Chester, R.: Neodymium

- isotopes as tracers in marine sediments and aerosols: North Atlantic, *Earth Planet. Sci. Lett.*, 87(4), 367–378, doi:10.1016/0012-821X(88)90001-5, 1988.
- Grousset, F. E., Parra, M., Bory, A., Martinez, P., Bertrand, P., Shimmield, G. and Ellam, R. M.: Saharan wind regimes traced by the Sr-Nd isotopic composition of subtropical Atlantic sediments: Last Glacial Maximum vs Today, *Quat. Sci. Rev.*, 17(4–5), 395–409, doi:10.1016/S0277-3791(97)00048-6, 1998.
- Gruber, N., Gloor, M., Mikaloff Fletcher, S. E., Doney, S. C., Dutkiewicz, S., Follows, M. J., Gerber, M., Jacobson, A. R., Joos, F., Lindsay, K., Menemenlis, D., Mouchet, A., Müller, S. a., Sarmiento, J. L. and Takahashi, T.: Oceanic sources, sinks, and transport of atmospheric CO₂, *Global Biogeochem. Cycles*, 23(1), doi:10.1029/2008GB003349, 2009.
- Gu, S. and Liu, Z.: 231Pa and 230Th in the ocean model of the Community Earth System Model (CESM1.3), *Geosci. Model Dev.*, 10, 4723–4742, 2017.
- Gu, S., Liu, Z., Zhang, J., Rempfer, J., Joos, F. and Oppo, D. W.: Coherent response of Antarctic Intermediate Water and Atlantic Meridional Overturning Circulation during the last deglaciation: reconciling contrasting neodymium isotope reconstructions from the tropical Atlantic, *Paleoceanography*, 1036–1053, doi:10.1002/2017PA003092, 2017a.
- Gu, S., Liu, Z., Jahn, A., Rempfer, J., Zhang, J. and Joos, F.: Neodymium isotopes in the ocean model of the Community Earth System Model (CESM1.3), *Geosci. Model Dev. Discuss.*, (March), 1–41, doi:10.5194/gmd-2017-40, 2017b.
- Guo, L., Santschi, P. H., Baskaran, M. and Zindler, A.: Distribution of dissolved and particulate 230Th and 232Th in seawater from the Gulf of Mexico and off Cape Hatteras as measured by SIMS, *Earth Planet. Sci. Lett.*, 133(1), 117–128, 1995.
- Gutjahr, M., Frank, M., Stirling, C. H., Keigwin, L. D. and Halliday, a. N.: Tracing the Nd isotope evolution of North Atlantic Deep and Intermediate Waters in the western North Atlantic since the Last Glacial Maximum from Blake Ridge sediments, *Earth Planet. Sci. Lett.*, 266(1–2), 61–77, doi:10.1016/j.epsl.2007.10.037, 2008.
- Hain, M. P., Sigman, D. M. and Haug, G. H.: Distinct roles of the Southern Ocean and North Atlantic in the deglacial atmospheric radiocarbon decline, *Earth Planet. Sci. Lett.*,

394, 198–208, doi:10.1016/j.epsl.2014.03.020, 2014.

Hall, I. R., Moran, S. B., Zahn, R., Knutz, P. C., Shen, C.-C. and Edwards, R. L.: Accelerated drawdown of meridional overturning in the late-glacial Atlantic triggered by transient pre-H event freshwater perturbation, *Geophys. Res. Lett.*, 33(16), L16616, doi:10.1029/2006GL026239, 2006.

Harris, S. and Mix, A.: Pleistocene Precipitation Balance in the Amazon Basin Recorded in Deep Sea Sediments, *Quat. Res.*, 26(1999), 14–26, doi:10.1006/qres.1998.2008, 1999.

Hayes, C. T., Anderson, R. F., Fleisher, M. Q., Serno, S., Winckler, G. and Gersonde, R.: Quantifying lithogenic inputs to the North Pacific Ocean using the long-lived thorium isotopes, *Earth Planet. Sci. Lett.*, 383, 16–25, doi:10.1016/j.epsl.2013.09.025, 2013.

Hayes, C. T., Anderson, R. F., Fleisher, M. Q., Huang, K. F., Robinson, L. F., Lu, Y., Cheng, H., Edwards, R. L. and Moran, S. B.: ^{230}Th and ^{231}Pa on GEOTRACES GA03, the U.S. GEOTRACES North Atlantic transect, and implications for modern and paleoceanographic chemical fluxes, *Deep. Res. Part II Top. Stud. Oceanogr.*, 116, 29–41, doi:10.1016/j.dsr2.2014.07.007, 2015.

He, F.: SIMULATING TRANSIENT CLIMATE EVOLUTION OF THE LAST DEGLACIATION WITH CCSM3. [online] Available from: http://www.researchgate.net/profile/Feng_He4/publication/263618839_Simulating_transient_climate_evolution_of_the_last_deglaciation_with_CCSM3/links/0c96053b5fc619188f000000.pdf (Accessed 25 August 2015), 2011.

He, F., Shakun, J. D., Clark, P. U., Carlson, A. E., Liu, Z., Otto-Bliesner, B. L. and Kutzbach, J. E.: Northern Hemisphere forcing of Southern Hemisphere climate during the last deglaciation., *Nature*, 494(7435), 81–5, doi:10.1038/nature11822, 2013.

Henderson, G. M. and Anderson, R. F.: The U-series toolbox for paleoceanography, *Rev. Mineral. Geochemistry*, 52(1), 493–531, doi:10.2113/0520493, 2003.

Hesse, T., Butzin, M., Bickert, T. and Lohmann, G.: A model-data comparison of $\delta^{13}\text{C}$ in the glacial Atlantic Ocean, *Paleoceanography*, 26(3), 1–16, doi:10.1029/2010PA002085, 2011.

Hoffmann, S. S., McManus, J. F., Curry, W. B. and Brown-Leger, L. S.: Persistent export of ^{231}Pa from the deep central Arctic Ocean over the past 35,000 years., *Nature*, 497(7451), 603–6, doi:10.1038/nature12145, 2013.

Holland, W. R.: Baroclinic and topographic influences on the transport in western boundary currents, *Geophys. Fluid Dyn.*, 4(1), 187–210, doi:10.1080/03091927208236095, 1972.

Howe, J. N. W., Piotrowski, A. M., Oppo, D. W., Huang, K.-F., Mulitza, S., Chiessi, C. M. and Blusztajn, J.: Antarctic Intermediate Water circulation in the South Atlantic over the past 25,000 years, *Paleoceanography*, doi:10.1002/2016PA002975, 2016a.

Howe, J. N. W., Piotrowski, A. M., Noble, T. L., Mulitza, S., Chiessi, C. M. and Bayon, G.: North Atlantic Deep Water Production during the Last Glacial Maximum., *Nat. Commun.*, 7, 11765, doi:10.1038/ncomms11765, 2016b.

Hsieh, Y. Te, Henderson, G. M. and Thomas, A. L.: Combining seawater ^{232}Th and ^{230}Th concentrations to determine dust fluxes to the surface ocean, *Earth Planet. Sci. Lett.*, 312(3–4), 280–290, doi:10.1016/j.epsl.2011.10.022, 2011.

Huang, K.-F., Oppo, D. W. and Curry, W. B.: Decreased influence of Antarctic intermediate water in the tropical Atlantic during North Atlantic cold events, *Earth Planet. Sci. Lett.*, 389, 200–208, doi:10.1016/j.epsl.2013.12.037, 2014.

Huh, C. A. and Beasley, T. M.: Profiles of dissolved and particulate thorium isotopes in the water column of coastal Southern California, *Earth Planet. Sci. Lett.*, 85(1–3), 1–10, doi:10.1016/0012-821X(87)90016-1, 1987.

Ito, T., Woloszyn, M. and Mazloff, M.: Anthropogenic carbon dioxide transport in the Southern Ocean driven by Ekman flow., *Nature*, 463(7277), 80–83, doi:10.1038/nature08687, 2010.

Jacobsen, S. B. and Wasserburg, G. J.: Sm-Nd isotopic evolution of chondrites, *Earth Planet. Sci. Lett.*, 50(1), 139–155, doi:10.1016/0012-821X(80)90125-9, 1980.

Jahn, A., Lindsay, K., Giraud, X., Gruber, N., Otto-Bliesner, B. L., Liu, Z. and Brady, E. C.: Carbon isotopes in the ocean model of the Community Earth System Model (CESM1), *Geosci. Model Dev.*, 8(8), 2419–2434, doi:10.5194/gmd-8-2419-2015, 2015.

Jeandel, C., Arsouze, T., Lacan, F., Techine, P. and Dutay, J.: Isotopic Nd compositions

- and concentrations of the lithogenic inputs into the ocean: A compilation, with an emphasis on the margins, *Chem. Geol.*, 239(1–2), 156–164, doi:10.1016/j.chemgeo.2006.11.013, 2007.
- Johannesson, K. H. and Burdige, D. J.: Balancing the global oceanic neodymium budget: Evaluating the role of groundwater, *Earth Planet. Sci. Lett.*, 253(1–2), 129–142, doi:10.1016/j.epsl.2006.10.021, 2007.
- Jones, K. M., Khatiwala, S. P., Goldstein, S. L., Hemming, S. R. and van de Flierdt, T.: Modeling the distribution of Nd isotopes in the oceans using an ocean general circulation model, *Earth Planet. Sci. Lett.*, 272(3–4), 610–619, doi:10.1016/j.epsl.2008.05.027, 2008.
- Jonkers, L., Zahn, R., Thomas, A., Henderson, G., Abouchami, W., Francois, R., Masque, P., Hall, I. R. and Bickert, T.: Deep circulation changes in the central South Atlantic during the past 145 kyrs reflected in a combined $^{231}\text{Pa}/^{230}\text{Th}$, Neodymium isotope and benthic $\delta^{13}\text{C}$ record, *Earth Planet. Sci. Lett.*, 419, 14–21, doi:10.1016/j.epsl.2015.03.004, 2015.
- Keeling, R. and Stephens, B.: Antarctic sea ice and the control of Pleistocene climate instability, *Paleoceanography*, 16(1), 112–131 [online] Available from: http://www.eol.ucar.edu/~stephens/papers/2000PA000529_648.pdf (Accessed 8 September 2015), 2001.
- Keigwin, L. D. and Boyle, E. A.: Did North Atlantic overturning halt 17,000 years ago?, *Paleoceanography*, 23(1), 1–5, doi:10.1029/2007PA001500, 2008.
- Keigwin, L. D. and Lehman, S. J.: Deep circulation change linked to HEINRICH Event 1 and Younger Dryas in a middepth North Atlantic Core, *Paleoceanography*, 9(2), 185–194, doi:10.1029/94PA00032, 1994.
- Kriest, I.: Different parameterizations of marine snow in a 1D-model and their influence on representation of marine snow, nitrogen budget and sedimentation, *Deep. Res. Part I Oceanogr. Res. Pap.*, 49(12), 2133–2162, doi:10.1016/S0967-0637(02)00127-9, 2002.
- Kroopnick, P.: The distribution of ^{13}C in the Atlantic Ocean, *Earth Planet. Sci. Lett.*, 49(2), 469–484, doi:10.1016/0012-821X(80)90088-6, 1980.
- Ku, T. L.: Uranium series disequilibrium in deep sea sediments, Columbia., 1966.

- Ku, T. L., Bischoff, J. L. and Boersma, A.: Age studies of Mid-Atlantic Ridge sediments near 42°N and 20°N, *Deep. Res. Oceanogr. Abstr.*, 19(3), 233–247, doi:10.1016/0011-7471(72)90033-2, 1972.
- Kumar, N.: Trace metals and natural radionuclides as tracers of ocean productivity, Columbia., 1994.
- Kumar, N., Gwiazda, R., Anderson, R. F. and Froelich, P. N.: $^{231}\text{Pa}/^{230}\text{Th}$ ratios in sediments as a proxy for past changes in Southern Ocean productivity, *Nature*, 362, 45–48, doi:10.1038/362045a0, 1993.
- Labeyrie, L. D., Duplessy, J., Duprat, J., Juillet-Leclerc, A., Moyes, J., Michel, E., Kallel, N. and Shackleton, N. J.: Changes in the vertical structure of the North Atlantic Ocean between glacial and modern times, *Quat. Sci. Rev.*, 11(4), 401–413, doi:10.1016/0277-3791(92)90022-Z, 1992.
- Large, W. G. and Yeager, S. G.: The global climatology of an interannually varying air–sea flux data set, *Clim. Dyn.*, 33(2–3), 341–364, doi:10.1007/s00382-008-0441-3, 2008.
- LeGrand, P. and Wunsch, C.: Constraints from palaeo-tracer data on the North Atlantic circulation during the last glacial maximum, *Paleoceanography*, 10(6), 1011–1045, 1995.
- Lézine, A. M., Duplessy, J. C. and Cazet, J. P.: West African monsoon variability during the last deglaciation and the Holocene: Evidence from fresh water algae, pollen and isotope data from core KW31, Gulf of Guinea, *Palaeogeogr. Palaeoclimatol. Palaeoecol.*, 219(3–4), 225–237, doi:10.1016/j.palaeo.2004.12.027, 2005.
- Lippold, J., Grützner, J., Winter, D., Lahaye, Y., Mangini, A. and Christi, M.: Does sedimentary $^{231}\text{Pa}/^{230}\text{Th}$ from the Bermuda Rise monitor past Atlantic Meridional Overturning Circulation?, *Geophys. Res. Lett.*, 36(12), 1–6, doi:10.1029/2009GL038068, 2009.
- Lippold, J., Gherardi, J. M. and Luo, Y.: Testing the $^{231}\text{Pa}/^{230}\text{Th}$ paleocirculation proxy: A data versus 2D model comparison, *Geophys. Res. Lett.*, 38(20), 1–7, doi:10.1029/2011GL049282, 2011.
- Lippold, J., Mulitza, S., Mollenhauer, G., Weyer, S., Heslop, D. and Christl, M.: Boundary scavenging at the East Atlantic margin does not negate use of $^{231}\text{Pa}/^{230}\text{Th}$

- to trace Atlantic overturning, *Earth Planet. Sci. Lett.*, 333–334, 317–331, doi:10.1016/j.epsl.2012.04.005, 2012a.
- Lippold, J., Luo, Y., Francois, R., Allen, S. E., Gherardi, J., Pichat, S., Hickey, B. and Schulz, H.: Strength and geometry of the glacial Atlantic Meridional Overturning Circulation, *Nat. Geosci.*, 5(11), 813–816, doi:10.1038/ngeo1608, 2012b.
- Liu, Z., Otto-Bliesner, B. L., He, F., Brady, E. C., Tomas, R., Clark, P. U., Carlson, a E., Lynch-Stieglitz, J., Curry, W., Brook, E., Erickson, D., Jacob, R., Kutzbach, J. and Cheng, J.: Transient simulation of last deglaciation with a new mechanism for Bolling-Allerod warming., *Science*, 325(5938), 310–4, doi:10.1126/science.1171041, 2009.
- Liu, Z., Zhu, J., Rosenthal, Y., Zhang, X., Otto-Bliesner, B. L., Timmermann, A., Smith, R. S., Lohmann, G., Zheng, W. and Elison Timm, O.: The Holocene temperature conundrum., *Proc. Natl. Acad. Sci. U. S. A.*, 111(34), E3501-5, doi:10.1073/pnas.1407229111, 2014.
- Long, M. C., Lindsay, K., Peacock, S., Moore, J. K. and Doney, S. C.: Twentieth-century oceanic carbon uptake and storage in CESM1(BGC), *J. Clim.*, 26(18), 6775–6800, doi:10.1175/JCLI-D-12-00184.s1, 2013.
- Lugmair, G. W.: Sm-Nd ages: a new dating method, *Meteoritics*, 9, 369, 1974.
- Lumpkin, R. and Speer, K.: Large-scale vertical and horizontal circulation in the North Atlantic Ocean, *J. Phys. Oceanogr.*, 33(9), 1902–1920, 2003.
- Luo, C., Mahowald, N. and Corral, J.: Sensitivity study of meteorological parameters on mineral aerosol mobilization, transport, and distribution, *J. Geophys. Res.*, 108(D15), 4447, doi:10.1029/2003JD003483, 2003.
- Luo, S. D., Ku, T. L., Kusakabe, M., Bishop, J. K. B. and Yang, Y. L.: Tracing particle cycling in the upper ocean with Th-230 and Th-228: An investigation in the equatorial Pacific along 140 degrees W, *Deep - Sea Res. Part II - Top. Stud. Oceanogr.*, 42(2–3), 805–829, doi:10.1016/0967-0645(95)00019-M, 1995.
- Luo, Y., Francois, R. and Allen, S.: Sediment $^{231}\text{Pa}/^{230}\text{Th}$ as a recorder of the rate of the Atlantic meridional overturning circulation: insights from a 2-D model, *Ocean Sci.*, 6(3), 381–400, doi:10.5194/os-6-381-2010, 2010.
- Lupker, M., Aciego, S. M., Bourdon, B., Schwander, J. and Stocker, T. F.: Isotopic

tracing (Sr, Nd, U and Hf) of continental and marine aerosols in an 18th century section of the Dye-3 ice core (Greenland), *Earth Planet. Sci. Lett.*, 295(1–2), 277–286, doi:10.1016/j.epsl.2010.04.010, 2010.

Lynch-Stieglitz, J., Curry, W. B. and Slowey, N.: A geostrophic transport estimate for the Florida Current from the oxygen isotope composition of benthic foraminifera, *Paleoceanography*, 14(3), 360–373, doi:10.1029/1999PA900001, 1999.

Lynch-Stieglitz, J., Curry, W. B., Oppo, D. W., Ninneman, U. S., Charles, C. D. and Munson, J.: Meridional overturning circulation in the South Atlantic at the last glacial maximum, *Geochemistry, Geophys. Geosystems*, 7(10), n/a-n/a, doi:10.1029/2005GC001226, 2006.

Lynch-Stieglitz, J., Schmidt, M. W., Henry, G. L., Curry, W. B., Skinner, L. C., Mulitza, S., Zhang, R. and Chang, P.: Muted change in Atlantic overturning circulation over some glacial-aged Heinrich events, *Nat. Geosci.*, 7(12), 144–150, doi:10.1038/ngeo2045, 2014.

Mangini, A. and Diester-Hass, L.: Excess Th-230 in sediments off NW Africa traces upwelling during the past 130,000 years, in *Coastal upwelling: Its sedimentary records*, edited by E. Suess and J. Thiede, pp. 455–470, Plenum., 1983.

Mangini, A. and Key, R. M.: A ^{230}Th profile in the Atlantic Ocean, *Earth Planet. Sci. Lett.*, 62(3), 377–384, doi:10.1016/0012-821X(83)90008-0, 1983.

Mangini, A. and Sonntag, C.: ^{231}Pa dating of deep-sea cores via ^{227}Th counting, *Earth Planet. Sci. Lett.*, 37(2), 251–256, 1977.

Mangini, A. and U., K.: Depositional history in the Clarion-Clipperton zone during the last 250,000 years: ^{230}Th and ^{231}Pa methods, *Geol. Jahrb.*, 87, 105–121, 1987.

Marchal, O., François, R., Stocker, T. F. and Joos, F.: Ocean thermohaline circulation and sedimentary $^{231}\text{Pa}/^{230}\text{Th}$ ratio, *Paleoceanography*, 15(6), 625–641 [online] Available from: <http://onlinelibrary.wiley.com/doi/10.1029/2000PA000496/full> (Accessed 19 April 2016), 2000.

Marchitto, T. M. and Broecker, W. S.: Deep water mass geometry in the glacial Atlantic Ocean: A review of constraints from the paleonutrient proxy Cd/Ca, *Geochemistry, Geophys. Geosystems*, 7(12), doi:10.1029/2006GC001323, 2006.

- Marchitto, T. M., Curry, W. B., Lynch-Stieglitz, J., Bryan, S. P., Cobb, K. M. and Lund, D. C.: Improved oxygen isotope temperature calibrations for cosmopolitan benthic foraminifera, *Geochim. Cosmochim. Acta*, 130, 1–11, doi:10.1016/j.gca.2013.12.034, 2014.
- Marcott, S. a., Shakun, J. D., Clark, P. U. and Mix, A. C.: A Reconstruction of Regional and Global Temperature for the Past 11,300 Years, *Science*, 339(6124), 1198–1201, doi:10.1126/science.1228026, 2013.
- Marotzke, J., Giering, R., Zhang, K. Q., Stammer, D., Hill, C. and Lee, T.: Construction of the adjoint MIT ocean general circulation model and application to Atlantic heat transport sensitivity, *J. Geophys. Res.*, 104547(15), 529–29, doi:10.1029/1999JC900236, 1999.
- McCreary, J. P. and Lu, P.: Influence of the Indonesian Throughflow on the Circulation of Pacific Intermediate Water, *J. Phys. Oceanogr.*, 31(4), 932–942, doi:10.1175/1520-0485(2001)031<0932:IOTITO>2.0.CO;2, 2001.
- McManus, J., Francois, R. and Gherardi, J.: Collapse and rapid resumption of Atlantic meridional circulation linked to deglacial climate changes, *Nature*, 428(6985), 834–837, 2004.
- Moore, J. K. and Braucher, O.: Sedimentary and mineral dust sources of dissolved iron to the World Ocean, *Biogeosciences*, 5(1994), 631–656, doi:10.5194/bgd-4-1279-2007, 2008.
- Moore, J. K., Doney, S. C., Glover, D. M. and Fung, I. Y.: Iron cycling and nutrient-limitation patterns in surface waters of the World Ocean, , 49, 463–507, 2002.
- Moore, J. K., Doney, S. C. and Lindsay, K.: Upper ocean ecosystem dynamics and iron cycling in a global three-dimensional model, *Global Biogeochem. Cycles*, 18(4), doi:10.1029/2004GB002220, 2004.
- Moore, J. K., Lindsay, K., Doney, S. C., Long, M. C. and Misumi, K.: Marine Ecosystem Dynamics and Biogeochemical Cycling in the Community Earth System Model [CESM1(BGC)]: Comparison of the 1990s with the 2090s under the RCP4.5 and RCP8.5 Scenarios, *J. Clim.*, 26(23), 9291–9312, doi:10.1175/JCLI-D-12-00566.1, 2013.
- Moore, W. S.: The thorium isotope content of ocean water, *Earth Planet. Sci. Lett.*,

53(3), 419–426, doi:10.1016/0012-821X(81)90046-7, 1981.

Moran, S. B., Hoff, J. A., Buesseler, K. O. and Edwards, R. L.: High precision ^{230}Th and ^{232}Th in the Norwegian Sea and Denmark by thermal ionization mass spectrometry, , 22(19), 2589–2592, 1995.

Moran, S. B., Charette, M. a., Hoff, J. a., Edwards, R. L. and Landing, W. M.: Distribution of ^{230}Th in the Labrador Sea and its relation to ventilation, *Earth Planet. Sci. Lett.*, 150, 151–160, doi:10.1016/S0012-821X(97)00081-2, 1997.

Moran, S. B., Shen, C.-C., Weinstein, S. E., Hettlinger, L. H., Hoff, J. H., Edmonds, H. N. and Edwards, R. L.: Constraints on deep water age and particle flux in the Equatorial and South Atlantic Ocean based on seawater ^{231}Pa and ^{230}Th data, *Geophys. Res. Lett.*, 28(18), 3437–3440 [online] Available from:

papers2://publication/uuid/2A811583-B32B-4BD8-B582-EC8B0D96A949, 2001.

Moran, S. B., Shen, C. C., Edmonds, H. N., Weinstein, S. E., Smith, J. N. and Edwards, R. L.: Dissolved and particulate ^{231}Pa and ^{230}Th in the Atlantic Ocean: Constraints on intermediate/deep water age, boundary scavenging, and $^{231}\text{Pa}/^{230}\text{Th}$ fractionation, *Earth Planet. Sci. Lett.*, 203(3–4), 999–1014, doi:10.1016/S0012-821X(02)00928-7, 2002.

Müller, P. J. and Mangini, A.: Organic carbon decomposition rates in sediments of the pacific manganese nodule belt dated by ^{230}Th and ^{231}Pa , *Earth Planet. Sci. Lett.*, 51(1), 94–114, doi:10.1016/0012-821X(80)90259-9, 1980.

Negre, C., Zahn, R., Thomas, A. L., Masqué, P., Henderson, G. M., Martínez-Méndez, G., Hall, I. R. and Mas, J. L.: Reversed flow of Atlantic deep water during the Last Glacial Maximum., *Nature*, 468(7320), 84–88, doi:10.1038/nature09508, 2010.

Nozaki, Y. and Horibe, Y.: Alpha-emitting thorium isotopes in northwest Pacific deep waters, *Earth Planet. Sci. Lett.*, 65(1), 39–50, doi:10.1016/0012-821X(83)90188-7, 1983.

Nozaki, Y. and Nakanishi, T.: ^{231}Pa and ^{230}Th profiles in the open ocean water column, *Deep Sea Res. Part A, Oceanogr. Res. Pap.*, 32(10), 1209–1220, doi:10.1016/0198-0149(85)90004-4, 1985.

Nozaki, Y. and Yamada, M.: Thorium and protactinium isotope distributions in waters

- of the Japan Sea, *Deep Sea Res. Part A, Oceanogr. Res. Pap.*, 34(8), 1417–1430, 1987.
- Nozaki, Y. and Yang, H. S.: Th and Pa isotopes in the waters of the western margin of the Pacific near Japan: Evidence for release of ^{228}Ra and ^{227}Ac from slope sediments, *J. Oceanogr. Soc. Japan*, 43(4), 217–227, doi:10.1007/BF02109817, 1987.
- Nozaki, Y., Horibe, Y. and Tsubota, H.: The water column distribution of thorium isotopes in the western North Pacific, *Earth Planet. Sci. Lett.*, 54(54), 203–216, 1981.
- Nozaki, Y., Yang, H.-S. and Yamada, M.: Scavenging of thorium in the ocean, *J. Geophys. Res.*, 92(C1), 772, doi:10.1029/JC092iC01p00772, 1987.
- Nurnberg, D. and Tiedemann, R.: Environmental change in the Sea of Okhotsk during the last 1.1 million years, *Paleoceanography*, 19(4), 1–23, doi:10.1029/2004PA001023, 2004.
- Okubo, A., Obata, H., Nozaki, Y., Yamamoto, Y. and Minami, H.: ^{230}Th in the Andaman Sea: Rapid deep-sea renewal, *Geophys. Res. Lett.*, 31(22), 1–5, doi:10.1029/2004GL020226, 2004.
- Okubo, A., Obata, H., Luo, S., Gamo, T., Yamamoto, Y., Minami, H. and Yamada, M.: Particle flux in the twilight zone of the eastern Indian Ocean: A constraint from ^{234}U - ^{230}Th and ^{228}Ra - ^{228}Th disequilibria, *Deep. Res. Part I Oceanogr. Res. Pap.*, 54(10), 1758–1772, doi:10.1016/j.dsr.2007.06.009, 2007a.
- Okubo, A., Obata, H., Gamo, T., Minami, H. and Yamada, M.: Scavenging of ^{230}Th in the Sulu Sea, *Deep. Res. Part II Top. Stud. Oceanogr.*, 54(1–2), 50–59, doi:10.1016/j.dsr2.2006.02.016, 2007b.
- Okubo, A., Obata, H., Gamo, T. and Yamada, M.: ^{230}Th and ^{232}Th distributions in mid-latitudes of the North Pacific Ocean: Effect of bottom scavenging, *Earth Planet. Sci. Lett.*, 339–340, 139–150, doi:10.1016/j.epsl.2012.05.012, 2012.
- Oppo, D. W., Curry, W. B. and McManus, J. F.: What do benthic $\delta^{13}\text{C}$ and $\delta^{18}\text{O}$ data tell us about Atlantic circulation during Heinrich Stadial 1?, *Paleoceanography*, 30(4), 353–368, doi:10.1002/2014PA002667, 2015.
- Osborne, A. H., Haley, B. A., Hathorne, E. C., Flögel, S. and Frank, M.: Neodymium isotopes and concentrations in Caribbean seawater: Tracing water mass mixing and continental input in a semi-enclosed ocean basin, *Earth Planet. Sci. Lett.*, 406, 174–186,

doi:10.1016/j.epsl.2014.09.011, 2014.

Pahnke, K., Goldstein, S. L. and Hemming, S. R.: Abrupt changes in Antarctic Intermediate Water circulation over the past, *Nat. Geosci.*, 1(12), 870–874, doi:10.1038/ngeo360, 2008.

Palter, J. B. and Lozier, M. S.: On the source of Gulf Stream nutrients, *J. Geophys. Res.*, 113(C6), C06018, doi:10.1029/2007JC004611, 2008.

Pena, L. D., Goldstein, S. L., Hemming, S. R., Jones, K. M., Calvo, E., Pelejero, C. and Cacho, I.: Rapid changes in meridional advection of Southern Ocean intermediate waters to the tropical Pacific during the last 30kyr, *Earth Planet. Sci. Lett.*, 368, 20–32, doi:10.1016/j.epsl.2013.02.028, 2013.

Piepgras, D. and Wasserburg, G.: Isotopic Composition of Neodymium in Waters from the Drake Passage, *Science* (80-.), 217(4556), 207–214, 1982.

Piepgras, D., Wasserburg, G. and Dasch, E.: The isotopic composition of Nd in different ocean masses, *Earth Planet. Sci. ...*, 45(2), 223–236, 1979.

Piepgras, D. . and Wasserburg, G. .: Rare earth element transport in the western North Atlantic inferred from Nd isotopic observations, *Geochim. Cosmochim. Acta*, 51(5), 1257–1271, doi:10.1016/0016-7037(87)90217-1, 1987.

Piotrowski, A. M., Goldstein, S. L., Hemming, S. R. and Fairbanks, R. G.: Intensification and variability of ocean thermohaline circulation through the last deglaciation, *Earth Planet. Sci. Lett.*, 225(1–2), 205–220, doi:10.1016/j.epsl.2004.06.002, 2004.

Piotrowski, A. M., Galy, A., Nicholl, J. A. L., Roberts, N., Wilson, D. J., Clegg, J. A. and Yu, J.: Reconstructing deglacial North and South Atlantic deep water sourcing using foraminiferal Nd isotopes, *Earth Planet. Sci. Lett.*, 357, 289–297, doi:10.1016/j.epsl.2012.09.036, 2012.

Rahmstorf, S.: Ocean circulation and climate during the past 120,000 years., *Nature*, 419(6903), 207–214, doi:10.1038/nature01090, 2002.

Rempfer, J., Stocker, T. F., Joos, F., Dutay, J.-C. and Siddall, M.: Modelling Nd-isotopes with a coarse resolution ocean circulation model: Sensitivities to model parameters and source/sink distributions, *Geochim. Cosmochim. Acta*, 75(20), 5927–

5950, doi:10.1016/j.gca.2011.07.044, 2011.

Rempfer, J., Stocker, T. F., Joos, F. and Dutay, J.-C.: On the relationship between Nd isotopic composition and ocean overturning circulation in idealized freshwater discharge events, *Paleoceanography*, 27(3), doi:10.1029/2012PA002312, 2012a.

Rempfer, J., Stocker, T. F., Joos, F. and Dutay, J.-C.: Sensitivity of Nd isotopic composition in seawater to changes in Nd sources and paleoceanographic implications, *J. Geophys. Res.*, 117(C12), C12010, doi:10.1029/2012JC008161, 2012b.

Rempfer, J., Stocker, T. F., Joos, F., Lippold, J. and Jaccard, S. L.: New insights into cycling of ^{231}Pa and ^{230}Th in the Atlantic Ocean, *Earth Planet. Sci. Lett.*, 468, 27–37, doi:10.1016/j.epsl.2017.03.027, 2017.

Resplandy, L., Bopp, L., Orr, J. C. and Dunne, J. P.: Role of mode and intermediate waters in future ocean acidification: Analysis of CMIP5 models, *Geophys. Res. Lett.*, 40(12), 3091–3095, doi:10.1002/grl.50414, 2013.

Rickaby, R. E. M. and Elderfield, H.: Evidence from the high-latitude North Atlantic for variations in Antarctic Intermediate water flow during the last deglaciation, *Geochemistry, Geophys. Geosystems*, 6(5), doi:10.1029/2004GC000858, 2005.

Rickli, J., Frank, M., Baker, A. R., Aciego, S., de Souza, G., Georg, R. B. and Halliday, A. N.: Hafnium and neodymium isotopes in surface waters of the eastern Atlantic Ocean: Implications for sources and inputs of trace metals to the ocean, *Geochim. Cosmochim. Acta*, 74(2), 540–557, doi:10.1016/j.gca.2009.10.006, 2010.

Rincon-Martinez, D., Lamy, F., Contreras, S., Leduc, G., Bard, E., Saukel, C., Blanz, T., MacKensen, A. and Tiedemann, R.: More humid interglacials in Ecuador during the past 500 kyr linked to latitudinal shifts of the equatorial front and the Intertropical Convergence Zone in the eastern tropical Pacific, *Paleoceanography*, 25(2), 1–15, doi:10.1029/2009PA001868, 2010.

Rintoul, S. R.: South Atlantic interbasin exchange, *J. Geophys. Res.*, 96(C2), 2675, doi:10.1029/90JC02422, 1991.

Roberts, N. L., Piotrowski, A. M., McManus, J. F. and Keigwin, L. D.: Synchronous deglacial overturning and water mass source changes., *Science*, 327(5961), 75–8, doi:10.1126/science.1178068, 2010.

- Roberts, N. L., McManus, J. F., Piotrowski, A. M. and McCave, I. N.: Advection and scavenging controls of Pa/Th in the northern NE Atlantic, *Paleoceanography*, 29(6), 668–679, doi:10.1002/2014PA002633, 2014.
- Robinson, L. F., Belshaw, N. S. and Henderson, G. M.: U and Th concentrations and isotope ratios in modern carbonates and waters from the Bahamas, *Geochim. Cosmochim. Acta*, 68(8), 1777–1789, doi:10.1016/j.gca.2003.10.005, 2004.
- Roy-Barman, M., Chen, J. H. and Wasserburg, G. J.: ^{230}Th - ^{232}Th systematics in the central Pacific Ocean: The sources and the fates of thorium, *Earth Planet. Sci. Lett.*, 139(3–4), 351–363, doi:10.1016/0012-821X(96)00017-9, 1996.
- Rühs, S. and Getzlaff, K.: On the suitability of North Brazil Current transport estimates for monitoring basin-scale AMOC changes, *Geophys. Res. Lett.*, 8072–8080, doi:10.1002/2015GL065695. Received, 2015.
- Rutgers van der Loeff, M. M. and Berger, G. W.: Scavenging of ^{230}Th and ^{231}Pa near the antarctic polar front in the South Atlantic, *Deep. Res. Part I*, 40(2), 339–357, doi:10.1016/0967-0637(93)90007-P, 1993.
- Sabine, C. L.: The Oceanic Sink for Anthropogenic CO_2 , *Science* (80-.), 305(5682), 367–371, doi:10.1126/science.1097403, 2004.
- Saenko, O., Weaver, A. and Gregory, J.: On the link between the two modes of the ocean thermohaline circulation and the formation of global-scale water masses, *J. Clim.*, 16(17), 2797–2801, 2003.
- Sarkisyan, A. S. and Ivanov, V. F.: Joint effect of baroclinicity and bottom relief as an important factor in the dynamics of the sea current, *Investiya Acad. Sci. USSR, Atmos. Ocean Sci. (English Trans)*, 1, 173–188, 1971.
- Sarmiento, J. L., Gruber, N., Brzezinski, M. A. and Dunne, J. P.: High-latitude controls of thermocline nutrients and low latitude biological productivity., *Nature*, 427(6969), 56–60, doi:10.1038/nature10605, 2004.
- Schmid, C., Siedler, G. and Zenk, W.: Dynamics of Intermediate Water Circulation in the Subtropical South Atlantic, *J. Phys. Oceanogr.*, 3191–3211, 2000.
- Schmittner, A.: Decline of the marine ecosystem caused by a reduction in the Atlantic overturning circulation., *Nature*, 434(7033), 628–633, doi:10.1038/nature03476, 2005.

- Schmitz, W., Mangini, A., Stoffers, P., Glasby, G. P. and Pluger, W. L.: Sediment accumulation rates in the southwestern Pacific Basin and Aitutaki Passage, *Mar. Geol.*, 73(1), 181–190, 1986.
- Schmitz, W. J. and McCartney, M. S.: ON THE NORTH ATLANTIC CIRCULATION, *Rev. Geophys.*, (92), 29–49, 1993.
- Scholten, J. C., Rutgers van der Loeff, M. M. and Michel, A.: Distribution of ^{230}Th and ^{231}Pa in the water column in relation to the ventilation of the deep Arctic basins, *Deep. Res. Part II*, 42(6), 1519–1531, doi:10.1016/0967-0645(95)00052-6, 1995.
- Scholten, J. C., Fietzke, J., Mangini, A., Stoffers, P., Rixen, T., Gaye-Haake, B., Blanz, T., Ramaswamy, V., Sirocko, F., Schulz, H. and Ittekkot, V.: Radionuclide fluxes in the Arabian Sea: The role of particle composition, *Earth Planet. Sci. Lett.*, 230(3–4), 319–337, doi:10.1016/j.epsl.2004.11.003, 2005.
- Scholten, J. C., Fietzke, J., Mangini, A., Garbe-Schönberg, C. D., Eisenhauer, A., Schneider, R. and Stoffers, P.: Advection and scavenging: Effects on ^{230}Th and ^{231}Pa distribution off Southwest Africa, *Earth Planet. Sci. Lett.*, 271(1–4), 159–169, doi:10.1016/j.epsl.2008.03.060, 2008.
- Shimmield, G. B. and Price, N. B.: The scavenging of U, ^{230}Th and ^{231}Pa during pulsed hydrothermal activity at 20°S, East Pacific Rise, *Geochim. Cosmochim. Acta*, 52(3), 669–677, doi:10.1016/0016-7037(88)90329-8, 1988.
- Shimmield, G. B., Murray, J. W., Thomson, J., Bacon, M. P., Anderson, R. F. and Price, N. B.: The distribution and behaviour of ^{230}Th and ^{231}Pa at an ocean margin, Baja California, Mexico, *Geochim. Cosmochim. Acta*, 50(11), 2499–2507, doi:10.1016/0016-7037(86)90032-3, 1986.
- Siddall, M., Henderson, G. M., Edwards, N. R., Frank, M., Müller, S. a., Stocker, T. F. and Joos, F.: $^{231}\text{Pa}/^{230}\text{Th}$ fractionation by ocean transport, biogenic particle flux and particle type, *Earth Planet. Sci. Lett.*, 237(1–2), 135–155, doi:10.1016/j.epsl.2005.05.031, 2005.
- Siddall, M., Stocker, T. F., Henderson, G. M., Joos, F., Frank, M., Edwards, N. R., Ritz, S. P. and Müller, S. a.: Modeling the relationship between $^{231}\text{Pa}/^{230}\text{Th}$ distribution in North Atlantic sediment and Atlantic meridional overturning circulation,

- Paleoceanography, 22(2), n/a-n/a, doi:10.1029/2006PA001358, 2007.
- Siddall, M., Khatiwala, S., van de Flierdt, T., Jones, K., Goldstein, S. L., Hemming, S. and Anderson, R. F.: Towards explaining the Nd paradox using reversible scavenging in an ocean general circulation model, *Earth Planet. Sci. Lett.*, 274(3–4), 448–461, doi:10.1016/j.epsl.2008.07.044, 2008.
- Sima, A., Paul, A., Schulz, M. and Oerlemans, J.: Modeling the oxygen-isotopic composition of the North American Ice Sheet and its effect on the isotopic composition of the ocean during the last glacial cycle, *Geophys. Res. Lett.*, 33(15), 1–5, doi:10.1029/2006GL026923, 2006.
- Stichel, T., Frank, M., Rickli, J. and Haley, B. a.: The hafnium and neodymium isotope composition of seawater in the Atlantic sector of the Southern Ocean, *Earth Planet. Sci. Lett.*, 317–318, 282–294, doi:10.1016/j.epsl.2011.11.025, 2012.
- Stoll, H. M., Vance, D. and Arevalos, A.: Records of the Nd isotope composition of seawater from the Bay of Bengal: Implications for the impact of Northern Hemisphere cooling on ITCZ movement, *Earth Planet. Sci. Lett.*, 255(1–2), 213–228, doi:10.1016/j.epsl.2006.12.016, 2007.
- Stouffer, R., Seidov, D. and Haupt, B.: Climate response to external sources of freshwater: North Atlantic versus the Southern Ocean, *J. Clim.*, 30(3), 436–448 [online] Available from: <http://journals.ametsoc.org/doi/abs/10.1175/jcli4015.1> (Accessed 28 September 2015), 2007.
- Tachikawa, K., Athias, V. and Jeandel, C.: Neodymium budget in the modern ocean and paleo-oceanographic implications, *J. Geophys. Res.*, 108(C8), 3254, doi:10.1029/1999JC000285, 2003.
- Talley, L.: *Antarctic Intermediate Water in the South Atlantic.*, 1996.
- Thomas, A. L., Henderson, G. M. and Robinson, L. F.: Interpretation of the $^{231}\text{Pa}/^{230}\text{Th}$ paleocirculation proxy: New water-column measurements from the southwest Indian Ocean, *Earth Planet. Sci. Lett.*, 241(3–4), 493–504, doi:10.1016/j.epsl.2005.11.031, 2006.
- Toggweiler, J. R. and Samuels, B.: Effect of drake passage on the global thermohaline circulation, *Deep. Res. Part I*, 42(4), 477–500, doi:10.1016/0967-0637(95)00012-U,

1995.

Trimble, S. M., Baskaran, M. and Porcelli, D.: Scavenging of thorium isotopes in the Canada Basin of the Arctic Ocean, *Earth Planet. Sci. Lett.*, 222(3–4), 915–932, doi:10.1016/j.epsl.2004.03.027, 2004.

Tütken, T., Eisenhauer, A., Wiegand, B. and Hansen, B. T.: Glacial-interglacial cycles in Sr and Nd isotopic composition of Arctic marine sediments triggered by the Svalbard/Barents Sea ice sheet, *Mar. Geol.*, 182(3–4), 351–372, doi:10.1016/S0025-3227(01)00248-1, 2002.

Vallis, G.: Large-scale circulation and production of stratification: Effects of wind, geometry, and diffusion, *J. Phys. Oceanogr.*, (1962), 933–954 [online] Available from: [http://journals.ametsoc.org/doi/abs/10.1175/1520-0485\(2000\)030%3C0933%3ALSCAPO%3E2.0.CO%3B2](http://journals.ametsoc.org/doi/abs/10.1175/1520-0485(2000)030%3C0933%3ALSCAPO%3E2.0.CO%3B2) (Accessed 4 May 2015), 2000.

Venchiarutti, C., van der Loeff, M. R. and Stimac, I.: Scavenging of ^{231}Pa and thorium isotopes based on dissolved and size-fractionated particulate distributions at Drake Passage (ANTXXIV-3), *Deep. Res. Part II Top. Stud. Oceanogr.*, 58(25–26), 2767–2784, doi:10.1016/j.dsr2.2010.10.040, 2011.

Vogler, S., Scholten, J., Rutgers van der Loeff, M. M. and Mangini, A.: ^{230}Th in the eastern North Atlantic: the importance of water mass ventilation in the balance of ^{230}Th , *Earth Planet. Sci. Lett.*, 156(1–2), 61–74, doi:10.1016/S0012-821X(98)00011-9, 1998.

Wainer, I., Goes, M., Murphy, L. N. and Brady, E.: Changes in the intermediate water mass formation rates in the global ocean for the Last Glacial Maximum, mid-Holocene and pre-industrial climates, *Paleoceanography*, 27(3), n/a-n/a, doi:10.1029/2012PA002290, 2012.

Walter, H. J., Rutgers van der Loeff, M. M. and Hoeltzen, H.: Enhanced scavenging of ^{231}Pa relative to ^{230}Th in the South Atlantic south of the Polar Front: Implications for the use of the $^{231}\text{Pa}/^{230}\text{Th}$ ratio as a paleoproductivity proxy, *Earth Planet. Sci. Lett.*, 149(1), 85–100, doi:10.1016/S0012-821X(97)00068-X, 1997.

Weaver, A. J., Saenko, O. A., Clark, P. U. and Mitrovica, J. X.: Meltwater pulse 1A

- from Antarctica as a trigger of the Bølling-Allerød warm interval., *Science* (80-.), 299(5613), 1709–13, doi:10.1126/science.1081002, 2003.
- Wolfe, C. L. and Cessi, P.: What Sets the Strength of the Middepth Stratification and Overturning Circulation in Eddy Ocean Models?, *J. Phys. Oceanogr.*, 40(7), 1520–1538, doi:10.1175/2010JPO4393.1, 2010.
- Wolff, E. W., Fischer, H., Fundel, F., Ruth, U., Twarloh, B., Littot, G. C., Mulvaney, R., Röthlisberger, R., De Angelis, M., Boutron, C. F., Hansson, M., Jonsell, U., Hutterli, M. A., Lambert, F., Kaufmann, P., Stauffer, B., Stocker, T. F., Steffensen, J. P., Bigler, M., Siggaard-Andersen, M. L., Udisti, R., Becagli, S., Castellano, E., Severi, M., Wagenbach, D., Barbante, C., Gabrielli, P. and Gaspari, V.: Southern Ocean sea-ice extent, productivity and iron flux over the past eight glacial cycles., *Nature*, 440(7083), 491–496, doi:10.1038/nature06271, 2006.
- Xie, R. C., Marcantonio, F. and Schmidt, M. W.: Deglacial variability of Antarctic Intermediate Water penetration into the North Atlantic from authigenic neodymium isotope ratios, *Paleoceanography*, 27(3), doi:10.1029/2012PA002337, 2012.
- Yang, H. S., Nozaki, Y., Sakai, H. and Masuda, A.: The distribution of ^{230}Th and ^{231}Pa in the deep-sea surface sediments of the Pacific Ocean, *Geochim. Cosmochim. Acta*, 50(1), 81–89, doi:10.1016/0016-7037(86)90050-5, 1986.
- Yeager, S. and Danabasoglu, G.: Sensitivity of atlantic meridional overturning circulation variability to parameterized Nordic Sea overflows in CCSM4, *J. Clim.*, 25(6), 2077–2103, doi:10.1175/JCLI-D-11-00149.1, 2012.
- Yong-Liang Yang, Elderfield, H., Pedersen, T. F. and Ivanovich, M.: Geochemical record of the Panama Basin during the Last Glacial Maximum carbon event shows that the glacial ocean was not suboxic, *Geology*, 23(12), 1115–1118, doi:10.1130/0091-7613(1995)023<1115:GROTPB>2.3.CO, 1995.
- Yong Lao, Anderson, R. F., Broecker, W. S., Trumbore, S. E., Hofmann, H. J. and Wolfli, W.: Transport and burial rates of ^{10}Be and ^{231}Pa in the Pacific Ocean during the Holocene period, *Earth Planet. Sci. Lett.*, 113(1–2), 173–189, doi:10.1016/0012-821X(92)90218-K, 1992.
- Yu, E.-F.: Variations in the Particulate Flux of ^{230}Th and ^{231}Pa and

- Paleoceanographic Applications of the $^{231}\text{Pa}/^{230}\text{Th}$ Ratio, WHOI/MIT., 1994.
- Yu, E.-F., Francois, R. and Bacon, M. P.: Similar rates of modern and last-glacial ocean thermohaline circulation inferred from radiochemical data, *Nature*, 379(6567), 689–694, doi:10.1038/379689a0, 1996.
- Zahn, R. and Stüber, A.: Suborbital intermediate water variability inferred from paired benthic foraminiferal Cd/Ca and $\delta^{13}\text{C}$ in the tropical West Atlantic and linking with North Atlantic, *Earth Planet. Sci. Lett.*, 200, 191–205, 2002.
- Zektser, I. S. and Loaiciga, H. A.: Groundwater fluxes in the global hydrologic cycle: past, present and future, *J. Hydrol.*, 144(1–4), 405–427, doi:10.1016/0022-1694(93)90182-9, 1993.
- Zhang, D., Msadek, R., McPhaden, M. J. and Delworth, T.: Multidecadal variability of the North Brazil Current and its connection to the Atlantic meridional overturning circulation, *J. Geophys. Res.*, 116(C4), C04012, doi:10.1029/2010JC006812, 2011.
- Zhang, J., Liu, Z., Brady, E. C., Jahn, A., Oppo, D. W., Clark, P. U., Marcott, S. A. and Lindsay, K.: Asynchronous warming and oxygen isotope evolution of deep Atlantic water masses during the last deglaciation, *Proc. Natl. Acad. Sci.*, 114(42), 11075–11080, doi:10.1073/pnas.1704512114, 2017.
- Zheng, X. Y., Plancherel, Y., Saito, M. A., Scott, P. M. and Henderson, G. M.: Rare earth elements (REEs) in the tropical South Atlantic and quantitative deconvolution of their non-conservative behavior, *Geochim. Cosmochim. Acta*, 177, 217–237, doi:10.1016/j.gca.2016.01.018, 2016.